

X-SORTER (X-RAY SURVEY OF MERGING CLUSTERS IN REDMAPPER): X-RAY AND SPECTROSCOPIC CHARACTERIZATION OF 12 OPTICALLY SELECTED GALAXY CLUSTER MERGER CANDIDATES

CHRISTOPHER HOPP¹ , DAVID WITTMAN¹ , RODRIGO STANCIOLI¹ , ZHUORAN GAO¹, FAIK BOUHRİK^{1,2} , AND SCOTT ADLER³ 

¹Department of Physics & Astronomy, University of California, Davis, CA 95616

²Department of Physics & Astronomy, California State University, Sacramento, CA 95819 and

³School of Physics & Astronomy, Rochester Institute of Technology, Rochester, NY 14623

Version March 11, 2026

Abstract

Merging galaxy clusters offer a unique probe of dark matter (DM) interactions through the spatial offsets between galaxies, the intracluster medium, and the DM halo. Systems that are binary, near the plane of the sky, and observed shortly after first pericenter provide the cleanest constraints on the DM self-interaction cross-section. The **X-SORTER** (X-ray Survey Of meRging cluSTERS in redMaPPer) program aims to systematically identify such mergers using optical indicators of binarity in the redMaPPer cluster catalog and to follow up promising candidates with X-ray and spectroscopic observations. We select clusters where the top redMaPPer brightest cluster galaxy (BCG) probability is below 0.98, the top two BCGs are separated by at least $0.95'$, and the optical richness exceeds $\lambda = 120$. We present XMM-Newton and Keck/DEIMOS observations of twelve clusters with no previous XMM-Newton or Chandra archival data meeting these criteria. The X-ray data reveal that most targets are morphologically disturbed, with several clear post-pericenter, dissociative systems exhibiting X-ray peaks between the BCGs. Spectroscopy confirms cluster membership and rules out foreground or background contamination. Together, these results demonstrate that optical BCG properties provide an efficient means of identifying dynamically active clusters suitable for detailed, multi-wavelength studies of dark matter and cluster evolution.

Subject headings: Galaxy clusters (584) — X-ray astronomy (1810) — Intracluster medium (858) — Galaxy spectroscopy (2171) — Redshift surveys (1378)

1. INTRODUCTION

Merging galaxy clusters are powerful laboratories for constraining the properties of dark matter (DM). As two (or more) clusters collide, their constituent components—galaxies, intracluster medium (ICM), and dark matter—are provided ample opportunity to interact. During these events, the galaxies act as effectively collisionless particles, passing through the merger with minimal interaction. The hot gas of the ICM, by contrast, is highly collisional and interacts through ram pressure, causing it to lag behind the collisionless components. Dark matter, inferred from gravitational lensing, behaves more similarly to the collisionless galaxies than the collisional gas, suggesting it is also nearly collisionless. Quantifying the spatial offsets between components in these dissociative mergers offers a way to constrain the interaction properties of dark matter, with a lag between the DM halo and galaxies favoring a DM model with a non-zero self-interaction cross-section (Markevitch et al. 2004; Clowe et al. 2006; Randall et al. 2008; Kim et al. 2017; Golovich et al. 2019a). Because self-interactions cannot be probed in the laboratory, astrophysical systems like these remain the only way to test such models. In particular, merging clusters probe DM interactions at relative velocities exceeding 1000 km s^{-1} (compared to

$\sim 10 \text{ km s}^{-1}$ at dwarf galaxy scales and $\sim 200 \text{ km s}^{-1}$ at galaxy scales (Tulin & Yu 2018)), providing constraints in a velocity regime inaccessible to lower-mass systems.

While cluster mergers provide a powerful method to study dark matter, not all mergers are equally useful. First, the offset between DM and galaxies is predicted to be small, $\sim 10\text{--}40 \text{ kpc}$ for self-interaction cross-sections of $1 \text{ cm}^2 \text{ g}^{-1}$ (Kim et al. 2017; Robertson et al. 2019), which may be further diminished by projection effects. Additionally, systems with complex substructure are prohibitively complicated to model with sufficient accuracy to constrain the nature of dark matter. Finally, the displacement between galaxies, DM, and the ICM depends on the impact parameter and dynamics of the merger. Accurate models must consider the merger stage, infall velocity, and time since pericenter passage (Kim et al. 2017; Golovich et al. 2019a). Thus, the ideal scenario is a head-on binary merger in the plane of the sky observed shortly after the first pericenter passage. These simple, well-modeled systems have utility beyond the study of dark matter. Studies of cluster dynamics, the ICM, and galaxy evolution all benefit from clean merger models.

The quintessential example of a high-quality merger scenario is the Bullet Cluster (Clowe et al. 2006; Robertson et al. 2017; Cha et al. 2025). Other well-studied systems include the Musket Ball Cluster (Dawson et al. 2012), El Gordo (Jee et al. 2014), and Baby Bullet

(Bradač et al. 2008), all of which have produced constraints on the self-interacting dark matter (SIDM) cross-section. From these individual clusters, the tightest upper limit on the SIDM cross-section is $\sigma/m < 0.7 \text{ cm}^2 \text{ g}^{-1}$ (Randall et al. 2008). While these constraints are useful, there is still a wide swath of parameter space available, meriting further study (for reference, these current limits are approximately that of the largest cross-sections in the Standard Model). To further tighten these constraints with mergers, one approach is to consider a larger, statistical ensemble of merging systems (Harvey et al. 2015). However, care must be taken to select an ensemble from clusters in the same merger phase, as the offset between DM and galaxies changes sign once the subhalo is returning from apocenter (Kim et al. 2017; Wittman et al. 2018).

The current sample of such ideal mergers is small, historically discovered serendipitously by their disturbed X-ray morphologies. Extensive work has focused on identifying merging clusters systematically through X-ray (Mann & Ebeling 2012; Arendt et al. 2024) or radio (Golovich et al. 2019b) data. These methods typically identify disturbed systems but do not preferentially select for bimodal mergers with separated subclusters. Other attempts have been made to develop algorithms to identify clusters in optical wavelengths to leverage the high-quality imaging now available across much of the sky from surveys such as SDSS (York et al. 2000), DES (Dark Energy Survey Collaboration et al. 2016), Pan-STARRS (Kaiser et al. 2002), DESI (Dey et al. 2019), and eventually LSST (Ivezić et al. 2019). One approach, using a Friends-of-Friends algorithm, has shown promise in identifying merging structures (Tempel et al. 2017). More recently, Wen et al. (2024) had considerable success in identifying merging systems by locating galaxy overdensities between identified brightest cluster galaxies (BCGs). They identified 3446 systems with post-collision merging features, including two bullet-like clusters.

In this work, we pursue an optical selection strategy using the redMaPPer catalog (Rykoff et al. 2014) to identify clean binary mergers from BCG positions alone. RedMaPPer identifies galaxy clusters from SDSS (York et al. 2000) and, for each cluster, ranks five candidate BCGs by their probability of being the true BCG. In relaxed clusters, the top-ranked BCG is overwhelmingly likely to be the true BCG, whereas in a merger, we expect a secondary BCG with a non-negligible probability.

This strategy forms the basis of the **X-SORTER** (X-ray Survey Of merging cluSTERS in Redmapper) program, which uses optical BCG information to systematically identify merging clusters for targeted X-ray and spectroscopic observations. In this paper, we apply the X-SORTER selection method by targeting clusters where the top BCG probability is less than 98% and the two most likely BCGs have a projected separation of $>0.95'$, criteria designed to identify potential binary mergers. While the full program spans both archival and new observations, we focus here on 12 galaxy clusters lacking previous XMM-Newton or Chandra coverage,¹ selected for follow-up with XMM-Newton. We complement the X-ray data with Keck/DEIMOS spectroscopy to iden-

tify cluster members and rule out foreground and background contamination. These observations are intended as a first-look assessment and do not uniquely constrain the merger scenario of each candidate. However, they provide sufficient information to evaluate the viability of each system for multi-wavelength follow-up.

The paper is structured as follows: in §2, we discuss our selection criteria and data reduction processes. In §3, we cover results and discussion of our selection algorithm as well as specific analysis of each of the 12 clusters targeted. Finally, we summarize and conclude in §4. Throughout this paper, we assume a flat Λ CDM cosmology with $H_0 = 70.0 \text{ km s}^{-1} \text{ Mpc}^{-1}$ and $\Omega_m = 0.3$.

2. METHODS

2.1. Target Selection

We aim to identify binary mergers with a subcluster separation favorable for dark matter follow-up studies (*i.e.*, post-pericenter mergers with small impact parameter and a separation vector mostly in the plane of the sky) using optical photometric properties for the initial selection. Optical properties are well suited to expose bimodality in the projected spatial distribution of the galaxies, but less so for inferring whether the two subclusters are heading toward pericenter (which we will refer to as *premerger*), outbound after first pericenter (*outbound*), or returning after first apocenter (*returning*). See Wen et al. (2024), however, for promising recent work using optical properties to test the merger stage. Our approach relies on X-ray follow-up to identify candidates where the X-ray surface brightness (XSB) peak is between the BCGs, indicating that the ICM has been displaced. These *dissociative* mergers are most likely to have had a small impact parameter and be seen after first pericenter (Dawson et al. 2012; McDonald et al. 2022).

Because our approach requires X-ray follow-up, we focus on richer clusters, which are more likely to yield strong X-ray signals. In turn, because the number of clusters steeply declines with richness, the sample size is much smaller than that of Wen et al. (2024). The sample is defined by cuts on the following three attributes listed in, or derivable from, the redMaPPer catalog:

- **Optical richness** (λ), redMaPPer’s estimate of the number of galaxies in the cluster within a set magnitude range of the BCG magnitude.
- **Projected separation** between the top two BCG candidates.
- **Dominance of the top BCG candidate**, quantified by the redMaPPer attribute P_0 , the probability of the top BCG candidate being the BCG.

Figure 1 shows the joint distribution of these three attributes, along with the redshift z which redMaPPer estimates from photometric properties, with a typical uncertainty of ≈ 0.01 . We cut on these properties as follows:

- The bottom right panel of Figure 1 shows that the modal value of P_0 is near unity, so we impose a cut of $P_0 < 0.98$ to remove a large number of presumably relaxed clusters. This cut by itself removes only about half the clusters, but we found (based on

¹ RM J121917.6+505432.8 did have very shallow Chandra data, insufficient for detailed analysis.

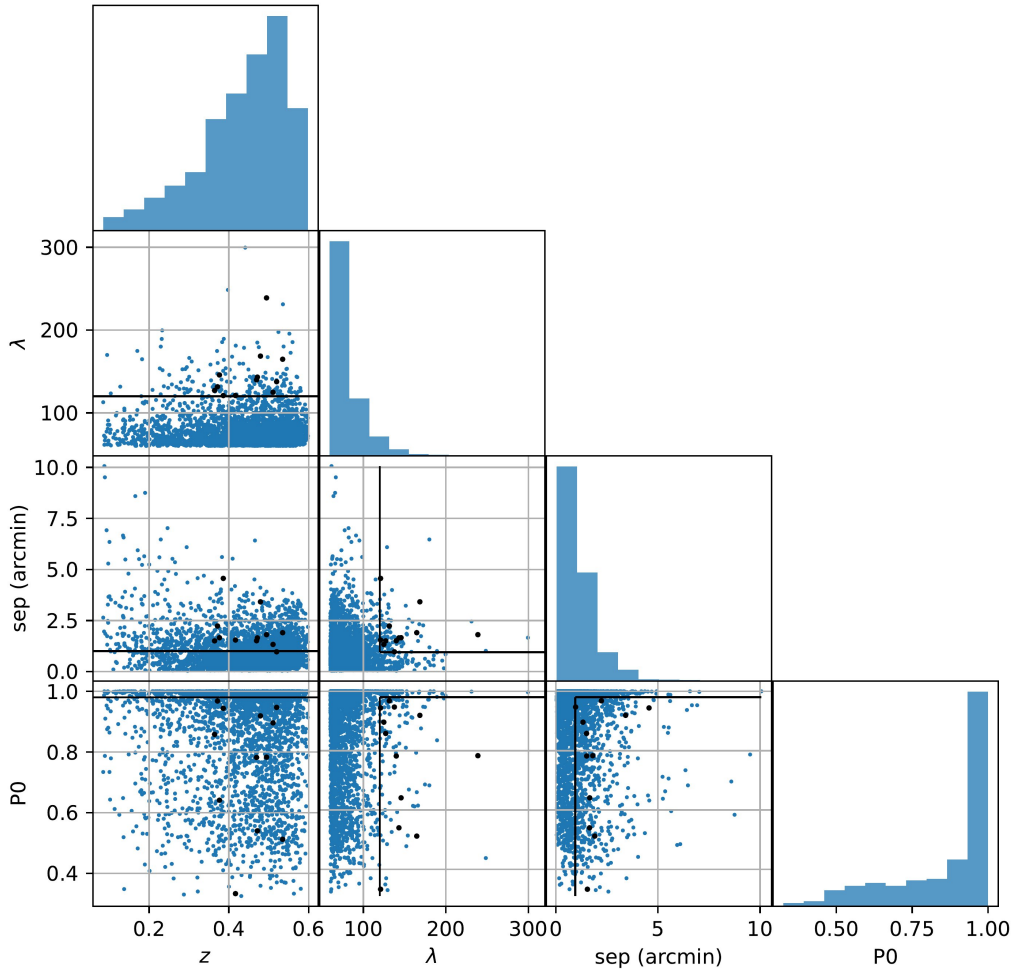


FIG. 1.— Pair plot for the redMaPPer attributes of redshift, richness λ , separation between the top two BCG candidates, and $P0$ (probability of the top BCG candidate being the actual BCG). This plot includes only clusters with $\lambda > 60$ to reduce crowding. Black lines illustrate our cuts, and black points are clusters studied in this paper.

the procedure described below) that good merger candidates can be found even with $P0 \approx 0.9$, so we chose to make other cuts more restrictive.

- We wanted subclusters to be separated by several times the XMM-Newton angular resolution of $10''$ so that the location of the X-ray peak relative to the galaxy subclusters could be determined with relatively short X-ray exposures. Therefore, we seek separations of $\gtrsim 1'$ between the top two BCG candidates; we settled on a cut of $\geq 0.95'$ to obtain a sample size of ≈ 50 . A fixed angular cut has the possible disadvantage of yielding a redshift-dependent cut on the physical separation, thus favoring low-redshift candidates, but in practice, we had no excess of low-redshift candidates (likely due to the richness cut explained below). Over the redshift range 0.2–0.55, the $0.95'$ cut ranges from 190–370 kpc in physical separation.

- Rich candidates are more practical for follow-up, so we imposed a richness cut of $\lambda \geq 120$, to yield a small number of rich candidates. Figure 1 shows that richness is largely uncorrelated with the other attributes, except for the unavoidable lack of rare rich clusters at low z due to the small volume probed there. Therefore, the richness cut reduces the sample size with the side effect of disfavoring low-redshift candidates. Given the opposing redshift effects of the richness and separation cuts, the redshifts of the resulting candidates range from 0.1–0.55, similar to the parent catalog.

We found two cases in which redMaPPer failed to identify an overwhelmingly dominant BCG despite the presence of a single clear BCG: RM J073220.3+314120.7 (Abell 586) and RM J140100.5+025149.7. We suspect the underlying photometry was at fault, for example, if the BCG was saturated or misclassified due to AGN ac-

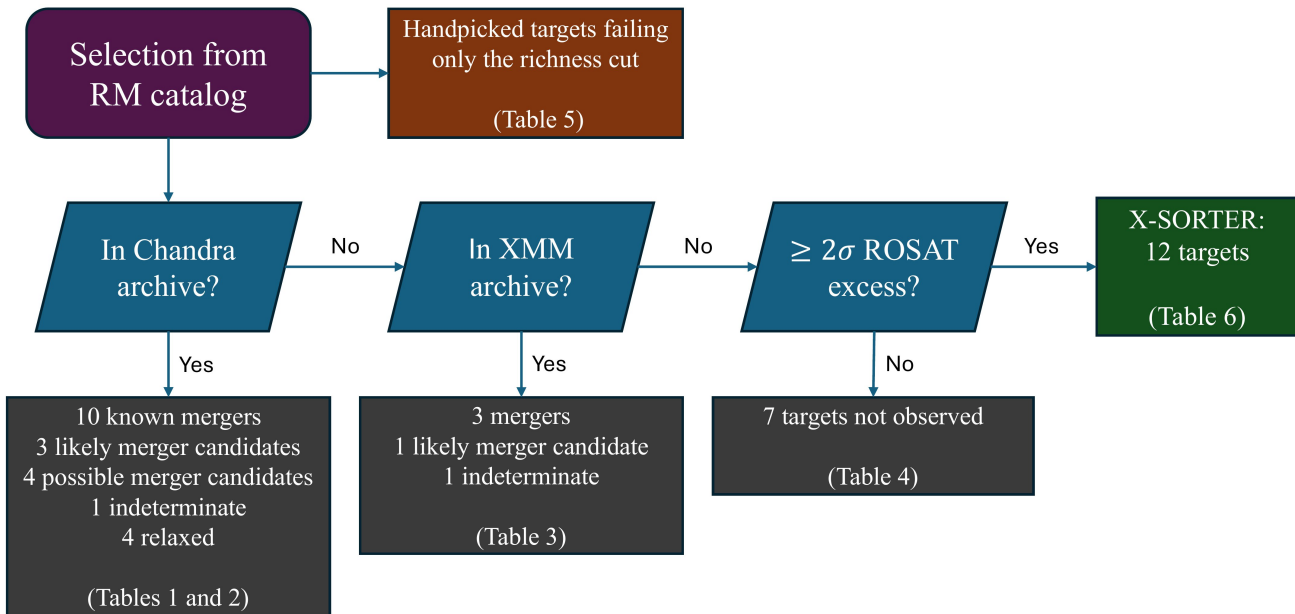


FIG. 2.— Decision tree for X-SORTER targets. The green box on the right is the focus of this paper.

tivity. Therefore, our final cut is a visual inspection to rule out this failure mode. To limit the role of subjective human judgment, we considered no other aspects of redMaPPer performance in this inspection.

The resulting target list was evaluated using the decision tree illustrated in Figure 2. First, we performed a *Chandra* archival search (in mid-2020) to determine how well the selection criteria were yielding systems with an XSB peak between the BCG candidates. This allowed for some experimentation with the cuts. With the final set of cuts, there were 46 targets, with 22 in the *Chandra* archive, 17 of which were also in the *XMM-Newton* archive.

A summary of these 22 systems is given in Tables 1 and 2. The classification given to each system is based on both the observed X-ray morphology and published results in the literature. We also include the morphological parameter, δ , where values of $\delta > 0$ indicate a dynamically active system (Yuan & Han 2020; Yuan et al. 2022). Classifications of “known merger” and “relaxed” require explicit designation in the refereed literature; we do not attempt to re-interpret these prior studies. Systems without a definitive literature classification are divided into “likely” and “possible” merger or relaxed scenarios. “Likely” mergers show disturbed X-ray and/or galaxy-density morphology together with independent supporting evidence (e.g., radio emission, lensing mass structure, or dynamical analysis). “Possible” mergers exhibit disturbed morphology but lack corroborating multiwavelength evidence. Of the 22 systems in the *Chandra* archive, we find 10 previously-known mergers and 7 merger candidates.

For the remaining 24 targets, we searched the *XMM-Newton* archive and found five that had been previously observed, three of which are clear mergers (Table 3). For the 19 targets lacking archival X-ray data, we estimated the *XMM-Newton* exposure time required to record 3500 photons and thus locate the XSB peak to $\lesssim 10''$, even for the highly disturbed morphologies typical of known

merging clusters. We used the clusters that were in the *XMM-Newton* archive to create a mapping between ROSAT All Sky Survey (RASS) flux (Voges et al. 1999) and *XMM-Newton* counts. None of these clusters were cataloged as sources in RASS, but generally had 2–3 σ flux excesses. To reduce the total *XMM-Newton* time for the survey, we opted to drop the seven targets with $< 2\sigma$ RASS excesses. We recognize that with such low signal-to-noise (S/N) in RASS, there is randomness in whether a target appeared above or below 2σ . Therefore, the seven dropped targets may be fruitful in the future. We also identified a few additional promising clusters that are closely related to this project. These are clusters that came to our attention while developing the cuts; had a wealth of archival data worthy of study; and ultimately failed only the richness cut. We list these clusters in Table 4 only to clarify the relationship of this paper to other papers, and do not consider them further in this work. The seven dropped targets are listed separately in Table 5.

The remaining 12 targets with $\geq 2\sigma$ RASS excesses, listed in Table 6, form the basis of the *XMM-Newton* survey described in this paper. Henceforth, we refer to clusters by truncating their redMaPPer designation to the first four digits. All 12 systems are minimally characterized in the literature and none has been the subject of a dedicated multiwavelength analysis. Three clusters (RMJ0829, RMJ1219, and RMJ2321) were included in a LOFAR analysis of Planck SZ-selected clusters by Botteon et al. (2022), while several others appear in large-area optical or SZ cluster catalogs, but without detailed study. These 12 clusters therefore comprise a newly defined, uniformly selected sample of optically identified merger candidates whose X-ray properties have not been systematically examined.

2.2. XMM Data Reduction

The targets were observed across the AO20-22 programs using the *XMM-Newton* European Photon Imag-

TABLE 1
CANDIDATES IN BOTH THE *Chandra* AND XMM-*Newton* ARCHIVES

Name	Redshift ^a	Richness ^a	δ^b	Alt. name(s)	Comment
RM J004629.3+202804.8	0.104	123	0.85	Abell 98 PSZ1 G121.35-42.47	Known merger (Paterno-Mahler et al. 2014) (Sarkar et al. 2023)
RM J015949.3-084958.9	0.408	168	-0.13	MACS J0159.8-0849 RXC J0159.8-0850 PSZ2 G167.66-65.59 ACT-CL J0159.8-0849	Relaxed (Cibirka et al. 2018)
RM J082529.1+470800.9	0.128	132	0.50	Abell 655 RXC J0825.5+4707 PSZ2 G172.63+35.15	Likely merger (Zhang et al. 2023) (Groeneveld et al. 2025)
RM J092052.5+302740.3	0.294	129	0.92	Abell 781	Known merger (Sehgal et al. 2008) (Botteon et al. 2019)
RM J100214.1+203216.6	0.324	151	0.98	Abell 913 PSZ2 G213.30+50.99 WHL J100226.8+203101	Possible merger
RM J101734.3+593339.8	0.289	124	0.60	Abell 959 RXC J1017.5+5934 PSZ2 G151.19+48.27	Known merger (Boschin et al. 2009) (Birzan et al. 2019)
RM J104729.0+151402.1	0.209	128	1.06	Abell 1095 RXC J1047.5+1513 PSZ1 G228.98+58.89	Known merger (Ge et al. 2016) (Burchett et al. 2018)
RM J113613.0+400235.8	0.295	155	0.13	Abell 1319 PSZ2 G168.33+69.73	Known premerger (Wilber et al. 2019)
RM J114935.7+222354.6	0.536	231	0.86	MACS J1149.6+2223 RXC J1149.5+2223 PSZ2 G228.16+75.20	Known merger (Golovich et al. 2019b) (Finner et al. 2025)
RM J115914.9+494748.4	0.363	134	0.01	Abell 1430 RXC J1159.2+4947 PSZ2 G143.26+65.24	Known merger (Hoeft et al. 2021)
RM J121218.5+273255.1	0.354	158	0.39	Abell 1489 RXC J1212.3+2733 PSZ2 G207.88+81.31	Possible merger (Zitrin et al. 2020) (Rines et al. 2022)
RM J155820.0+271400.3	0.095	170	0.01	Abell 2142 RXC J1558.3+2713 PSZ2 G044.20+48.66	Known merger (Liu et al. 2018)
RM J172227.2+320757.2	0.229	180	-0.45	Abell 2261 RXC J1722.4+3208 PSZ2 G055.59+31.85	Likely relaxed (Kim et al. 2022) (Dutta et al. 2025)
RM J221145.9-034944.5	0.426	159	-0.09	MACS J2211.7-0349 RXC J2211.7-0349 PSZ2 G057.25-45.34 ACT-CL J2211.7-0349	Likely relaxed (Cerny et al. 2018) (George et al. 2021)
RM J222826.8+203852.4	0.389	121	0.25	MACS J2228.5+2036 RXC J2228.6+2036 PSZ2 G083.29-31.03	Known merger (Soucail et al. 2015) (Stuardi et al. 2025)
RM J224319.8-093530.9	0.441	299	0.73	MACS J2243.3-0935 RXC J2243.3-0935 PSZ2 G056.93-55.08 ACT-CL J2243.3-0935	Known merger (Cantwell et al. 2016)
RM J231147.6+034107.6	0.301	166	-0.15	Abell 2552 MACS J2311.5+0338 RXC J2311.5+0338 PSZ2 G081.00-50.93 ACT-CL J2311.5+0338	Likely relaxed (Kale et al. 2015)

^aAs estimated by Rykoff et al. (2016).

^bCluster morphology parameter reported from Yuan et al. (2022).

TABLE 2
CANDIDATES IN THE *Chandra* ARCHIVE

Name	Redshift ^a	Richness ^a	δ^b	Alt. name(s)	Comment
RM J105417.5+143904.2	0.297	125	1.48	Abell 1127 PSZ2 G231.56+60.03 ACT-CL J1054.2+1438	Likely merger (Duchesne et al. 2020)
RM J124922.1+494742.1	0.287	129	1.10	Abell 1622 PSZ2 G123.66+67.25	Likely merger (van Weeren et al. 2021) (Paul et al. 2021)
RM J160319.0+031644.6	0.237	132	1.05	PSZ2 G014.09+38.38 ACT-CL J1603.3+0317	Possible merger
RM J211849.1+003337.2	0.265	120	1.50	PSZ2 G052.35-31.98	Indeterminate; low S/N
RM J230707.5+163246.1	0.248	130	1.62	RXC J2307.0+1631 PSZ2 G089.81-39.56 ACT-CL J2307.0+1631	Possible merger

^aAs estimated by Rykoff et al. (2016).

^bCluster morphology parameter reported from Yuan et al. (2022).

TABLE 3
CANDIDATES IN THE XMM-*Newton* ARCHIVE

Name	Redshift ^a	Richness ^a	Alt. name(s)	Comment
RM J003208.2+180625.3	0.398	248	MACS J0032.1+1808 RXCJ 0032.1+1808 PSZ2 G116.50-44.47 ACT-CL J0032.2+1808	Merger (Acebron et al. 2020) (Wittman et al. 2025)
RM J003353.1-075210.4	0.304	128	Abell 56 MACS J0033.8-0751 RXC J0033.8-0750 PSZ2 G109.99-70.28 ACT-CL J0033.8-0751	Merger (Wittman et al. 2023) (Albuquerque et al. 2024)
RM J123416.1+151508.4	0.280	137	ACT-CL J1234.2+1515	Indeterminate; on edge of XMM field
RM J150822.0+575515.2	0.544	153	PSZ2 G094.56+51.03	Merger (Stancioli et al. 2024)
RM J224158.1+173303.7	0.323	126	Abell 2472 MACS J2241.8+1732 RXC J2241.8+1732 PSZ2 G084.13-35.41 ACT-CL J2241.9+1732	Likely merger (Botteon et al. 2022)

^aAs estimated by Rykoff et al. (2016).

TABLE 4
MERGING CLUSTERS IN RELATED PUBLICATIONS

Name	Redshift ^a	Richness ^a	Alt. name(s)	Comment
RM J001938.7+033557.3	0.277	109	ZwCl 0017.0+0320 PSZ2 G107.66-58.32 ACT-CL J0019.6+0336	(Pillay et al. 2021) (Stancioli et al. in prep.)
RM J024808.3-021637.2	0.235	97	Abell 384 RXC J0248.2-0216 PSZ2 G176.25-52.57 ACT-CL J0248.1-0216	(Chatterjee et al. 2025) (Stancioli et al. in prep.)
RM J130558.9+263048.4	0.316	70	ZWCL 1303.6+2647 RXC J1306.0+2630 PSZ2 G023.17+86.71	Bouhrik et al. (2025)
RM J213518.8+012527.0	0.234	109	Abell 2355 RXC J2135.2+0125 PSZ2 G055.95-34.89 ACT-CL J2135.2+0125	Bouhrik et al. in prep.

Note. – Failing the richness cut, these clusters were followed up outside the scope of this paper.

^aAs estimated by Rykoff et al. (2016).

TABLE 5
UNOBSERVED CANDIDATES WITH LOW ROSAT FLUX

Name	Redshift ^a	Richness ^a
RM J005119.7–104940.8	0.502	128
RM J005936.8+131020.8	0.492	148
RM J020824.7+245522.0	0.485	131
RM J112529.9+101339.1	0.502	129
RM J222921.6+105809.0	0.517	129
RM J231211.3+151320.7	0.449	152
RM J233344.5+244324.4	0.499	131

^aAs estimated by Rykoff et al. (2016).

ing Camera (EPIC) and reduced using the Science Analysis System (SAS) Version 22.1.0 (Ochsenbein et al. 2004) in conjunction with the Extended Source Analysis Software (ESAS), largely following the ESAS Cookbook (Snowden & Kuntz 2024). The ESAS tasks were executed via a custom bash pipeline that streamlines the standard reduction workflow and is made publicly available.²

For each detector (MOS1, MOS2, and PN), the data were first filtered of proton flaring events by identifying good time intervals in the 10–12 keV band, removing all events during the contaminated intervals. The exact filtering level depends on the observation, but was generally around 0.3 counts s⁻¹ for the MOS detectors and 0.5 counts s⁻¹ for the PN. Next, the exposures were checked for CCDs in anomalous (broken) states, which were removed from further processing. Point sources were subtracted with the `cheese` routine, with a manual inspection for any missing or wrongfully removed point sources.

Background contamination was removed following the double-subtraction method of Arnaud et al. (2002), with blank-sky files (Carter & Read 2007) to account for spatial variability in the backgrounds across each detector. First, source and background regions with a typical radius of $\sim 1' - 1.5'$ were defined, with the background region selected to avoid bright sources, dead pixels, chip gaps, and anomalous CCDs. After correcting for vignetting effects in both the observation and blank-sky files with the routine `evigweight`, the effective area (A) of each region was calculated, as was the total count rate in the 10–12 keV band (R) for each detector.

A scaled blank-sky subtraction was then performed on the spectra (S) of each region,

$$S_{\text{Source}} = A_{\text{Obs, Src}} \left(\frac{S_{\text{Obs, Src}}}{A_{\text{Obs, Src}}} - Q \frac{S_{\text{Blank, Src}}}{A_{\text{Blank, Src}}} \right), \quad (1)$$

$$S_{\text{Bkg}} = A_{\text{Obs, Src}} \left(\frac{S_{\text{Obs, Bkg}}}{A_{\text{Obs, Bkg}}} - Q \frac{S_{\text{Blank, Bkg}}}{A_{\text{Blank, Bkg}}} \right), \quad (2)$$

where Q is the ratio in count rates,

$$Q = \frac{R_{\text{Obs}}}{R_{\text{Blank}}}. \quad (3)$$

The subtracted and scaled spectra were then subtracted a second time to produce the final spectra,

$$S = S_{\text{Source}} - S_{\text{Bkg}}. \quad (4)$$

The resulting spectrum for each detector was then

² <https://github.com/chrisopp12/xmm-esas-pipeline>

grouped to a minimum of 30 counts per bin and fit simultaneously in XSPEC (Arnaud 1996). An `apex` model for continuum plasma X-ray emission was combined with a `phabs` model for galactic absorption. To account for cross-calibration differences between detectors, a `const` component was added, with the value allowed to float on both MOS detectors. All detectors were fit simultaneously to produce a best-fit temperature for each cluster.

The best-fit temperature was then used to recalculate a source region with r_{500} defined by the relationship from Arnaud et al. (2005) to match the procedure from Uppedell et al. (2023):

$$E(z)r_{500} = B_{500} \left(\frac{T_X}{5 \text{ keV}} \right)^\beta, \quad (5)$$

where $E(z) = \sqrt{\Omega_M(1+z)^3 + \Omega_\Lambda}$, and constants $B_{500} = 1104 \text{ kpc}$ and $\beta = 0.57$. The double-subtraction and XSPEC fitting process was then repeated using the new source region. After fitting in the 0.3–10.0 keV band, the cross-calibration and temperature components were frozen and the `clumin` convolution model was used to calculate the luminosities in 0.1–2.4 and 0.5–2.0 keV bands.

Image processing was done with ESAS by first implementing `binadapt` with a bin factor of four and adaptively smoothing with `combimage` using a kernel sized to enclose 50 counts to produce a point-source-subtracted, exposure-corrected, smoothed image. Residual holes in the image from point-source masking were iteratively filled using the `inpaint_biharmonic` routine in `skimage.restoration` (van der Walt et al. 2014). Surface brightness contours varied in spacing depending on the observation, but were generally set to include 12 linearly spaced levels starting at $\sim 0.5\sigma$, where σ is the standard deviation of the XSB, and extending up to the maximum pixel value in the field.

Additional image processing was performed to qualitatively inspect sharp features in the XSB. The ESAS-processed image was reprojected onto an 800×800 pixel grid using `reproject_exact`, which conserves flux (Robitaille et al. 2020). After infilling holes in the image due to point source masking, the image was smoothed with a $10''$ Gaussian kernel and one-dimensional profiles were extracted across any suspected features. A map of the Gaussian gradient magnitude was also generated using the same $10''$ kernel to highlight sharp intensity gradients. Finally, an unsharp mask was produced by subtracting an image smoothed with a $50''$ kernel from the image smoothed at $10''$.

2.3. Member Galaxy Redshift Survey

Spectroscopic observations were carried out using the DEIMOS multi-object spectrograph (Faber et al. 2003) on the Keck II telescope between 2023 and 2025 as part of a multi-semester program. For each cluster, we designed two slitmasks to maximize spectroscopic coverage of likely cluster members and potential foreground and background structures. Targets for each mask were selected using Pan-STARRS photometric data, with priorities based on both brightness and likelihood of cluster membership. Specifically, we assigned each galaxy a weight proportional to

$$\frac{24 - r}{\sigma_{\text{PS}}} \exp \left(\frac{-(z_{\text{PS}} - z_{\text{cl}})^2}{2\sigma_{\text{PS}}^2} \right), \quad (6)$$

TABLE 6
CLUSTER INFORMATION FROM REDMAPPER

Name	Redshift	σ_z	Richness	σ_λ	RA [deg]	Dec [deg]	Alt. name(s)
RM J000343.8+100123.8	0.372	0.014	131	6	0.9325	10.0233	ACT-CL J0003.7+1001
RM J010934.2+330301.0	0.479	0.012	168	17	17.3923	33.0503	...
RM J021952.2+012952.2	0.364	0.014	127	6	34.9673	1.4978	ACT-CL J0219.9+0130
RM J080135.3+362807.5	0.511	0.014	125	17	120.3971	36.4688	...
RM J082944.9+382754.4	0.376	0.013	146	6	127.4372	38.4651	PSZ2 G183.30+34.98
RM J092647.3+050004.0	0.469	0.011	140	13	141.6970	5.0011	PSZ2 G227.89+36.58 ACT-CL J0926.7+0500
RM J104311.1+150151.9	0.417	0.012	121	8	160.7962	15.0311	...
RM J121917.6+505432.8	0.535	0.015	165	23	184.8232	50.9091	PSZ2 G135.17+65.43
RM J125725.9+365429.4	0.520	0.013	138	17	194.3580	36.9082	...
RM J132724.2+534656.5	0.386	0.013	121	6	201.8506	53.7823	...
RM J163509.2+152951.5	0.472	0.011	143	13	248.7885	15.4976	ACT-CL J1635.1+1529
RM J232104.1+291134.5	0.494	0.011	239	22	350.2673	29.1929	PSZ2 G100.22-29.64

Note. – All properties from Rykoff et al. (2016).

where r is the r -band apparent magnitude and z_{PS} and σ_{PS} are the photometric redshift and its uncertainty from the Pan-STARRS catalog, respectively. Because the Pan-STARRS photometric redshifts have substantial uncertainty (~ 0.15), this weighting allows for some focus on the cluster redshift while retaining sensitivity to foreground and background structures. The purpose of the magnitude weighting is to prioritize brighter galaxies (those more likely to successfully yield a redshift) within the target cluster. A side effect of the magnitude weighting is that foreground galaxies are more likely to be targeted than background galaxies. These weights were input into the `dsimulator` software to prioritize slit placement. We excluded stars based on Pan-STARRS morphology and avoided targeting galaxies with existing spectroscopic redshifts, except on the outskirts of the field of view, where redundancy was used for consistency checks.

Table 7 lists the masks and corresponding DEIMOS configurations. While the specifics of each observation are dependent on cluster redshift and observing conditions, the same general approach was applied to all clusters. All masks utilized the 1200G grating, giving a dispersion of $\sim 0.33 \text{ \AA pixel}^{-1}$ and a spectral resolution of $\sim 1 \text{ \AA}$, corresponding to a velocity resolution of $\sim 40 \text{ km s}^{-1}$. The wavelength coverage varied with cluster redshift so that it consistently included rest-frame features from the 3727 \AA [O II] doublet to the 5177 \AA magnesium line. (Within a mask, the exact wavelength coverage depends on the slit position, but always covers these lines for galaxies in the target cluster.)

The baseline plan was for three 900-second exposures on each mask, but exposure times were shortened (and in a few cases lengthened) as needed to complete the masks within the allotted night. The ‘‘B’’ mask for RMJ1257 is omitted from Table 7 because it received almost no exposure time and yielded no redshifts. Conversely, a third mask was designed for RMJ1635 to fill a gap in target scheduling, and RMJ0829 mask A was observed with approximately double the standard exposure time over two nights for a similar reason. The mask name

TABLE 7
DEIMOS CONFIGURATIONS

Cluster	Mask	Date (UT)	Exp [s]	Wavelength [\AA]
RMJ0003	A	2023 Sept 8	2520	4680-7320
	B	2023 Sept 14	2700	4680-7320
RMJ0109	A	2023 Sept 14	2160	5180-7820
	B	2023 Sept 14	2160	5180-7820
RMJ0219	A	2023 Sept 14	2700	4680-7320
	B	2023 Sept 14	2700	4680-7320
RMJ0801	A	2023 April 4	1800	5370-8010
	B	2023 April 4	1800	5370-8010
RMJ0829	A	2025 Feb 23, 24	6300	4780-7420
	B	2025 Feb 23	2700	4780-7420
RMJ0926	A	2025 Feb 23	2700	5080-7720
	B	2025 Feb 23	2700	5080-7720
RMJ1043	A	2025 Feb 23	2700	4930-7570
	B	2025 Feb 23	2580	4930-7570
RMJ1219	A	2023 April 23	1800	5370-8010
	B	2023 April 23	1800	5370-8010
RMJ1257	A	2022 July 1	2340	5370-8010
RMJ1327	A	2025 Feb 24	2280	4780-7420
	B	2025 Feb 23	2700	4780-7420
RMJ1635	A	2023 April 12	3240	5180-7820
	B	2023 April 23	3240	5370-8010
	C	2023 Sept 8	2160	5370-8010
RMJ2321	A	2023 Sept 8	2160	5180-7820
	B	2023 Sept 14	2700	5180-7820

listed in the Keck Science Archive can be constructed from Table 7 by combining the four digits in the cluster name with the mask letter, for example *0926B* or *1635C*.

We reduced the data using `PypeIt` (Prochaska et al. 2020), which performs wavelength calibration, sky subtraction, and extraction of 1D spectra. Redshifts were measured with a custom cross-correlation algorithm that compares each spectrum to a set of redshifted galaxy templates, following the procedure detailed in Wittman et al. (2023), with typical uncertainties of $\lesssim 10^{-4}$.

Each mask was designed with ~ 100 slits and yielded

~ 70 secure redshifts. These new redshifts were combined with archival results in a $10'$ radius circle around the cluster from SDSS (Kollmeier et al. 2019), BOSS (Dawson et al. 2013), and DESI (DESI Collaboration et al. 2025). The complete sample of redshifts was then used to identify cluster members as well as foreground and background structures.

2.4. Red Sequence Selection and Luminosity Density

We identified red sequence galaxies using DESI Legacy Survey (Dey et al. 2019) photometry in the g and r bands. For each cluster, we extracted sources within a $10'$ radius around the cluster center and constructed a color-magnitude diagram (CMD) using $g - r$ color versus r -band magnitude. Sources with missing or invalid photometry were removed.

We cross-matched the photometric catalog with available spectroscopic redshifts to isolate confirmed cluster members. A linear red sequence was then fit in $g - r$ versus r using these members with iterative σ -clipping to remove outliers and obtain a robust slope and intercept. We defined red sequence candidates as photometric sources lying within ± 0.2 mag of the best-fit relation and added them to our catalog of cluster members identified by spectroscopy.

Each cluster member was then assigned a luminosity weight using its r -band magnitude:

$$w_L = 10^{-0.4r}, \quad (7)$$

which serves as a proxy for stellar luminosity. These weights were then used to construct a smoothed luminosity-weighted spatial density map, generated by applying a Gaussian kernel density estimator with `scipy.stats.gaussian_kde` (Virtanen et al. 2020). Density contours varied in spacing depending on the observation, but were typically constructed with 12 linearly spaced levels from the minimum to maximum weighted density values, with the lowest contour omitted for clarity.

3. RESULTS AND DISCUSSION

3.1. X-Ray Analysis

X-ray temperatures and luminosities were determined following the procedure described in §2.2, with results shown in Table 8. We use the scaling relations provided in Upsdell et al. (2023) to compare fitted temperatures and luminosities to expected values at the given richness, assuming self-similar evolution. These relations do not explicitly account for selection effects. However, we use relations derived from an optically selected sample, which includes X-ray faint sources (those not detected in the XMM Cluster Survey, possibly due to low exposure time or off-axis positioning on the detector) at an estimated upper-limit luminosity to reduce bias towards X-ray bright sources.

Looking at the richness–temperature scaling relation from Upsdell et al. (2023),

$$\log\left(\frac{T_X}{E(z)^{2/3}T_0}\right) = \log(A_T) + B_T \log\left(\frac{\lambda}{\lambda_0}\right) \pm \sigma_T, \quad (8)$$

with $E(z)$ given by Equation 5 and fitting parameters $A_T = 1.13$, $B_T = 0.62$, $T_0 = 2.5$ keV, $\lambda_0 = 60.0$, and

$\sigma_T = 0.23$ is given in natural log space, we would expect temperatures of ~ 5 – 6 keV for clusters of this richness and redshift (except for RMJ2321, which has an expected temperature of 7.9 keV), shown in Figure 3.

To assess the significance of deviations from the relation, we compare the logarithmic offset between the observed and expected temperatures to the quadrature sum of the intrinsic scatter and the observational uncertainty,

$$\sigma = \sqrt{\sigma_{\ln, \text{obs}}^2 + \sigma_T^2}, \quad (9)$$

where $\sigma_{\ln, \text{obs}} = \sigma_{\text{obs}}/T_X$ is the observational uncertainty in natural log space (*i.e.*, the fractional uncertainty). Three clusters (RMJ0003, RMJ0801, and RMJ0926) have temperatures more than 1σ greater than predicted by the scaling relation, while two clusters (RMJ1043 and RMJ0219) lie more than 1σ below the predicted value.

Fitted luminosities in both the 0.1–2.4 and 0.5–2.0 keV

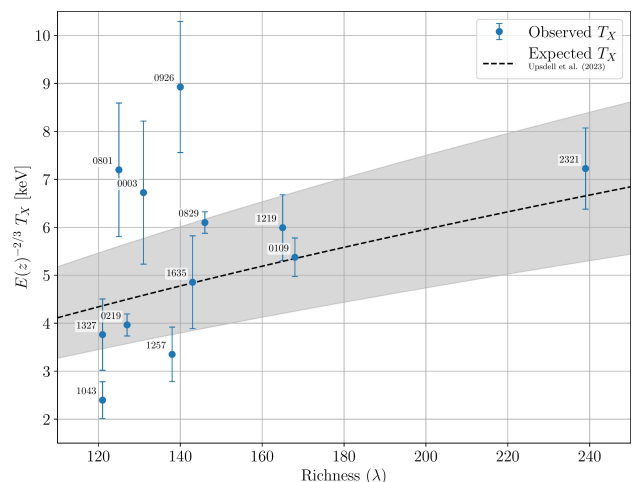


FIG. 3.— X-ray temperature, with self-similar correction $E(z)^{-2/3}$, versus richness with scaling relation given in Equation 8. The shaded region gives 1σ uncertainty in the scaling relation by Upsdell et al. (2023).

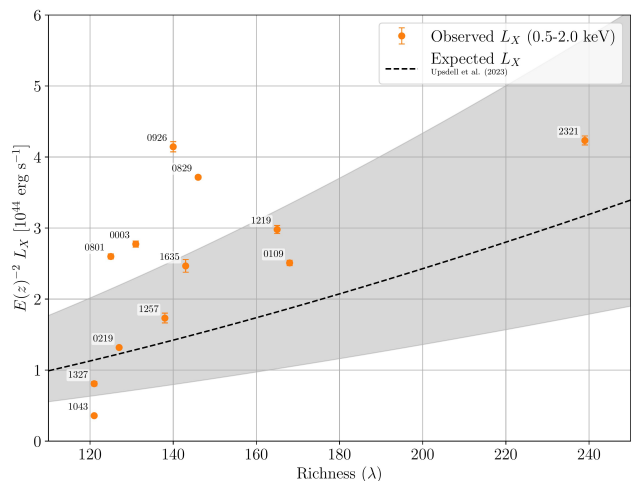


FIG. 4.— X-ray luminosity in the 0.5–2.0 keV band, with self-similar correction $E(z)^{-2}$, versus richness with scaling relation given in Equation 10. The shaded region gives 1σ uncertainty in the scaling relation by Upsdell et al. (2023).

TABLE 8
XMM-Newton OBSERVATION RESULTS

Name	Obs ID	Exposure [ks]				T_X [keV]	L_X [10^{44} erg s $^{-1}$]	
		Nominal	Usable				0.5–2.0 keV	0.1–2.4 keV
			MOS1	MOS2	PN			
RMJ0003	0881900801	38.9	21.6	21.9	13.8	7.65 ± 1.70	$4.09^{+0.063}_{-0.062}$	$6.60^{+0.093}_{-0.092}$
RMJ0109	0922150401	28.9	17.2	17.3	14.8	6.38 ± 0.48	$4.19^{+0.063}_{-0.062}$	$6.78^{+0.101}_{-0.100}$
RMJ0219	0922150601	36.6	24.6	24.6	21.7	4.50 ± 0.26	$1.93^{+0.026}_{-0.025}$	$3.13^{+0.041}_{-0.041}$
RMJ0801	0881901001	24.0	22.1	22.3	20.4	8.65 ± 1.67	$4.51^{+0.062}_{-0.061}$	$7.26^{+0.100}_{-0.098}$
RMJ0829	0901870901	28.0	26.7	25.2	24.5	6.95 ± 0.26	$5.50^{+0.035}_{-0.035}$	$8.89^{+0.057}_{-0.057}$
RMJ0926	0901870201	19.0	7.9	8.0	4.9	10.55 ± 1.62	$6.84^{+0.120}_{-0.118}$	$10.99^{+0.192}_{-0.189}$
RMJ1043	0922150301	21.0	19.7	19.7	17.5	2.77 ± 0.44	$0.56^{+0.024}_{-0.023}$	$0.91^{+0.039}_{-0.038}$
RMJ1219	0881900301	30.0	17.5	18.6	10.1	7.27 ± 0.83	$5.32^{+0.103}_{-0.101}$	$8.58^{+0.166}_{-0.163}$
RMJ1257	0881900701	14.0	12.6	12.4	1.1	4.04 ± 0.68	$3.04^{+0.123}_{-0.118}$	$4.95^{+0.200}_{-0.193}$
RMJ1327	0881901201	28.7	10.9	10.3	12.4	4.31 ± 0.85	$1.21^{+0.048}_{-0.046}$	$1.97^{+0.078}_{-0.075}$
RMJ1635	0881900501	18.8	15.6	16.3	4.0	5.74 ± 1.14	$4.09^{+0.151}_{-0.145}$	$6.62^{+0.244}_{-0.235}$
RMJ2321	0922150101	17.9	13.9	13.8	11.8	8.62 ± 1.01	$7.20^{+0.108}_{-0.106}$	$11.59^{+0.173}_{-0.171}$

Note. – RMJ1257 was fit using only MOS detectors due to proton flaring.

bands are listed in Table 8. The richness–luminosity scaling relation used in [Upsdell et al. \(2023\)](#),

$$\log\left(\frac{L_X}{E(z)^2 L_0}\right) = \log(A_L) + B_L \log\left(\frac{\lambda}{\lambda_0}\right) \pm \sigma_L, \quad (10)$$

with $A_L = 0.57$, $B_L = 1.5$, $L_0 = 0.7 \times 10^{44}$ erg s $^{-1}$, $\lambda_0 = 60.0$, and $\sigma_L = 0.58$, utilizes the 0.5–2.0 keV band and is shown in Figure 4. Only one of our clusters, RMJ1043, has a luminosity significantly below the prediction, while four (RMJ0003, RMJ0801, RMJ0829, and RMJ0926) lie more than 1σ above, where the uncertainty is again given in natural log space, $\sigma = \sqrt{(\sigma_{\text{obs}}/L_X)^2 + \sigma_L^2}$. RMJ0926 exhibits the largest positive deviation from the expected relations in both luminosity and temperature, with offsets of 1.8σ and 2.7σ respectively, and appears to be a prime candidate for a binary dissociative merger. All of these systems are discussed at length in §3.3.

3.2. Redshift and Cluster Member Analysis

A summary of redshift results is shown in Table 9, including the number of archival members within $10'$ of the cluster and the number of new spectroscopic results from DEIMOS. The cluster redshift range was determined from the redshift distribution, including both archival and new results. That redshift range was then used to define a red sequence and identify additional cluster members from Legacy photometry as described in §2.4. The full redshift catalog is available in machine-readable form; a portion is shown in Appendix A (Table 34).

3.3. Individual Cluster Analysis

3.3.1. RM J000343.8+100123.8

Our first cluster, RMJ0003, is the second-lowest redshift cluster in the sample at $z = 0.372$ (Table 6). The top priority BCG from redMaPPer barely meets our 0.98

TABLE 9
REDSHIFT AND MEMBERSHIP SUMMARY

Name	Redshift Range	Redshifts		Members	
		Arch.	New	Spec.	CMD
RMJ0003	$0.360 \leq z \leq 0.385$	113	101	91	468
RMJ0109	$0.449 \leq z \leq 0.470$	22	123	71	371
RMJ0219	$0.355 \leq z \leq 0.375$	178	119	108	1110
RMJ0801	$0.485 \leq z \leq 0.520$	153	96	62	479
RMJ0829	$0.380 \leq z \leq 0.410$	110	147	119	588
RMJ0926	$0.445 \leq z \leq 0.475$	208	143	89	585
RMJ1043	$0.420 \leq z \leq 0.440$	65	154	61	631
RMJ1219	$0.535 \leq z \leq 0.566$	126	118	75	432
RMJ1257	$0.520 \leq z \leq 0.540$	139	39	31	320
RMJ1327	$0.380 \leq z \leq 0.420$	151	171	124	616
RMJ1635	$0.465 \leq z \leq 0.485$	83	143	76	792
RMJ2321	$0.480 \leq z \leq 0.510$	95	115	113	775

TABLE 10
RMJ0003 BCG INFORMATION

BCG	Probability	Redshift	r -mag ^d	RA [deg]	Dec [deg]
1	0.9680	0.374 ^a	18.12	0.93249	10.02327
2	0.0293	0.377 ^b	18.49	0.95326	10.05429
3	0.0020	0.364 ^b	18.60	0.92447	10.01528
4	0.0007	0.372 ^b	19.15	0.95263	10.03755
5	0.0000	0.369 ^c	19.60	0.92024	10.02599

^aSDSS DR18 ([Almeida et al. 2023](#))

^bDESI DR1 ([DESI Collaboration et al. 2025](#))

^cDEIMOS (This work)

^dDESI Legacy Survey DR10 ([Dey et al. 2019](#))

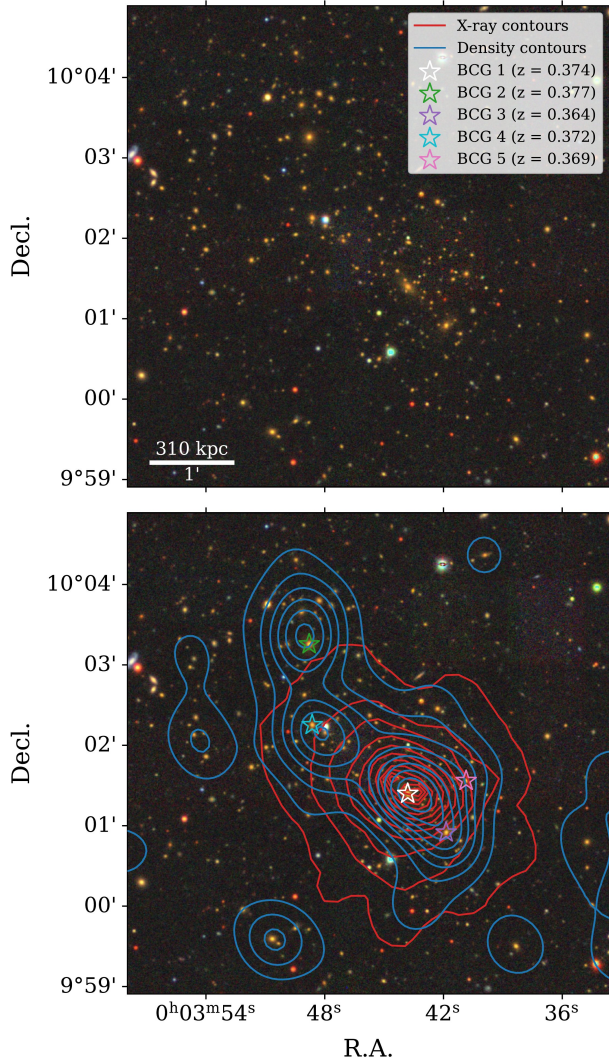


FIG. 5.— Optical image of RMJ0003. Top panel: 6' by 6' (1.86 by 1.86 Mpc) Legacy Survey image. Bottom panel: red sequence density contours (blue), X-ray surface brightness contours (red), and BCG candidates identified by redMaPPer.

probability threshold at 0.9680, shown in Table 10. In Figure 5, we can see that the X-ray surface brightness is largely centered on BCG 1 and elongated towards BCG 4. The X-ray emission also shows a second peak between BCGs 1 and 4, offset ≈ 100 kpc from BCG 1. Luminosity-weighted galaxy density contours show three individual structures, each collocated with one of the identified BCGs.

Looking at the spatial redshift distribution in the bottom panel of Figure 6, there is some clustering of lower redshift members near BCG 1 and higher redshift members near BCG 2, indicating possible separate subclusters. The redshift distribution of all galaxies in a 10' radius is shown in the top panel, with the inset showing all members between $0.360 \leq z \leq 0.385$ in the same field. There is a small background structure at $z \approx 0.75$ with 12 spectroscopic members, which are all located southwest of our cluster and do not contaminate the observed X-ray emission. To determine if there are distinct subclus-

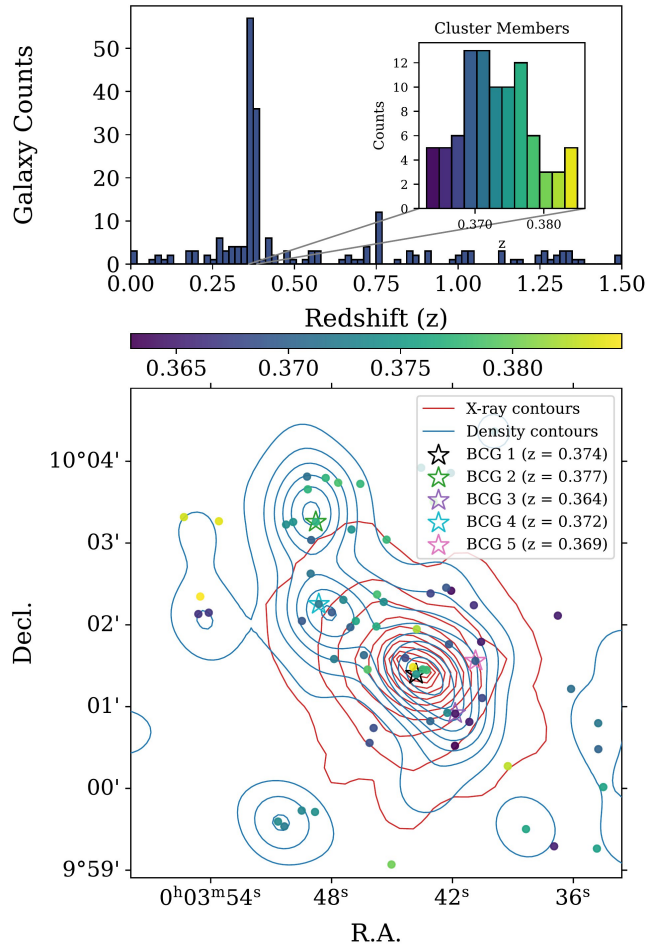


FIG. 6.— Redshift distribution of RMJ0003. Top panel: histogram of spectroscopic redshifts, combining archival data within 10' of the cluster with new observations from DEIMOS. The inset highlights galaxies in the redshift range $0.360 \leq z \leq 0.385$, which are classified as cluster members. Bottom panel: spatial distribution of those same members.

ter distributions in redshift-space, we fit a Gaussian mixture model (GMM) with one, two, and three components to the cluster redshift distribution. A single-component model is preferred, with a Bayesian Information Criterion $\text{BIC} = -690$ compared to -679 and -668 for two- and three-component models, respectively. We find the same one-component fit consistent with a Gaussian distribution according to both the Kolmogorov–Smirnov (KS) ($D = 0.070$, $p = 0.73$) and Anderson–Darling³ (AD) ($A^2 = 0.46$, $p = 0.26$) tests.

To further explore the possible substructure in the cluster, we divided the cluster into three regions, each containing one of the BCGs associated with a density peak. The boundaries of these regions were defined by

³ For the KS test, the statistic D is the maximum absolute difference between the empirical cumulative distribution function and that of a reference Gaussian distribution, and is primarily sensitive to global deviations. The Anderson–Darling statistic, A^2 , places greater weight on deviations in the distribution tails. A^2 is typically reported in reference to tabulated critical values where $A^2 \lesssim 0.55$ are consistent with a Gaussian distribution at better than a 15% significance level, while values $\gtrsim 1$ strongly disfavor a normal distribution (Stephens 1974). Reported AD p-values are computed using the Monte Carlo option in `scipy.stats.anderson`.

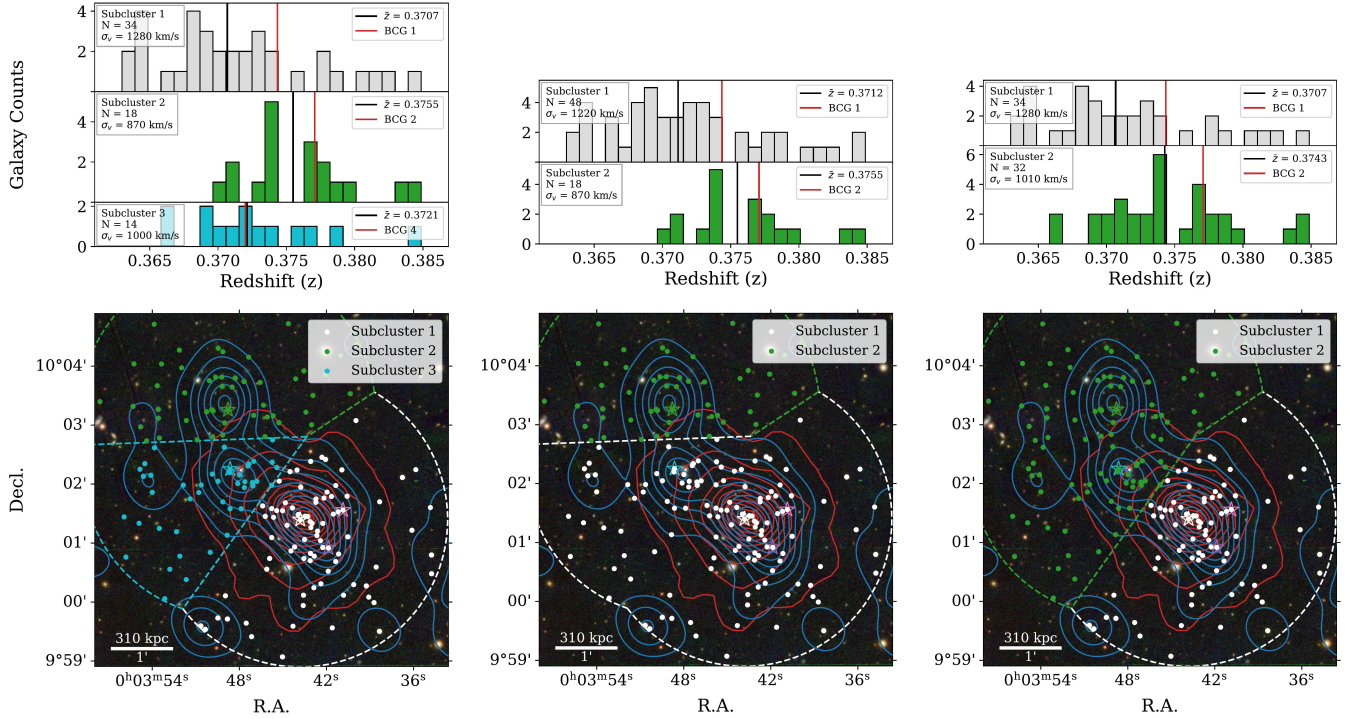


FIG. 7.— Subclustering analysis of RMJ0003. Bottom panels: spatial distribution of subcluster members, both spectroscopic and photometric, identified within regions defined by the bisector between BCG pairs and a radial distance of $2.5'$ from the BCG in each region. Top panels: redshift distribution of the spectroscopic members. The two right panels consider the subcluster associated with BCG 4 to be part of Subcluster 1 or 2.

the bisectors between BCGs 1, 2, and 4 and a $2.5'$ radius from the associated BCG, shown in the bottom left panel of Figure 7. Individual members, both spectroscopic and those identified through red-sequence, were determined from spatial location without additional redshift cuts. The top left panel shows the redshift distribution of the spectroscopic members. Subclusters 1 and 2 (corresponding to BCGs 1 and 2) show a distinct separation in redshift ($\Delta v_{\text{LOS}} = 1430 \text{ km s}^{-1}$ between subcluster means and 590 km s^{-1} between BCGs), while Subcluster 3 (BCG 4) appears more uniformly distributed across the cluster redshift range. Each subcluster is individually consistent with a normal distribution by both KS and AD tests.

Given the difference in mean redshift between Subclusters 1 and 2 (Table 11), we consider them to be distinct groups. To explore Subcluster 3 further, we considered scenarios that separately combine Subclusters 1 and 3 and Subclusters 2 and 3, shown in the center and right panels of Figure 7, respectively. Grouping Subclusters 1 and 3 together reduces the velocity dispersion of Subcluster 1 to 1220 km s^{-1} (from 1280 km s^{-1}) while the grouping of 1 and 2 increases the dispersion of Subcluster 2 to 1010 km s^{-1} . The similarity in redshift distribution between Subclusters 1 and 3, along with an elevated temperature and luminosity ($0.5\text{--}2.0 \text{ keV}$ and $4.09 \times 10^{44} \text{ erg s}^{-1}$ (Table 8) versus expected values of 5.22 keV and $1.90 \times 10^{44} \text{ erg s}^{-1}$, indicates those subclusters are likely involved in an active merger near the plane of the sky.

The role of Subcluster 2 is more ambiguous. The lack

TABLE 11
RMJ0003 SUBCLUSTER PROPERTIES

Subcluster	N	BCG	BCG z	Mean z	σ_v [km s^{-1}]
All	91	0.3731	1160
1	34	1	0.374	0.3707	1280
2	18	2	0.377	0.3755	870
3	14	4	0.372	0.3721	1000

of X-ray emission suggests gas-stripping and a low impact parameter post-pericenter scenario, or a low-mass subcluster. In a low impact parameter scenario, the subclusters would be on a radial trajectory where the line-of-sight (LOS) velocity component between subclusters and an on-sky separation of 700 kpc between BCGs 1 and 2 would produce a 3D separation of $\approx 1 \text{ Mpc}$. A significant LOS velocity at that separation would imply a moderate or low mass ratio merger while the complete stripping of the gas would favor a larger mass ratio between subclusters.

We believe the more likely scenario is a low-mass Subcluster 2. The luminosity density contours in the region are heavily dominated by BCG 2. Using unweighted density, the peak nearly vanishes while peaks at Subclusters 1 and 3 remain. Further, there is a large foreground galaxy that is likely obscuring members of Subcluster 3, falsely diminishing the local density. If the involvement with Subcluster 2 is minimal, the interaction between Subclusters 1 and 3 could still be well-modeled as a binary merger. This ambiguity, along with the elongated morphology and second X-ray peak between BCGs 1 and 4, leads us to not discount this cluster for possible future

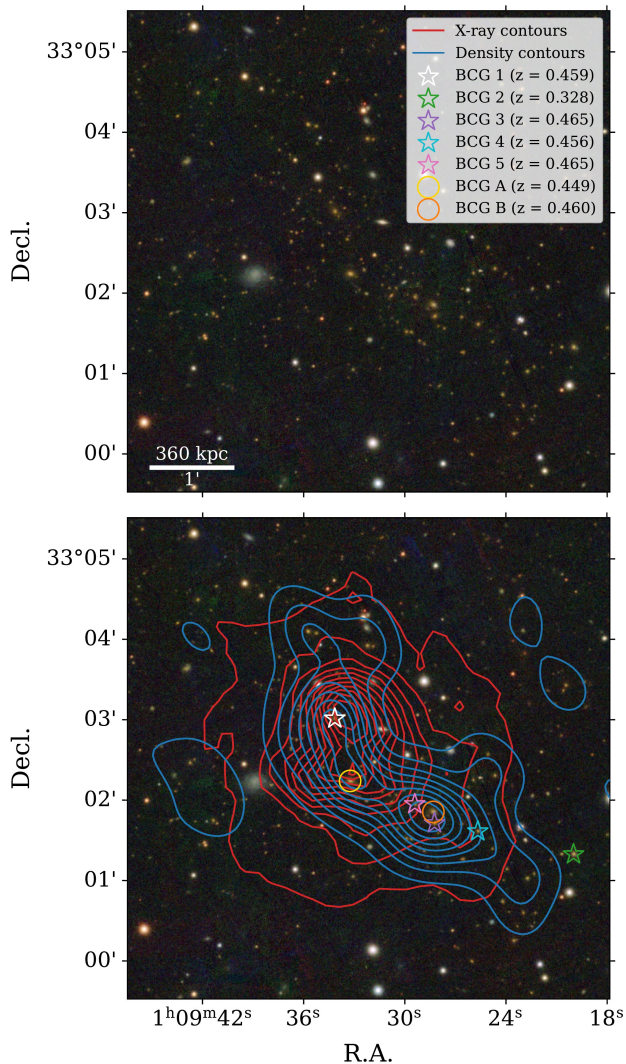


FIG. 8.— Optical image of RMJ0109. Top panel: $6'$ by $6'$ (2.16 by 2.16 Mpc) Pan-STARRS image. Bottom panel: red sequence density contours (blue), X-ray surface brightness contours (red), and BCG candidates identified by redMaPPer and this work.

follow-up. Weak lensing would provide the clearest picture, but additional spectroscopy targeted on Subcluster 2 would help resolve any LOS velocity component and provide a mass estimate for that subcluster.

3.3.2. RM J010934.2+330301.0

Our second cluster, RMJ0109, illustrates some issues with redMaPPer BCG selection that are relevant to a few of our other targets as well. RedMaPPer identifies two primary BCG candidates with probabilities of 0.9195 and 0.0750 (Table 12). However, a visual inspection suggests that the brightest galaxy consistent with the cluster red sequence is the one near the center of Figure 8, just south of the small X-ray contour. This galaxy has an r -band magnitude of 18.56 as compared to the 18.62 for BCG 1 and SDSS spectroscopy identifies the galaxy at $z = 0.44910$, making it the lowest redshift galaxy we define as in the cluster. We have marked this galaxy as an additional possible BCG, labeled BCG A, and adopted a

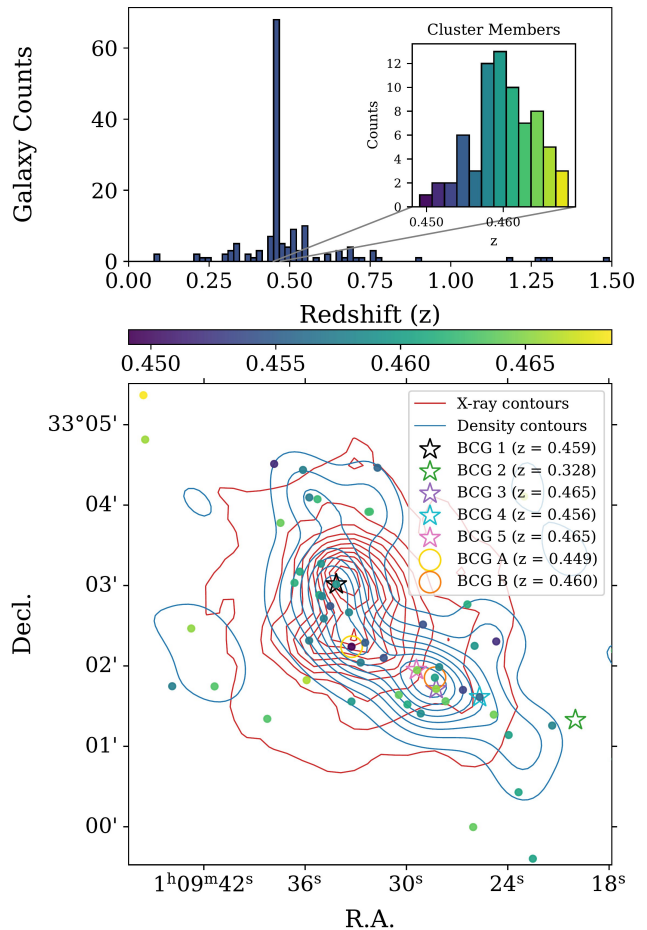


FIG. 9.— Redshift distribution of RMJ0109. Top panel: histogram of spectroscopic redshifts, combining archival data within $10'$ of the cluster with new observations from DEIMOS. The inset highlights galaxies in the redshift range $0.449 \leq z \leq 0.470$, which are classified as cluster members. Bottom panel: spatial distribution of those same members.

TABLE 12
RMJ0109 BCG INFORMATION

BCG	Probability	Redshift	r -mag ^c	RA [deg]	Dec [deg]
1	0.9195	0.459 ^a	18.62	17.39234	33.05028
2	0.0750	0.328 ^a	18.88	17.33332	33.02213
3	0.0031	0.465 ^b	19.64	17.36767	33.02857
4	0.0020	0.456 ^a	19.99	17.35695	33.02684
5	0.0004	0.465 ^a	19.74	17.37253	33.03254
A	...	0.449 ^b	18.56	17.38853	33.03734
B	...	0.460 ^b	19.04	17.36798	33.03092

^aDEIMOS (This work)

^bSDSS DR18 (Almeida et al. 2023)

^cDESI Legacy Survey DR10 (Dey et al. 2019)

convention of using letters to signify BCGs not classified by redMaPPer. It is not immediately clear to us why redMaPPer does not include BCG A in its list of top five BCG candidates. The redMaPPer algorithm incor-

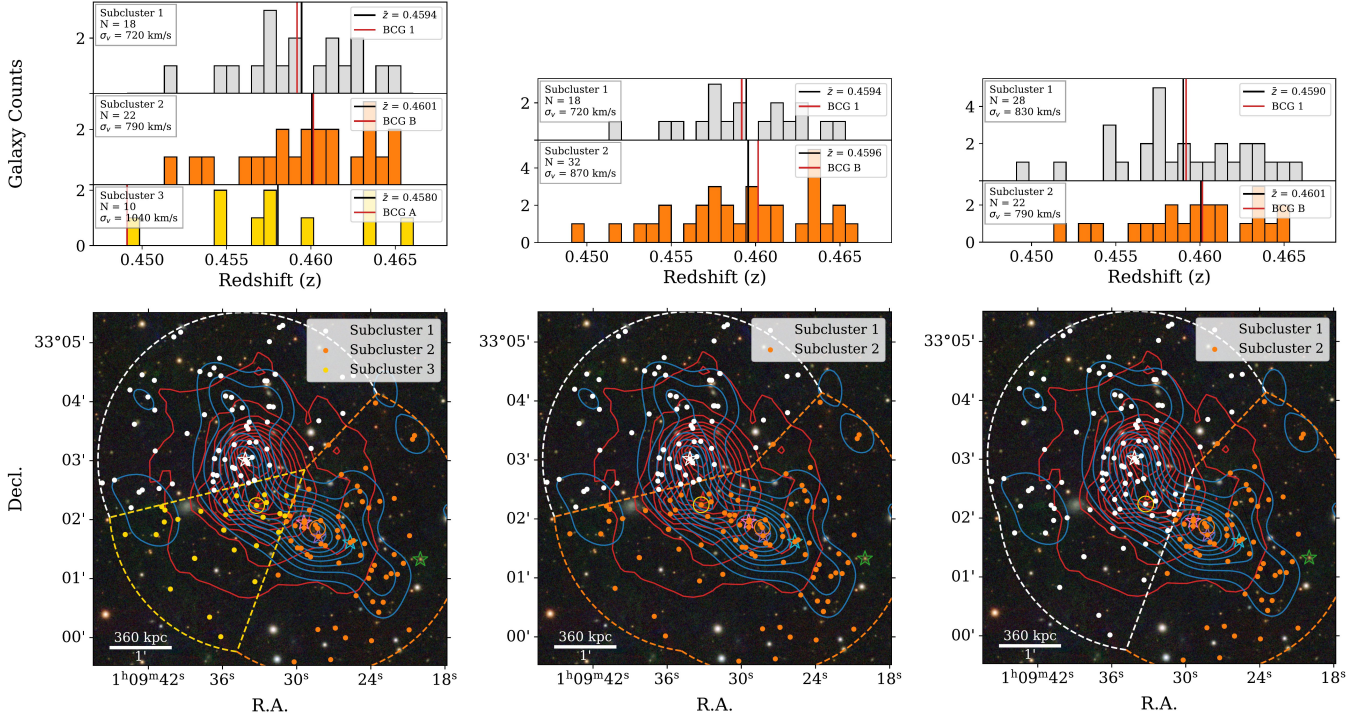


FIG. 10.— Subclustering analysis of RMJ0109. Bottom panels: spatial distribution of subcluster members, both spectroscopic and photometric, identified within regions defined by the bisector between BCG pairs and a radial distance of $2.5'$ from the BCG in each region. Top panels: redshift distribution of the spectroscopic members. The two right panels consider the subcluster associated with BCG A to be part of Subcluster 1 or 2.

porates local galaxy density when identifying potential BCG candidates. Although BCG A lies near the cluster center and appears on an extension of the primary peak in the luminosity-weighted galaxy density map, the unweighted galaxy number density in its immediate vicinity is relatively low, suggesting a possible explanation.

Another bright galaxy ($r = 19.04$), labeled BCG B in Figure 8, is also not listed among the BCG candidates. However, in this case, the reason may be that it is blended with a bluer foreground galaxy. The SDSS spectrum⁴ shows a blend of early and late type spectra at different redshifts; the SDSS pipeline correctly identified only the strong emission lines at $z = 0.17895$. We model the spectrum as the sum of this SDSS model (with freely varying amplitude) plus an early-type model with freely varying amplitude, redshift, and dust reddening. We find the redshift of the early type galaxy to be 0.46015 ± 0.00008 . The composite model fits the data substantially better, with $\Delta\chi^2 = 166$ for three additional parameters. We therefore consider this galaxy to be in the cluster. Note that this new redshift does not appear in Table 34 because that table pertains only to Keck/DEIMOS redshifts.

Finally, the galaxy identified by redMaPPer as BCG 2 is actually a foreground galaxy, spectroscopically confirmed by SDSS at $z = 0.32846$. Because redMaPPer does not use spectroscopic information, the color of the galaxy is similar enough to be misidentified. Of note, this galaxy was not classified as a member of our red

⁴ Available from <https://skyserver.sdss.org/dr19/VisualTools/explore/summary?id=1237680316595175986>

TABLE 13
RMJ0109 SUBCLUSTER PROPERTIES

Subcluster	N	BCG	BCG z	Mean z	σ_v [km s^{-1}]
All	71	0.4601	870
1	18	1	0.459	0.4594	720
2	22	B	0.460	0.4601	790
3	10	A	0.449	0.4580	1040

sequence fit, being bluer than the fit by 0.216 mag (accepted members lie within ± 0.2 mag).

To summarize the multiple BCG issues in reverse order: a foreground galaxy had similar enough color to be assigned as BCG 2; a galaxy with brighter apparent magnitude than BCG 3 was not identified as a BCG candidate, possibly due to blending with a foreground galaxy; and the brightest galaxy was overlooked with no definitive explanation. The blending issue is unique to this cluster, but the other two issues are relevant to some of our other targets. This suggests that a more robust selection approach could be developed based on additional inputs beyond redMaPPer's BCG ranking (for example, spectroscopic information or redMaPPer's complete list of possible member galaxies).

Turning our attention to BCGs 3, 4, and 5, we see in Figure 8 that they likely reside in a subcluster in the southwest with BCG B. Galaxy luminosity density contours show a peak between BCGs 3 and 5, and the X-ray emission is extended to the southwest. All three of these BCGs have comparatively faint magnitudes (19.64–19.99) and redMaPPer probabilities less than 0.3%.

The distribution of galaxies in redshift space, shown in

the top panel of Figure 9, is best-fit by a one-component Gaussian (BIC of -567 compared to -555 for a two-component model) in the cluster region. Across the full redshift range, a GMM identifies a background subcluster at $z \sim 0.52$. However, these background galaxies are located in two primary groups northeast and southwest of the cluster and do not spatially overlap with the merging system or contribute to the observed X-ray morphology. The spatial distribution of cluster members, shown in the bottom panel of Figure 9, does not show any clear gradient in redshift or separation between subclusters.

Given the low redshift of BCG A ($\Delta v_{\text{LOS}} = 2200 \text{ km s}^{-1}$ as compared with BCG 1), we examined the redshift distribution in three distinct regions corresponding with BCGs 1, A, and B (including BCGs 3–5 collectively) (Figure 10). Of these three potential subclusters, Subcluster 3 has the largest velocity dispersion and fewest members (Table 13). Further, we find no other low redshift members in the vicinity of BCG A and thus explore the possibility of BCG A being part of either a southern subcluster with BCG B or the northern subcluster with BCG 1, shown in the center and right panels of Figure 10 respectively. In either scenario, both subclusters have similar mean redshifts with $\Delta v_{\text{LOS}} < 230 \text{ km s}^{-1}$ between subclusters and velocity dispersions of $\sim 800 \text{ km s}^{-1}$.

RMJ0109 is the second richest cluster in our sample, with a richness of 168, given in Table 6. Given this richness, the temperature and luminosity of 6.38 keV and $4.19 \times 10^{44} \text{ erg s}^{-1}$, respectively, are not immediately indicative of a post-pericenter merger. However, the X-ray morphology is clearly disturbed and double-peaked and, despite the BCG confusion, this is a reasonable candidate for a bimodal, or more complicated, merger. The BCG candidates are strung out along a NE-SW axis, while the XSB is highly concentrated at the NE end of that string. Furthermore, the galaxy luminosity distribution shows two peaks. The merger action may be primarily between groups headed by BCG A and BCG 1, which span the region of highest XSB. In this scenario, BCGs 3–5 and B perhaps form an infalling group or highlight a filament but are not necessarily part of the current merger action. On the other hand, BCGs 1 and B are separated by $>0.95'$ and there could be an argument for a merger between groups headed by BCG 1 (perhaps including BCG A) and BCG B (including BCGs 3–5).

It should be noted that, had BCG A been identified by redMaPPer as one of the top two BCG candidates, this cluster would have been excluded from our sample based on a projected separation of $<0.95'$ between BCGs 1 and A. Furthermore, spectroscopy shows that BCG 2 is not a cluster member, rendering the separation between BCGs 1 and 2 physically irrelevant. While the inclusion of this system does not strictly follow our original intent of selecting clusters whose two most likely BCGs trace distinct subclusters, it highlights that ambiguity in the primary BCG identification alone can be indicative of merging activity.

We believe this cluster would be a good candidate for lensing follow-up to determine the morphology of the mass distribution. This would provide a firmer foundation for identifying the subclusters involved, a key issue not resolved by the BCG information. This would also be

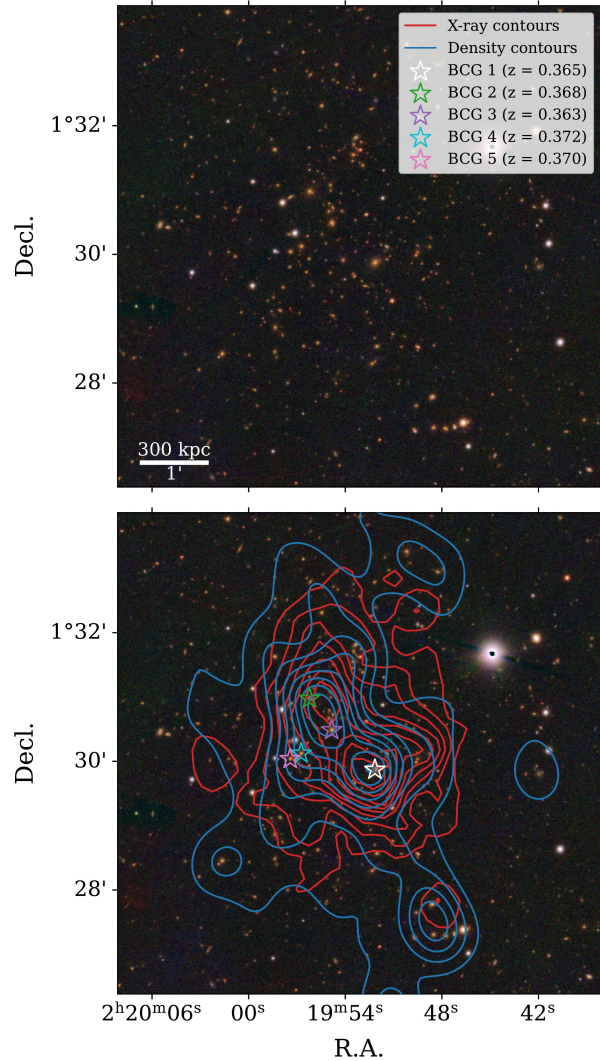


FIG. 11.— Optical image of RMJ0219. Top panel: $7.5'$ by $7.5'$ (2.25 by 2.25 Mpc) Pan-STARRS image. Bottom panel: red sequence density contours (blue), X-ray surface brightness contours (red), and BCG candidates identified by redMaPPer.

a good candidate for further spectroscopic study. Prior to this work, there were only 22 archival redshifts within $10'$ of the cluster, the least of any cluster in our sample. We increase that number to 145, with 71 spectroscopic members including 50 within $2.5'$ of BCGs 1, A, or B, but a more complete spectroscopic picture could help to disentangle the underlying structure.

3.3.3. RM J021952.2+012952.0

RMJ0219 displays a clear spatial separation between two subclusters with BCG 1 southwest of BCGs 2 and 3 (Figure 11). BCG 1 has a probability of 0.8577, while BCGs 2 and 3 have lower, but non-negligible, probabilities of 0.0871 and 0.0548, respectively (Table 14). BCGs 4 and 5 are both on the eastern edge of the cluster. They are not associated with any overdensities of galaxies or X-ray emission, and are unlikely to be representative of any underlying substructure. Both the XSB and galaxy luminosity density are elongated along a NE-SW axis and

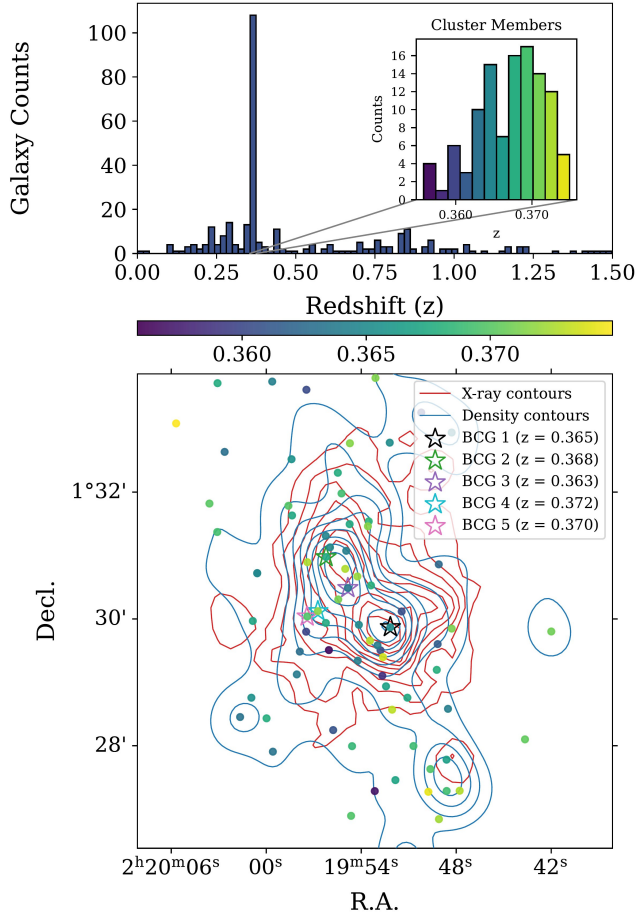


FIG. 12.— Redshift distribution of RMJ0219. Top panel: histogram of spectroscopic redshifts, combining archival data within $10'$ of the cluster with new observations from DEIMOS. The inset highlights galaxies in the redshift range $0.355 \leq z \leq 0.375$, which are classified as cluster members. Bottom panel: spatial distribution of those same members.

double-peaked, with one peak at BCG 1 and the other between BCGs 2 and 3. There is a small group in the southwest with an overdensity in both galaxies and X-ray emission. This group may be underrepresented, with foreground galaxies obscuring some members. However, the overall contribution to the cluster dynamics does not appear significant.

TABLE 14
RMJ0219 BCG INFORMATION

BCG	Probability	Redshift	r -mag ^d	RA [deg]	Dec [deg]
1	0.8577	0.365 ^a	17.80	34.96731	1.49783
2	0.0871	0.368 ^b	18.01	34.98425	1.51626
3	0.0548	0.363 ^c	18.32	34.97850	1.50815
4	0.0004	0.372 ^c	18.94	34.98640	1.50205
5	0.0001	0.370 ^b	19.20	34.98922	1.50065

^aDESI DR1 (DESI Collaboration et al. 2025)

^bSDSS DR18 (Almeida et al. 2023)

^cDEIMOS (This work)

^dDESI Legacy Survey DR10 (Dey et al. 2019)

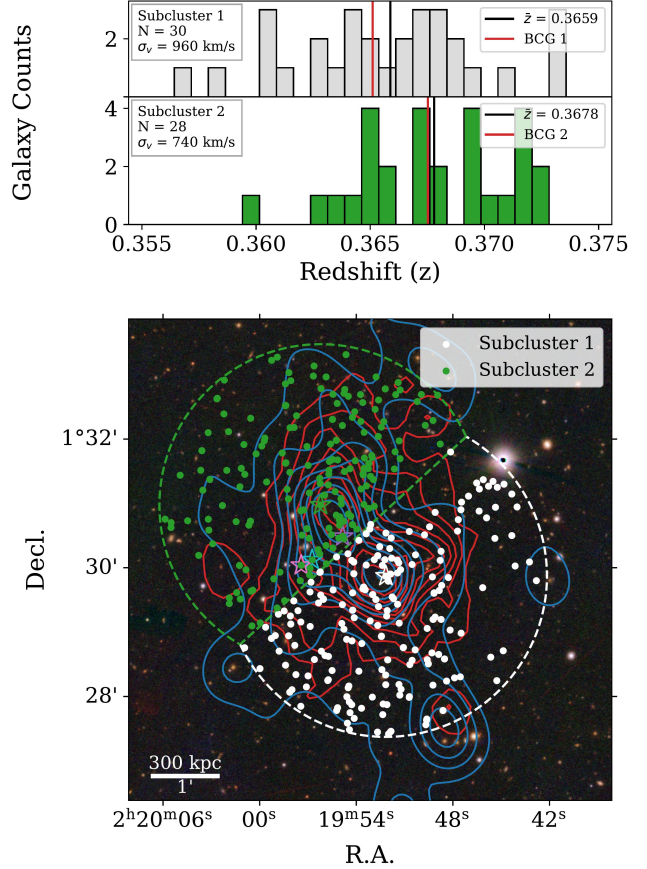


FIG. 13.— Subclustering analysis of RMJ0219. Bottom panel: spatial distribution of subcluster members, both spectroscopic and photometric, identified within regions defined by the bisector between BCG pairs and a radial distance of $2.5'$ from the BCG in each region. Top panel: redshift distribution of the spectroscopic members of those regions.

TABLE 15
RMJ0219 SUBCLUSTER PROPERTIES

Subcluster	N	BCG	BCG z	Mean z	σ_v [km s ⁻¹]
All	110	0.3674	980
1	30	1	0.365	0.3659	960
2	28	2	0.368	0.3678	740

The redshift distribution, shown in Figure 12, shows no foreground or background structures. The inset histogram shows two apparent peaks within the cluster redshift range of $0.355 \leq z \leq 0.375$, but this is likely a binning artifact and a single Gaussian fit is preferred. A one-component fit yields a lower BIC (-873 versus -867 for a two-component fit), and both KS ($D = 0.068$, $p = 0.63$) with AD ($A^2 = 0.63$, $p = 0.10$) statistics are consistent with a Gaussian distribution. In the bottom panel of the figure, no gradient in redshifts is evident.

Dividing the cluster into regions defined by the bisector between BCGs 1 and 2 and a $2.5'$ radius from each, shown in Figure 13, also shows no evidence for bimodality in redshift space. The redshift distributions of both subclusters are consistent with Gaussianity, with a line-

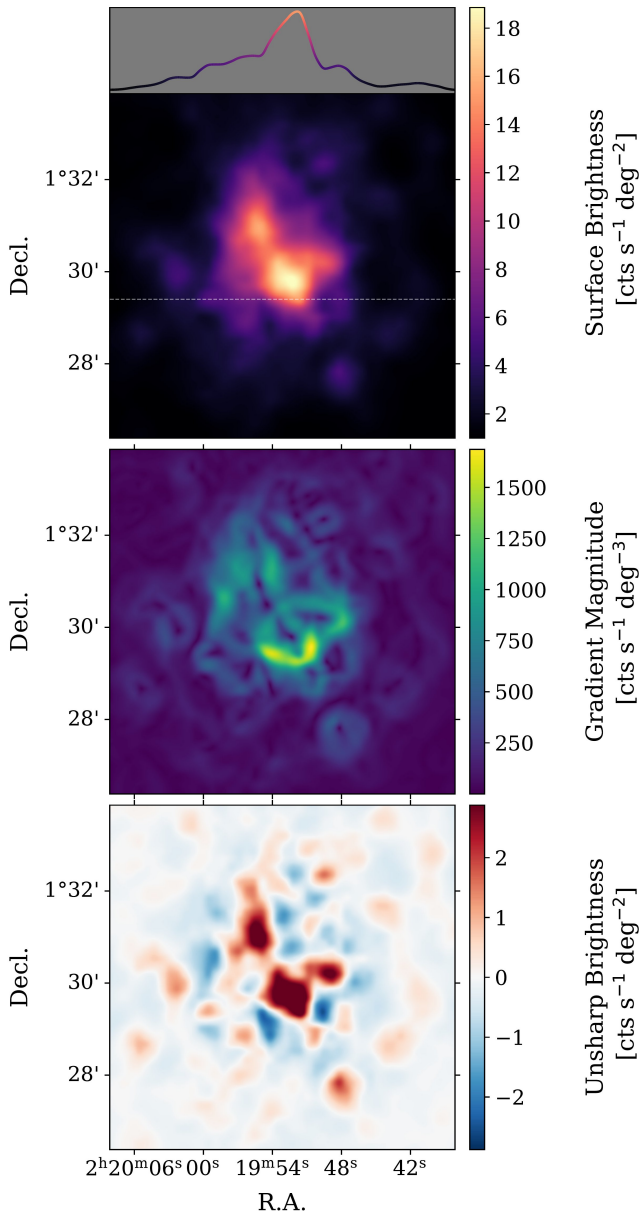


FIG. 14.— RMJ0219 X-ray features. Top panel: X-ray surface brightness smoothed with a $10''$ kernel and reprojected on an 800×800 pixel grid with the extracted 1D profile. The dashed line shows where the profile was extracted across the sharp feature. Center panel: gradient magnitude of the brightness. Bottom panel: residual features after unsharp masking, where an image smoothed with a kernel of $50''$ is subtracted from the image smoothed at $10''$.

of-sight offset of $\Delta V_{\text{LOS}} = 420 \text{ km s}^{-1}$ between subcluster means. Velocity dispersions for the two subclusters are similar at 960 and 740 km s^{-1} (Table 15). Overall, this system appears to be a clean, binary system near the plane of the sky.

Assuming BCG 2 to be the true BCG of the northern subcluster (with magnitude 18.01 versus 18.32 for BCG 3), the associated X-ray peak is lagging slightly ($\sim 100 \text{ kpc}$) to the south. The X-ray surface brightness also exhibits a steep gradient and bullet-like morphology in the southwest, near BCG 1. To explore this structure further, X-ray images were processed following the procedure in §2.2. A one-dimensional profile extracted across

the leading edge, shown in the top panel of Figure 14, reveals a sharp change in surface brightness on both the eastern and western edges of the cluster. This morphology is further highlighted with a map of the Gaussian gradient magnitude, shown in the center panel of Figure 14. An unsharp-masked image, shown in the bottom panel of Figure 14, was created by subtracting an image smoothed with a $50''$ kernel from one smoothed at $10''$, in which a bright edge tracing the leading boundary of the cluster is clearly visible.

From the X-ray morphology and galaxy distribution, this system appears to be a top candidate for a binary, post-pericenter, merger occurring near the plane of the sky. However, the X-ray temperature (4.50 keV) and luminosity ($1.93 \times 10^{44} \text{ erg s}^{-1}$) are not elevated, casting doubt on a recent pericenter passage. The sharp surface-brightness edge in the south is indicative of merger activity and is morphologically consistent with a cold-front-like structure, which could be confirmed with spatially resolved temperature measurements. While evidence supports a post-pericenter merger, a returning scenario, with the galaxies already having fallen back through the ICM, is not ruled out. Even given the uncertainty in the merger stage, the binary nature of this system still makes it a valuable target for future study. Follow-up with lensing and radio observations could be useful in determining the subcluster positions and constraining the merger stage.

3.3.4. RM J080135.3+362807.5

RedMaPPer lists the top two BCGs of RMJ0801 as having probabilities of 0.8964 and 0.1015 , with all others having a probability less than 0.002 . BCG 2 does not have a secure spectroscopic redshift, but it has been identified as a cluster member with a photometric redshift consistent with the cluster redshift (Szabo et al. 2011). We also identified an additional possible BCG, which we label BCG A, with magnitude 19.70 , placing it as the third brightest galaxy in the cluster (Table 16). We obtained a redshift of 0.503 with new DEIMOS spectroscopy, confirming it as a cluster member. BCG A also lies close to our fit of the cluster red sequence, with a difference of only 0.006 mag between the fit and actual $g-r$ color. Several bright foreground sources are visible in the optical image (Figure 15) possibly affecting the redMaPPer identification. However, unlike BCG B in RMJ0109,

TABLE 16
RMJ0801 BCG INFORMATION

BCG	Probability	Redshift	r -mag ^d	RA [deg]	Dec [deg]
1	0.8964	0.501 ^a	19.11	120.39710	36.46876
2	0.1015	...	19.23	120.37135	36.47645
3	0.0019	0.510 ^b	20.08	120.39008	36.47881
4	0.0001	0.500 ^b	20.12	120.36597	36.48641
5	0.0001	0.498 ^c	20.35	120.35158	36.48754
A	...	0.503 ^c	19.70	120.42687	36.45626

^aDESI DR1 (DESI Collaboration et al. 2025)

^bSDSS DR18 (Almeida et al. 2023)

^cDEIMOS (This work)

^dDESI Legacy Survey DR10 (Dey et al. 2019)

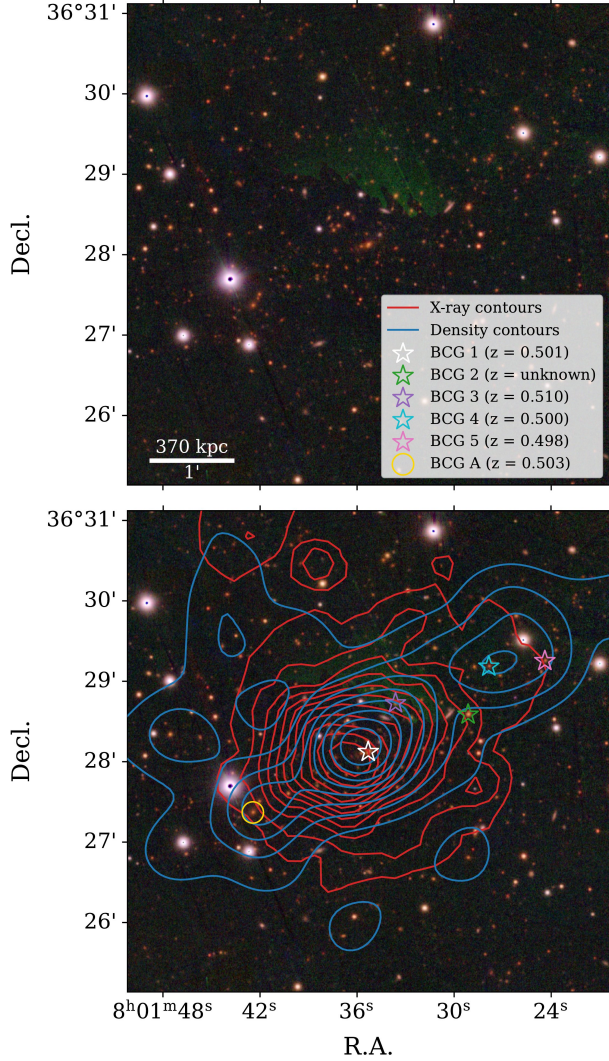


FIG. 15.— Optical image of RMJ0801. Top panel: 6' by 6' (2.22 by 2.22 Mpc) Pan-STARRS image. Bottom panel: red sequence density contours (blue), X-ray surface brightness contours (red), and BCG candidates identified by redMaPPer and this work.

there is no foreground galaxy directly obscuring BCG A.

Galaxy density contours suggest three possible subclusters, with the main cluster centered on BCG 1, a second with BCG A, and a third to the northwest with BCGs 4 and 5. BCG 2 does not appear to be associated with any underlying substructure. The luminosity density near BCG A is likely understated due to the bright stars, while the northwestern subcluster contours are largely dominated by BCGs 4 and 5.

The X-ray contours are elongated along a southeast-to-northwest axis, with a single peak southeast of BCG 1. While the X-ray peak is offset less than 100 kpc from the BCG, the displacement along the axis through BCGs 1 and A is indicative of a merger. Both temperature and luminosity are elevated given a richness of 125 (Table 6), at 8.65 keV and 4.51×10^{44} erg s $^{-1}$ (Table 8), with the temperature 1.6σ above the predicted value of 5.35 keV, providing further support for a merger scenario.

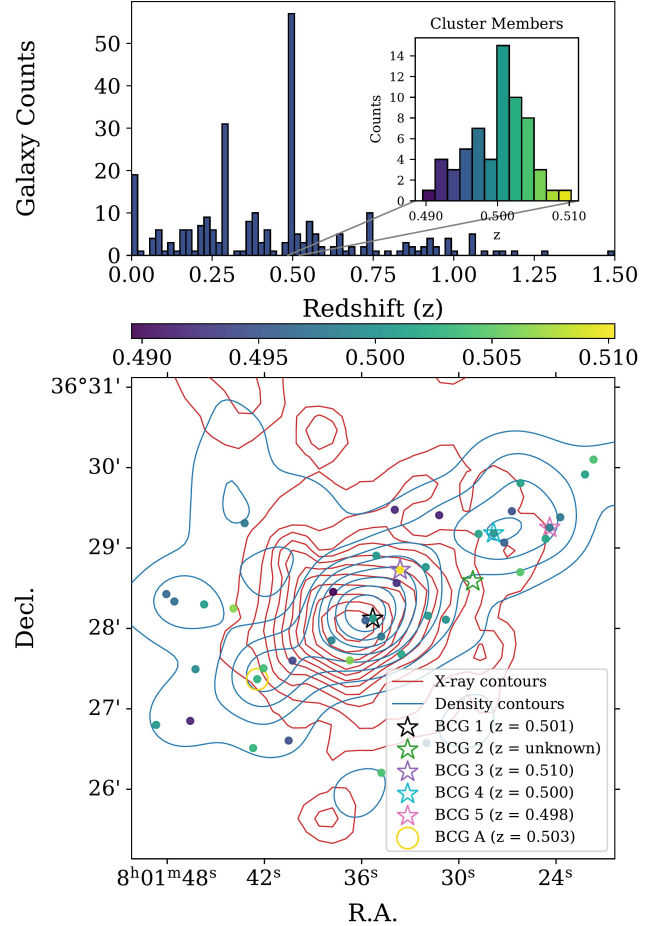


FIG. 16.— Redshift distribution of RMJ0801. Top panel: histogram of spectroscopic redshifts, combining archival data within 10' of the cluster with new observations from DEIMOS. The inset highlights galaxies in the redshift range $0.485 \leq z \leq 0.520$, which are classified as cluster members. Bottom panel: spatial distribution of those same members.

The redshift distribution, shown in Figure 16, shows two significant foreground structures, both identified as narrow components of the preferred GMM (five components total with three narrow). However, neither are in the immediate vicinity of the target cluster. The cluster at $z \sim 0.27$ is to the southwest out of the field of view shown. The ~ 20 galaxies at $z \lesssim 0.5$ are spread through the entire $10' \times 10'$ field. An additional smaller group at $z \sim 0.38$ is located due east of the cluster, also out of the field of view. The cluster redshift range was well fit by a single Gaussian and the spatial distribution shows no gradient or subclustering in redshift.

We divided the cluster into three regions around BCGs 1, 3, and A, shown in the left panel of Figure 17, and find no evidence of a LOS velocity difference between subclusters. The largest difference in LOS velocity is between Subclusters 1 and 3 at 220 km s^{-1} and all velocity dispersions lie in the range $850\text{--}980 \text{ km s}^{-1}$ (Table 17). While the central subcluster is dominant, it is not clear whether subclusters in the northwest and southeast are truly distinct so we consider scenarios that combine BCGs 1 and A (center panel) and BCGs 1 and 3 (right panel). In the first scenario, the resulting subclus-

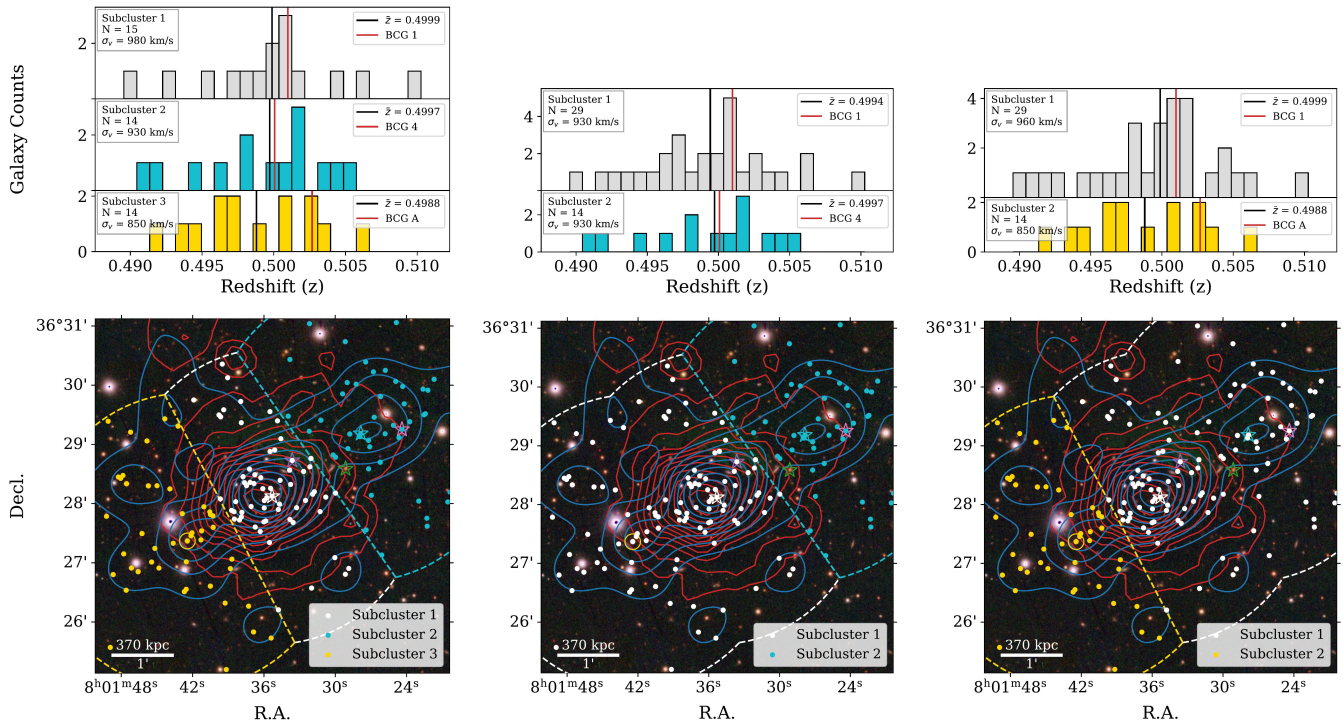


FIG. 17.— Subclustering analysis of RMJ0801. Bottom panels: spatial distribution of subcluster members, both spectroscopic and photometric, identified within regions defined by the bisector between BCG pairs and a radial distance of $2.5'$ from the BCG in each region. Top panels: redshift distribution of the spectroscopic members of those regions. The two right panels consider the subcluster associated with BCG A (center) and BCG 4 (right) to be part of Subcluster 1.

TABLE 17
RMJ0801 SUBCLUSTER PROPERTIES

Subcluster	N	BCG	BCG z	Mean z	σ_v [km s $^{-1}$]
All	62	0.5005	860
1	15	1	0.501	0.4999	980
2	14	4	0.500	0.4997	930
3	14	A	0.503	0.4988	850

ters have the same velocity dispersion at 930 km s $^{-1}$ and $\Delta V_{\text{LOS}} = 60$ km s $^{-1}$ between subcluster means. The second scenario tells much the same story with Subcluster 1 velocity dispersion dropping to $\sigma_v = 960$ km s $^{-1}$, and a 220 km s $^{-1}$ LOS velocity difference between subclusters.

Given the X-ray peak displaced toward BCG A along with the elevated temperature and luminosity, it seems likely that this is a recent merger between subclusters at BCGs 1 and A. The role of the northwestern group is more uncertain, but is likely a small infalling group. With a morphology that can likely be well-modeled as a binary merger, we believe this is an excellent candidate for follow-up observations. Given the abundance of foreground sources contaminating the density contours, weak lensing would be particularly useful in determining the extent of the secondary subclusters.

3.3.5. RM J082944.9+382754.0

RMJ0829 is a complicated system, with redMaPPer identifying BCGs 1, 2, and 3 all having $> 10\%$ probability of being the true BCG (Table 18). However, we confirmed BCG 2 to be at $z = 0.342$ while the other BCGs are spectroscopically confirmed at $z \sim 0.39$, cor-

responding to a difference in BCG line-of-sight velocities of $\sim 10,000$ km s $^{-1}$. We believe this to be part of a foreground system west of the target cluster (Figure 18), with our target being located at $0.38 \leq z \leq 0.41$. BCG 5 is the brightest in the cluster, with r -band magnitude of 18.29 as compared to 18.42 for BCG 1.

The X-ray contours are elongated both along an axis between BCG 1 and BCG 3/4 and to the southwest and BCG 5, with a sharp peak ≈ 100 kpc northwest of BCG 1. This sharp peak is nearly coincident with BCG 1 but is not located between any pair of BCGs. We considered the possibility that a point source was embedded in the extended cluster emission and missed by the ESAS cheese routine. To rule out this possibility, we manu-

TABLE 18
RMJ0829 BCG INFORMATION

BCG	Probability	Redshift	r -mag ^d	RA [deg]	Dec [deg]
1	0.6412	0.392 ^a	18.42	127.43722	38.46511
2	0.1930	0.342 ^b	19.18	127.40229	38.46144
3	0.1021	0.397 ^b	19.54	127.46242	38.46859
4	0.0359	0.395 ^b	19.34	127.46410	38.47002
5	0.0278	0.391 ^c	18.29	127.40543	38.43779

^aSDSS DR18 (Almeida et al. 2023)

^bDEIMOS (This work)

^cDESI DR1 (DESI Collaboration et al. 2025)

^dDESI Legacy Survey DR10 (Dey et al. 2019)

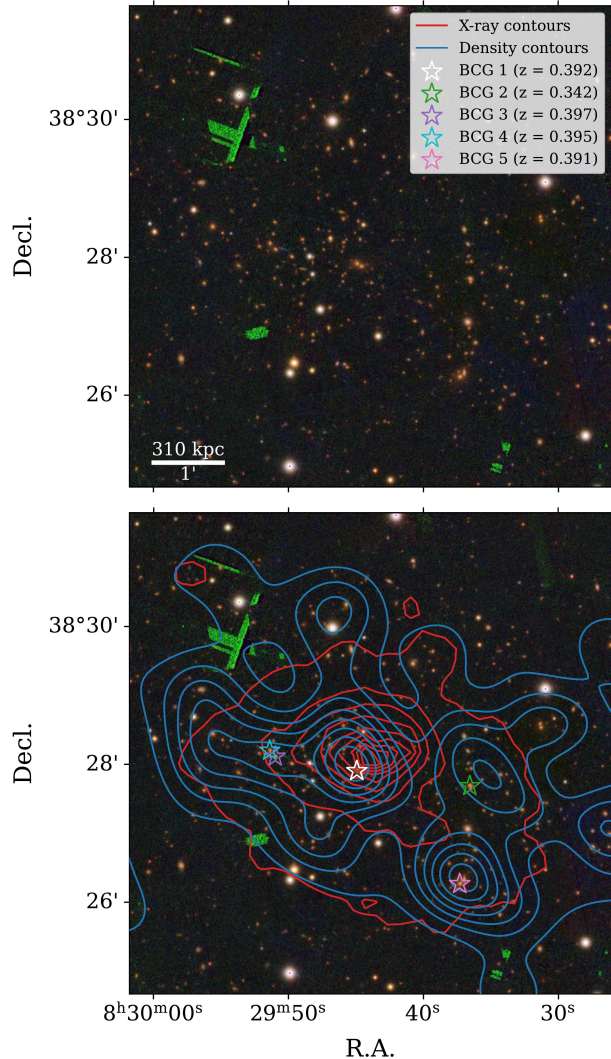


FIG. 18.— Optical image of RMJ0829. Top panel: $7'$ by $7'$ (2.17 by 2.17 Mpc) Pan-STARRS image. Bottom panel: red sequence density contours (blue), X-ray surface brightness contours (red), and BCG candidates identified by redMaPPer.

ally extracted high-energy events in a 2.5 – 7.5 keV band using `evselect` and found no events corresponding to the bright emission. Luminosity density contours show a complex morphology, with two distinct overdensities at BCGs 1 and 5 and an extended tail towards BCGs 3 and 4. However, the extended structure to the northeast is greatly reduced in unweighted number density and is unlikely to represent any significant substructure.

The redshift distribution, shown in Figure 19, is best-fit with a single component in the cluster region with both KS ($D = 0.060$, $p = 0.76$) and AD ($A^2 = 0.41$, $p = 0.36$) tests consistent with a normal distribution. For the entire range of $z \leq 1.5$, a three-component fit is preferred with a single narrow component at the cluster redshift. Spatially, the highest redshift members of the cluster are all contained between BCG 1 and 2, indicating a possible localized line-of-sight velocity contribution. Dividing the cluster into regions defined by bisectors between BCGs 1 and 5 and a radius of $2.5'$ from each BCG

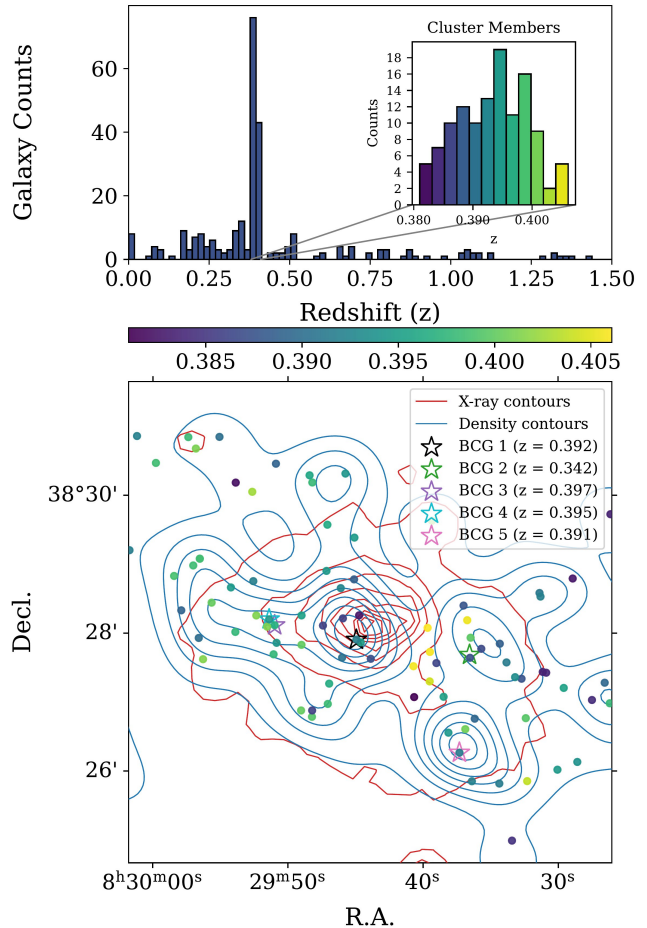


FIG. 19.— Redshift distribution of RMJ0829. Top panel: histogram of spectroscopic redshifts, combining archival data within $10'$ of the cluster with new observations from DEIMOS. The inset highlights galaxies in the redshift range $0.38 \leq z \leq 0.41$, which are classified as cluster members. Bottom panel: spatial distribution of those same members.

(Figure 20) shows a slight bias towards higher redshift for Subcluster 1 and a velocity difference of 950 km s^{-1} between subcluster means (Table 19).

Temperature (6.95 keV) and X-ray luminosity ($5.50 \times 10^{44} \text{ erg s}^{-1}$) are both elevated $>1\sigma$ above expected values (Table 8). Additionally, RMJ0829 (PSZ2 G183.30+34.98) has been identified as hosting a candidate radio halo by Botteon et al. (2022). The halo is reported as a newly claimed detection and is accompanied by diffuse radio emission of unknown origin elongated in the north-south direction to the east of the cluster center. The combination of disturbed X-ray morphology and diffuse radio emission strongly suggest a dynamically active system. The optical and X-ray data are broadly consistent with a merger between subclusters associated with BCGs 1 and 5, although the location of the X-ray peak likely disfavors a simple head-on configuration. We believe this to be a binary system with a non-zero impact parameter, but are unable to definitively rule out contributions from substructure in the northeast. Weak-lensing constraints on the mass distribution would be valuable in clarifying the merger geometry and assessing whether the system can be modeled reliably as a two-

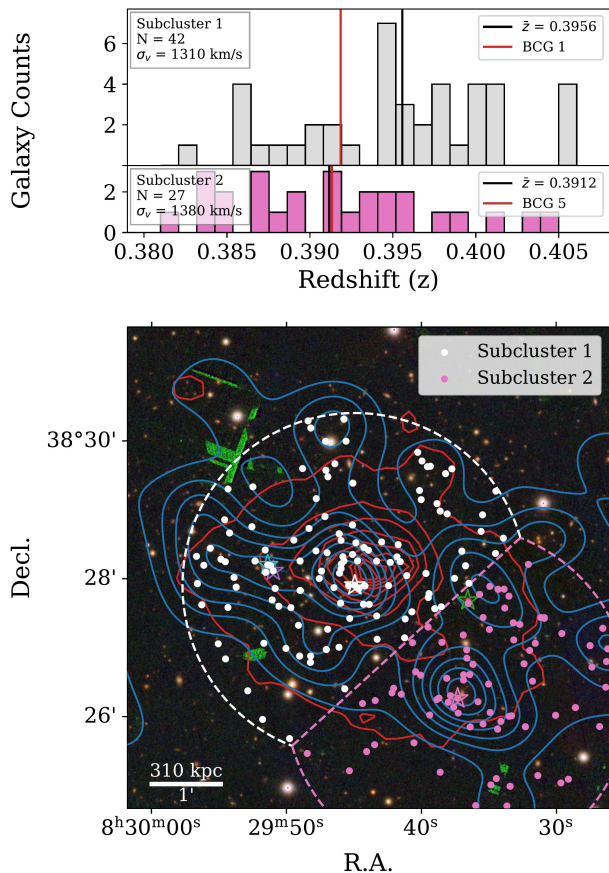


FIG. 20.— Subclustering analysis of RMJ0829. Bottom panel: spatial distribution of subcluster members, both spectroscopic and photometric, identified within regions defined by the bisector between BCG pairs and a radial distance of $2.5'$ from the BCG in each region. Top panel: redshift distribution of the spectroscopic members of those regions.

TABLE 19
RMJ0829 SUBCLUSTER PROPERTIES

Subcluster	N	BCG	BCG z	Mean z	σ_v [km s $^{-1}$]
All	119	0.3934	1330
1	42	1	0.392	0.3956	1310
2	27	5	0.391	0.3912	1380

body interaction.

3.3.6. *RM J092647.3+050004.0*

In contrast with RMJ0829, RMJ0926 appears to be a relatively simple system. The highest probability BCG in redMaPPer is at 0.7821 for BCG 1, while all other BCGs have roughly the same probability of ~ 0.05 (Table 20). We were unable to get a confirmed redshift on BCG 4, but it was selected through a fit of the red sequence, and we believe it to be a cluster member. The X-ray surface brightness (Figure 21) has a single peak at BCG 4 and is elongated along a north-south axis, coinciding with an axis that runs through all but BCG 2. The single peak located with BCG 4 may suggest a relaxed cluster at that location. However, BCG 4 is the faintest of the BCG candidates with an r -band magni-

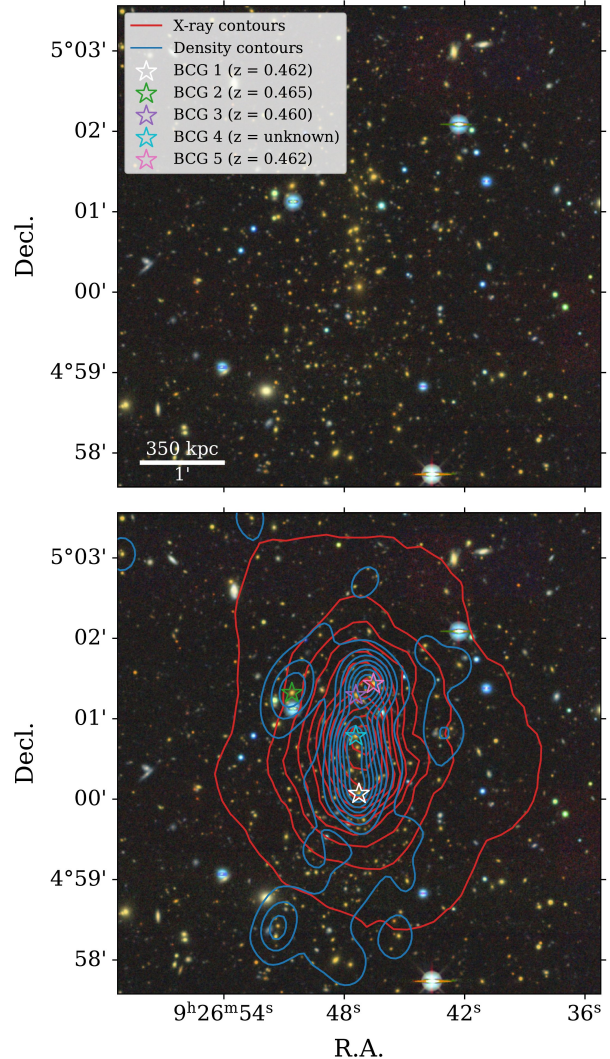


FIG. 21.— Optical image of RMJ0926. Top panel: $6'$ by $6'$ (2.10 by 2.10 Mpc) Legacy Survey image. Bottom panel: red sequence density contours (blue), X-ray surface brightness contours (red), and BCG candidates identified by redMaPPer.

TABLE 20
RMJ0926 BCG INFORMATION

BCG	Probability	Redshift	r -mag ^d	RA [deg]	Dec [deg]
1	0.7821	0.462 ^a	18.65	141.69696	5.00110
2	0.0746	0.465 ^b	19.14	141.71086	5.02208
3	0.0511	0.460 ^c	19.30	141.69759	5.02156
4	0.0479	...	19.47	141.69760	5.01306
5	0.0444	0.462 ^b	18.88	141.69397	5.02389

^aSDSS DR18 (Almeida et al. 2023)

^bDEIMOS (This work)

^cDESI DR1 (DESI Collaboration et al. 2025)

^dDESI Legacy Survey DR10 (Dey et al. 2019)

tude of 19.47 and is unlikely to be the single BCG of a relaxed system. The galaxy luminosity density has two

primary peaks, one encompassing BCGs 1 and 4 and another with BCGs 3 and 5. The contours are elongated along the same axis as the X-ray surface brightness, but also extend to the east and enclose BCG 2. The galaxy density at BCG 2 is likely underreported due to contamination from point sources, but it does not appear to be a separate subcluster.

Two foreground structures were identified in a GMM fit of the redshift distribution (Figure 22) both with ~ 45 members. The first, at $z = 0.25$, is widely scattered through the eastern half of the full field of view, with only ~ 5 members in the cluster region. The second, at $z = 0.36$, is largely concentrated to the southeast of the cluster, but has ~ 10 members overlapping along the cluster's eastern edge. That group could contribute some to the widening of the X-ray surface brightness south of BCG 2, but does not affect the general observed morphology. In the cluster region, $0.445 \leq z \leq 0.475$, a single-component GMM fit is preferred and consistent with Gaussianity ($D = 0.060$, $p = 0.88$; $A^2 = 0.33$, $p = 0.51$). The spatial distribution of redshifts, shown in the bottom panel of Figure 22, shows some clustering of lower redshift members near BCG 1, which could indicate

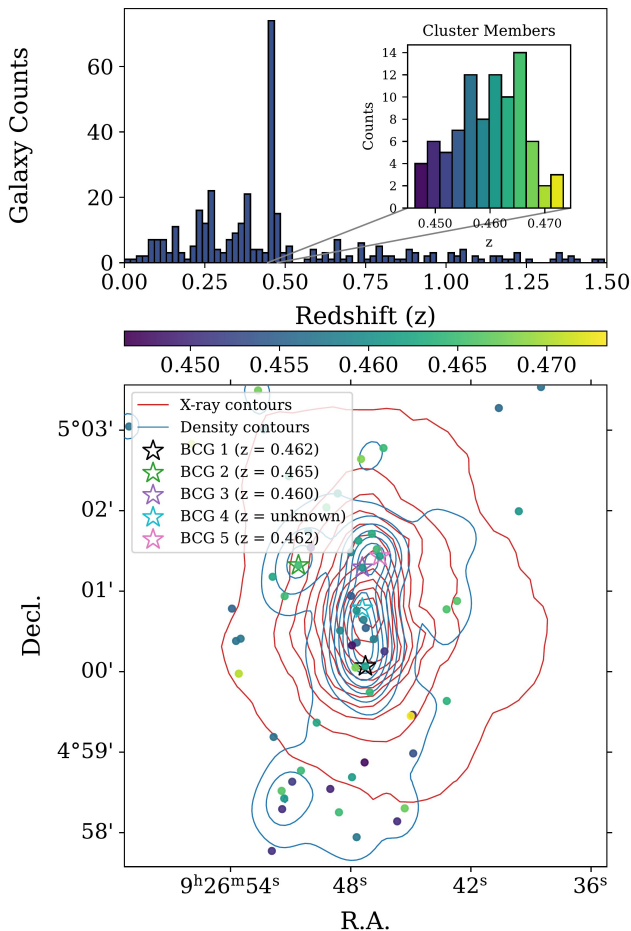


FIG. 22.— Redshift distribution of RMJ0926. Top panel: histogram of spectroscopic redshifts, combining archival data within $10'$ of the cluster with new observations from DEIMOS. The inset highlights galaxies in the redshift range $0.445 \leq z \leq 0.475$, which are classified as cluster members. Bottom panel: spatial distribution of those same members.

TABLE 21
RMJ0926 SUBCLUSTER PROPERTIES

Subcluster	N	BCG	BCG z	Mean z	σ_v [km s^{-1}]
All	89	0.4600	1358
1	37	1	0.462	0.4588	1410
2	17	3	0.460	0.4624	670

a local LOS velocity component. Dividing the field into northern and southern subclusters centered on BCGs 1 and 3 (Figure 23) shows the northern (southern) subcluster with a velocity dispersion of 670 km s^{-1} (1410 km s^{-1}) (Table 21) and a velocity difference of 740 km s^{-1} between subcluster means.

RMJ0926 has the highest temperature of any cluster in the sample at 10.55 keV , which is 2.7σ above the expected value of 5.65 keV . The X-ray luminosity is similarly elevated at $6.84 \times 10^{44} \text{ erg s}^{-1}$ (Table 8), compared to the expected value of $2.35 \times 10^{44} \text{ erg s}^{-1}$ for a cluster of richness 140 (Table 6), corresponding to a 1.8σ excess. This, along with a separation between northern and southern subclusters in both galaxy density and redshift distribution, supports a binary merger scenario. Subclus-

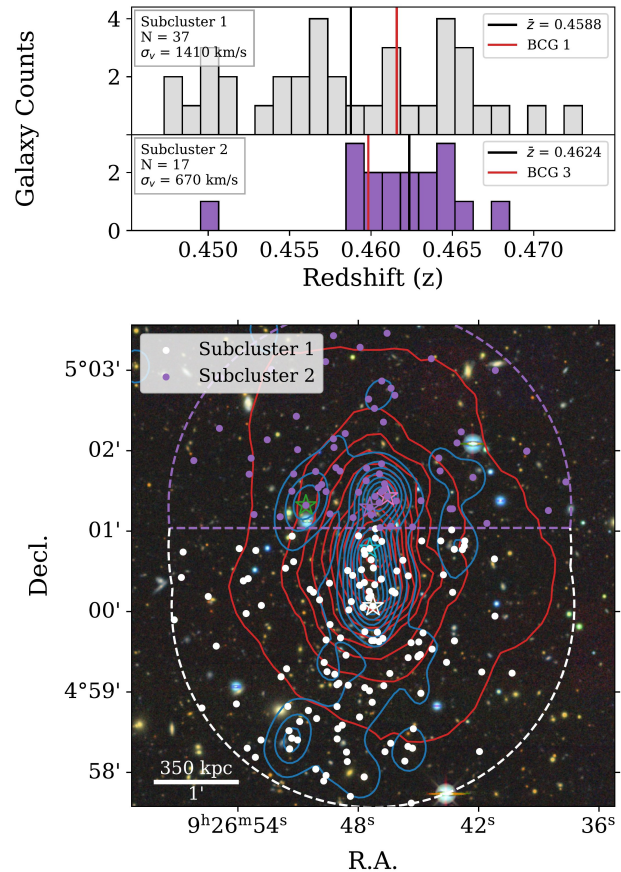


FIG. 23.— Subclustering analysis of RMJ0926. Bottom panel: spatial distribution of subcluster members, both spectroscopic and photometric, identified within regions defined by the bisector between BCG pairs and a radial distance of $2.5'$ from the BCG in each region. Top panel: redshift distribution of the spectroscopic members of those regions.

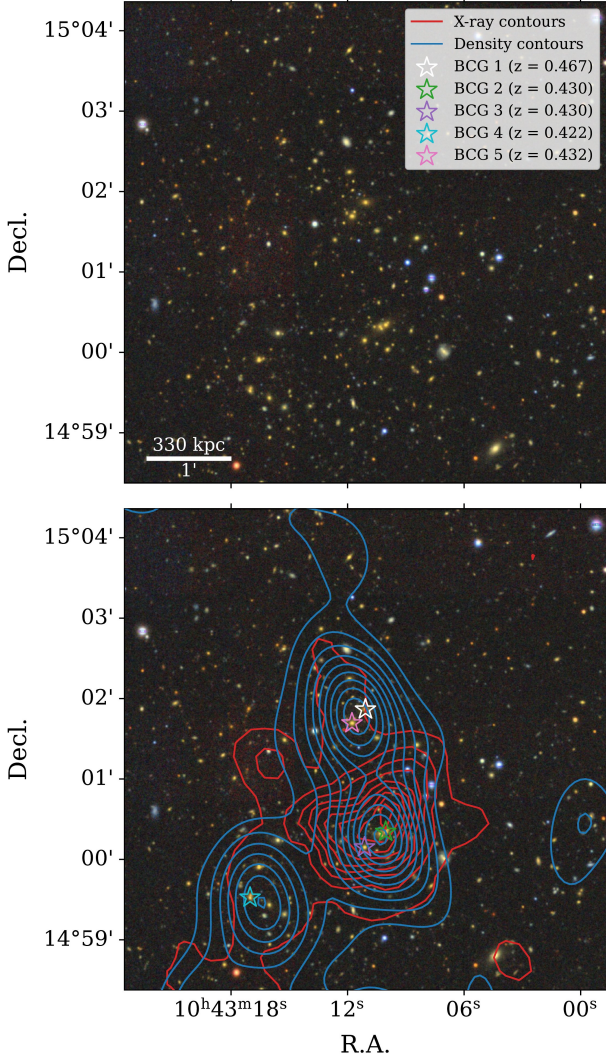


FIG. 24.— Optical image of RMJ1043. Top panel: 6' by 6' (1.98 by 1.98 Mpc) Legacy Survey image. Bottom panel: red sequence density contours (blue), X-ray surface brightness contours (red), and BCG candidates identified by redMaPPer.

ters at BCG 1 and BCG 3/5 are separated by ≈ 480 kpc, with the X-ray peak directly between the subclusters, ≈ 240 kpc from each. This is one of the cleanest binary merger candidates in the sample and a top-priority for follow-up, particularly with weak lensing.

3.3.7. RM J104311.1+150151.9

RMJ1043 is another complicated system, with all BCGs having a redMaPPer probability > 0.10 (Table 22). BCG 1, with probability 0.3327, is at a higher redshift than the rest of the BCGs at $z = 0.467$ versus $z \sim 0.43$, representing a velocity difference of > 7500 km s^{-1} . Galaxy density contours show three distinct peaks localized on BCG 1/5, BCG 2/3, and BCG 4 (Figure 24). The X-ray surface brightness is primarily localized around BCGs 2 and 3, with a peak north of BCG 2. The bulk of the X-ray emission is also extended to the east, roughly between all three galaxy density peaks.

In the range of $0.42 \leq z \leq 0.48$, the redshift dis-

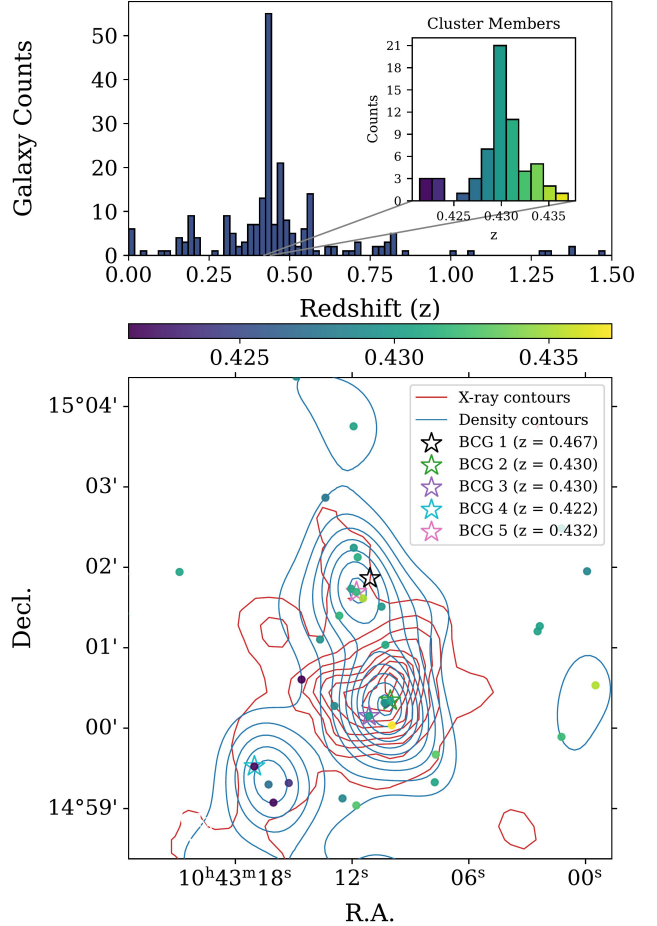


FIG. 25.— Redshift distribution of RMJ1043. Top panel: histogram of spectroscopic redshifts, combining archival data within $10'$ of the cluster with new observations from DEIMOS. The inset highlights galaxies in the redshift range $0.42 \leq z \leq 0.44$, which are classified as cluster members. Bottom panel: spatial distribution of those same members.

tribution (Figure 25) is best-fit with a two-component GMM. The primary peak, with 56 members at $z = 0.43$, encompasses BCGs 2–5 while BCG 1 is located with a secondary peak containing 27 members at $z = 0.47$. Given the difference in redshift (~ 7500 km s^{-1} between BCGs 1 and 2), we consider the cluster redshift to be $0.42 \leq z \leq 0.44$, and the cluster associated with BCG 1

TABLE 22
RMJ1043 BCG INFORMATION

BCG	Probability	Redshift	r -mag ^c	RA [deg]	Dec [deg]
1	0.3327	0.467 ^a	19.08	160.79619	15.03108
2	0.2613	0.430 ^b	18.66	160.79184	15.00572
3	0.1514	0.430 ^a	19.68	160.79639	15.00251
4	0.1506	0.422 ^a	19.31	160.82095	14.99200
5	0.1041	0.432 ^b	19.05	160.79907	15.02822

^aDEIMOS (This work)

^bSDSS DR18 (Almeida et al. 2023)

^cDESI Legacy Survey DR10 (Dey et al. 2019)

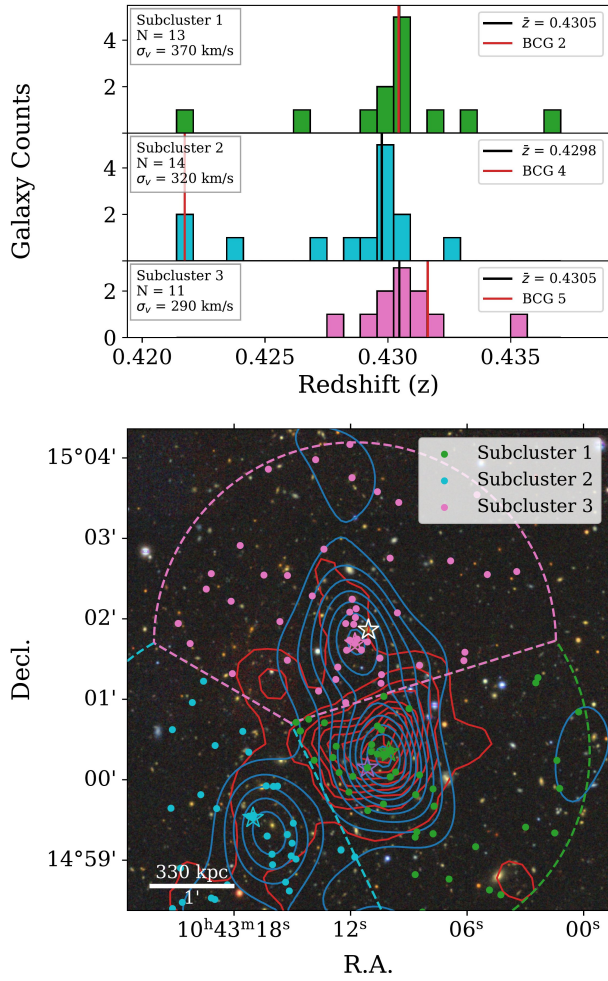


FIG. 26.— Subclustering analysis of RMJ1043. Bottom panel: spatial distribution of subcluster members, both spectroscopic and photometric, identified within regions defined by the bisector between BCG pairs and a radial distance of $2.5'$ from the BCG in each region. Top panel: redshift distribution of the spectroscopic members of those regions.

to be in the background. Both luminosity-weighted and unweighted density contours of spectroscopic members show this background group has two primary concentrations, one just north of BCG 1 and the other near BCG 4. Neither of these regions overlap with the observed X-ray emission, and contributions to the cluster luminosity density are minimal. Within the cluster redshift range, the redshift distribution is consistent with a normal distribution by both KS ($D = 0.21$, $p = 0.85$) and AD ($A^2 = 0.37$, $p = 0.34$) tests. A GMM fit across the entire redshift range of $z \leq 1.5$ identifies an additional background group with 20 members at $z = 0.56$. This group is again divided into two primary concentrations, with one north of the cluster and one south, neither of which contaminate the observed X-rays.

Dividing the cluster into three regions centered on BCGs 2, 4, and 5 (Figure 26) shows all three groups with small velocity dispersions ($\leq 370 \text{ km s}^{-1}$) and $< 150 \text{ km s}^{-1}$ velocity difference between subcluster means (Table 23), suggesting minimal interaction along

TABLE 23
RMJ1043 SUBCLUSTER PROPERTIES

Subcluster	N	BCG	BCG z	Mean z	σ_v [km s^{-1}]
All	61	0.4302	470
1	13	2	0.430	0.4305	370
2	14	4	0.422	0.4298	320
3	11	5	0.432	0.4305	290

the line of sight. However, the picture is complicated by a small handful of galaxies in Subcluster 2, including BCG 4, which are at a lower redshift than the primary distribution (a velocity difference of 1600 km s^{-1} between BCG 4 and the subcluster mean). We can see in the bottom panel of Figure 25 that the lowest redshift members of the cluster are exclusively concentrated near BCG 4. If the cluster redshift range is defined $0.425 \leq z \leq 0.44$, removing the four low-redshift galaxies from the luminosity density eliminates the peak seen in the southeast.

Given the disturbed X-ray morphology and peak offset, we believe this to be a merger, likely binary between Subclusters 1 and 3 with Subcluster 3 being stripped of its gas. Subcluster 2 could also be involved, and further spectroscopy would help in determining if there is a unique group at a lower redshift associated with BCG 4. Of the 12 clusters studied, RMJ1043 has the lowest richness, X-ray temperature, and X-ray luminosity at 121 (Table 6), 2.77 keV, and $0.56 \times 10^{44} \text{ erg s}^{-1}$ (Table 8), respectively. Both temperature and luminosity lie 2σ below expected values. Such low T_X and L_X disfavor the low impact parameter suggested by the gas-stripping of Subcluster 2. However, in addition to the lowest λ , T_X , and L_X in our sample, RMJ1043 also has the lowest velocity dispersion at 470 km s^{-1} (Table 23, indicating a less massive system than the richness would suggest).

RedMaPPer computes richness by first assigning galaxies a probability of being a cluster member based on a fit of the red sequence. The richness is then defined as a sum over those probabilities, weighted by radius and luminosity-dependent factors. The radius-weighting selects for members using a “soft” cut which penalizes galaxies outside of a richness-dependent scale radius of $\sim 1 \text{ Mpc}$. With BCG 1 having a probability of only 0.3327, again, the lowest in the sample, it is possible that the redMaPPer richness was influenced by an ambiguity in cluster location as well as interlopers near Subclusters 1 and 3. A lower richness would help to explain the discrepancy in T_X and L_X , as well as the low velocity dispersion.

This is a complicated system that would benefit from further spectroscopy to untangle any structure along the line-of-sight. While it is likely to be a binary dissociative merger, these interlopers could prove prohibitive to building accurate mass models with weak lensing.

3.3.8. RM J121917.6+505432.8

RMJ1219 has archival *Chandra* data (Observation Id. 21715, P.I. Kraft) and LOFAR analysis (van Weeren et al. 2021; Botteon et al. 2022), which were combined with this work as well as weak lensing from HST by Stancioli et al. (2026, in preparation) in a comprehensive analysis. All five BCGs identified by redMaPPer (four with a probability of > 0.10) (Table 24) are located east of the cluster, making this largely a serendipitous discov-

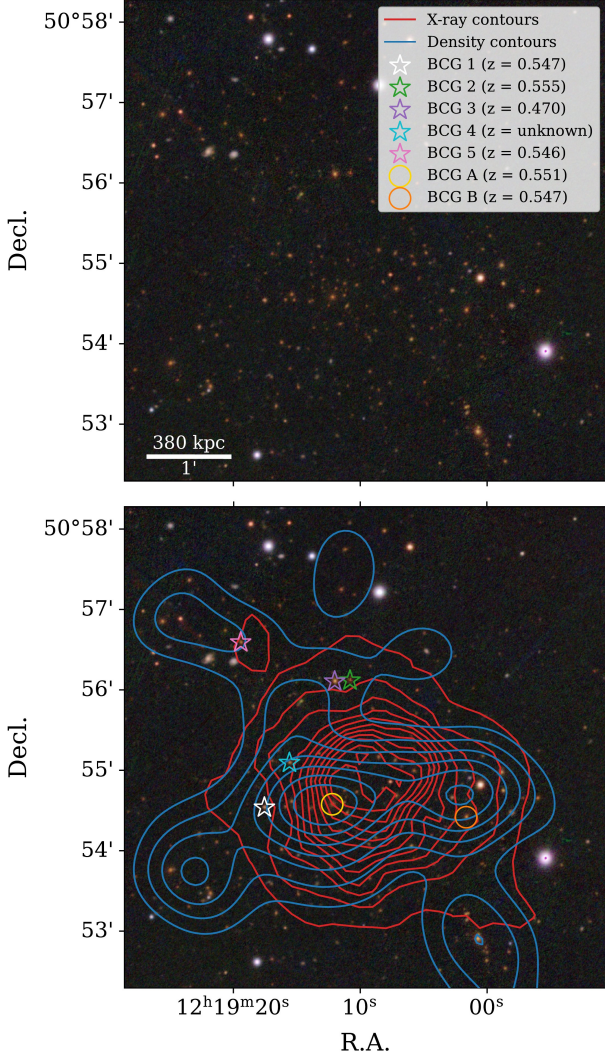


FIG. 27.— Optical image of RMJ1219. Top panel: 6' by 6' (2.28 by 2.28 Mpc) Pan-STARRS image. Bottom panel: red sequence density contours (blue), X-ray surface brightness contours (red), and BCG candidates identified by redMaPPer.

TABLE 24
RMJ1219 BCG INFORMATION

BCG	Probability	Redshift	r -mag ^c	RA [deg]	Dec [deg]
1	0.5124	0.547 ^a	20.07	184.82321	50.90911
2	0.2050	0.555 ^b	20.56	184.79510	50.93541
3	0.1742	0.470 ^b	18.80	184.80006	50.93522
4	0.1032	...	20.37	184.81497	50.91838
5	0.0052	0.546 ^b	20.14	184.83102	50.94331
A	...	0.551 ^a	19.49	184.80083	50.90971
B	...	0.547 ^a	19.88	184.75687	50.90707

^aDEIMOS (This work)

^bSDSS DR18 (Almeida et al. 2023)

^cDESI Legacy Survey DR10 (Dey et al. 2019)

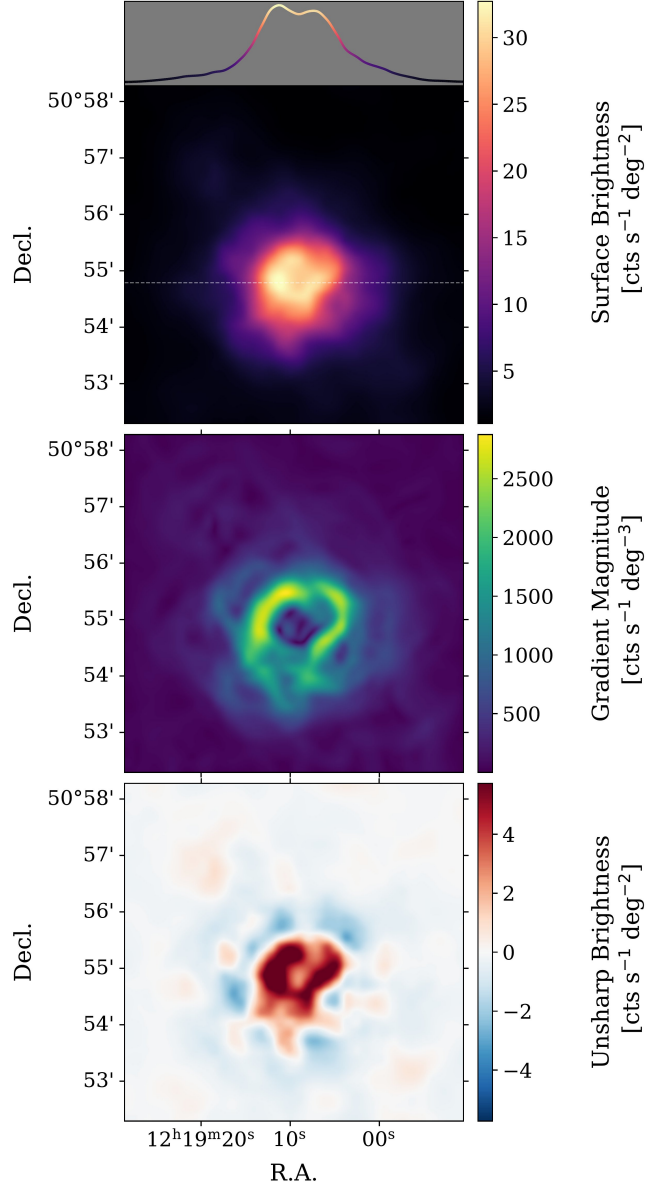


FIG. 28.— RMJ1219 X-ray features. Top panels: X-ray surface brightness smoothed with a 10'' kernel and reprojected on an 800 × 800 pixel grid with the extracted 1D profile. The dashed line shows where the profile was extracted. Center panel: gradient magnitude of the brightness. Bottom panel: residual features after unsharp masking, where an image smoothed with a kernel of 50'' is subtracted from the image smoothed at 10''.

ery. The brightest of these, BCG 3, is at a significantly lower redshift than the cluster (0.47 versus ~ 0.55 for the cluster). BCG 4 does not have a confirmed spectroscopic redshift and was not selected as cluster member in our fit of the red sequence. The true BCGs, labeled A and B, have r -band magnitudes of 19.49 and 19.88, respectively, and are each associated with one of the two overdensities of galaxies, shown in Figure 27, in the east and the west.

The X-ray surface brightness is strongly disturbed, with a crescent-shaped central structure between the two optical subclusters. This peak is roughly bimodal, as seen in the one-dimensional profile extracted across the cluster's center (top panel of Figure 28), where two local maxima are resolved within the broader emission enve-

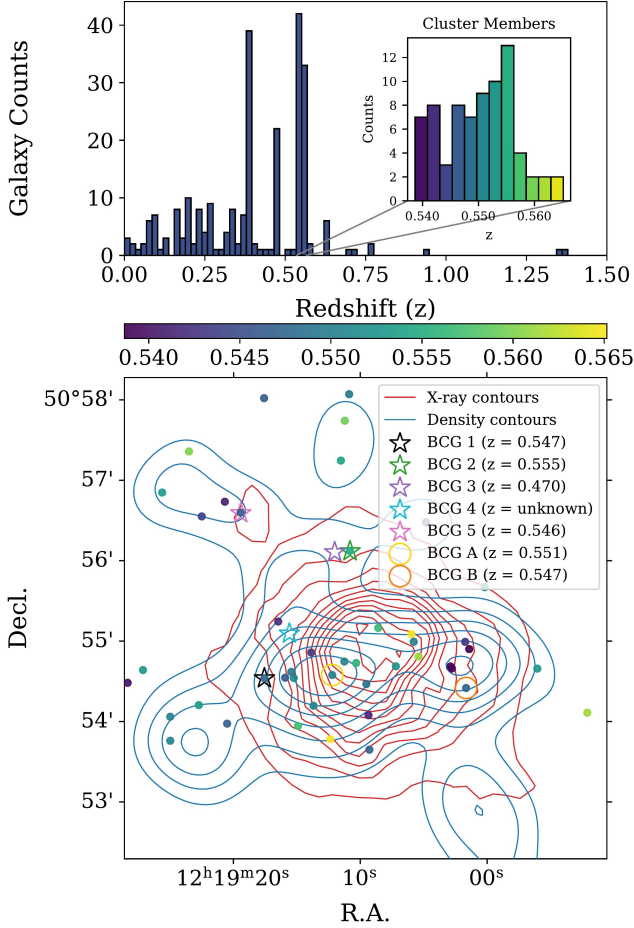


FIG. 29.— Redshift distribution of RMJ1219. Top panel: histogram of spectroscopic redshifts, combining archival data within $10'$ of the cluster with new observations from DEIMOS. The inset highlights galaxies in the redshift range $0.535 \leq z \leq 0.566$, which are classified as cluster members. Bottom panel: spatial distribution of those same members.

lope. The gradient map (center panel) highlights sharp brightness discontinuities along the eastern and western edges of the emission. These features are further emphasized in the unsharp-mask image (bottom panel). Both the location and morphology of the X-ray emission provide strong evidence of a dissociative merger.

The redshift histogram, shown in the top panel of Figure 29, exhibits two large foreground structures, both confirmed with a GMM fit. The spatial distribution of these structures is given in Figure 30, with luminosity-weighted density contours created from spectroscopic members with `scipy.stats.gaussian_kde` using a kernel factor of 0.2. The first, with 55 spectroscopic members at $0.378 \leq z \leq 0.40$, is concentrated southwest of the majority of the X-ray emission, 1.2 Mpc south-

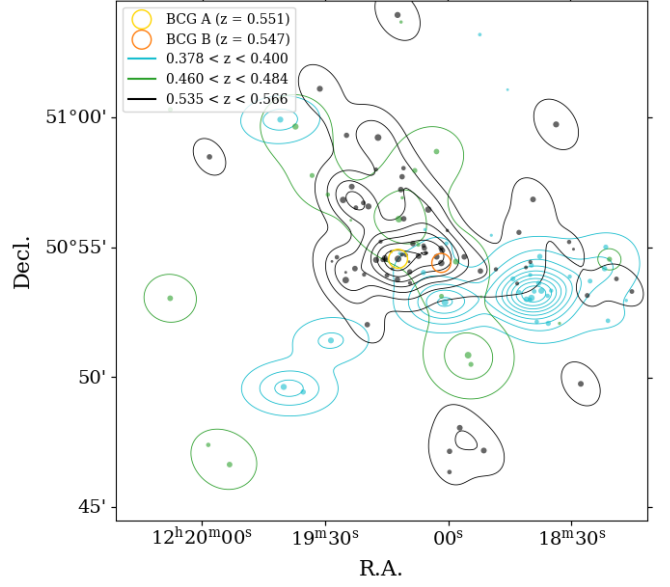


FIG. 30.— Distribution of foreground clusters in the full $10'$ field of RMJ1219. Contours show the luminosity-weighted density of spectroscopic members in each redshift bin. Individual galaxies are indicated by markers sized proportional to their luminosity.

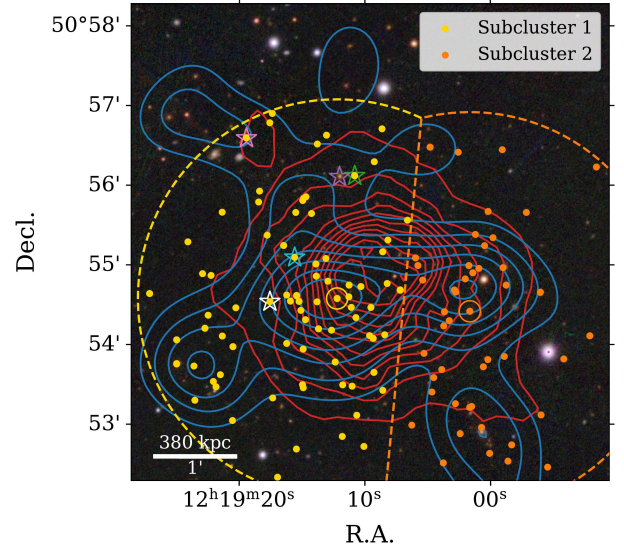
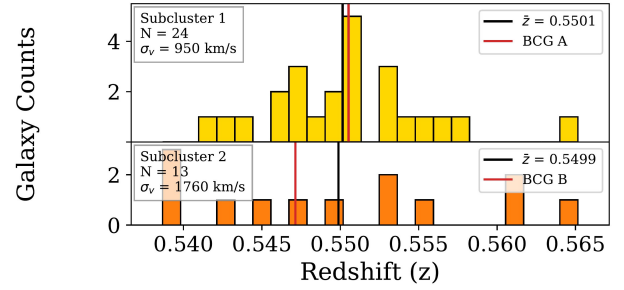


FIG. 31.— Subclustering analysis of RMJ1219. Bottom panel: spatial distribution of subcluster members, both spectroscopic and photometric, identified within regions defined by the bisector between BCG pairs and a radial distance of $2.5'$ from the BCG in each region. Top panel: redshift distribution of the spectroscopic members of those regions.

TABLE 25
RMJ1219 SUBCLUSTER PROPERTIES

Subcluster	N	BCG	BCG z	Mean z	σ_v [km s^{-1}]
All	75	0.5503	1290
1	24	A	0.551	0.5501	950
2	13	B	0.547	0.5499	1760

west of BCG B. The observed X-ray and luminosity density are not affected by this cluster, but analysis further from the cluster center could be impacted. The second, with 23 members at $0.46 \leq z \leq 0.484$, is distributed broadly across the cluster region. This cluster could produce some foreground contamination, particularly in the galaxy density where the luminosity peaks in the southwest and northeast are likely artifacts of interlopers in the fit of the CMD. However, with only 22 spectroscopic members across such a broad region, the location of the X-ray surface brightness peak is likely not materially affected.

Within the cluster redshift range, $0.535 \leq z \leq 0.566$, there appears to be an excess of galaxies at the low end of the redshift distribution. However, a one-component fit is preferred and consistent with a Gaussian distribution ($D = 0.078$, $p = 0.73$; $A^2 = 0.59$, $p = 0.12$). The spatial distribution of redshifts within the cluster region (Figure 29) shows some grouping of low redshift members near BCG B. We divide the cluster into regions defined by the bisector between BCGs A and B and a $2.5'$ radius from each (Figure 31). Subcluster 1 has a velocity dispersion of 950 km s^{-1} while Subcluster 2 is more widely distributed across the full redshift range with a dispersion of 1760 km s^{-1} (falsely elevated due to the low-number statistics)(Table 25). Both are at nearly the same redshift with a LOS velocity difference of only 40 km s^{-1} , indicating a merger near the plane of the sky.

Given a richness of 165 (Table 6), the X-ray temperature and luminosity of 7.27 keV and $5.32 \times 10^{44} \text{ erg s}^{-1}$ (Table 8) are both slightly elevated from expected scaling relations. Weak lensing results from Stancioli et al. (2026, in preparation) confirm a dissociative merger between east and west subclusters. Consistent with this interpretation, LOFAR observations indicate the presence of both a radio relic and radio halo (van Weeren et al. 2021; Botteon et al. 2022). However, the eastern subcluster is not well fit by a single spherical NFW profile, indicating a possible separate recent merging event. Overall, this is an interesting system with clear evidence of merging activity and a great candidate for additional study.

TABLE 26
RMJ1257 BCG INFORMATION

BCG	Probability	Redshift	r -mag ^d	RA [deg]	Dec [deg]
1	0.9473	0.518 ^a	19.13	194.35800	36.90816
2	0.0367	0.527 ^b	19.81	194.36916	36.92155
3	0.0129	0.504 ^a	19.76	194.36880	36.91972
4	0.0029	0.531 ^b	19.83	194.33660	36.90151
5	0.0002	0.522 ^c	20.30	194.35435	36.90672
A	...	0.527 ^a	19.71	194.34135	36.91943

^aSDSS DR18 (Almeida et al. 2023)

^bDEIMOS (This work)

^cDESI DR1 (DESI Collaboration et al. 2025)

^dDESI Legacy Survey DR10 (Dey et al. 2019)

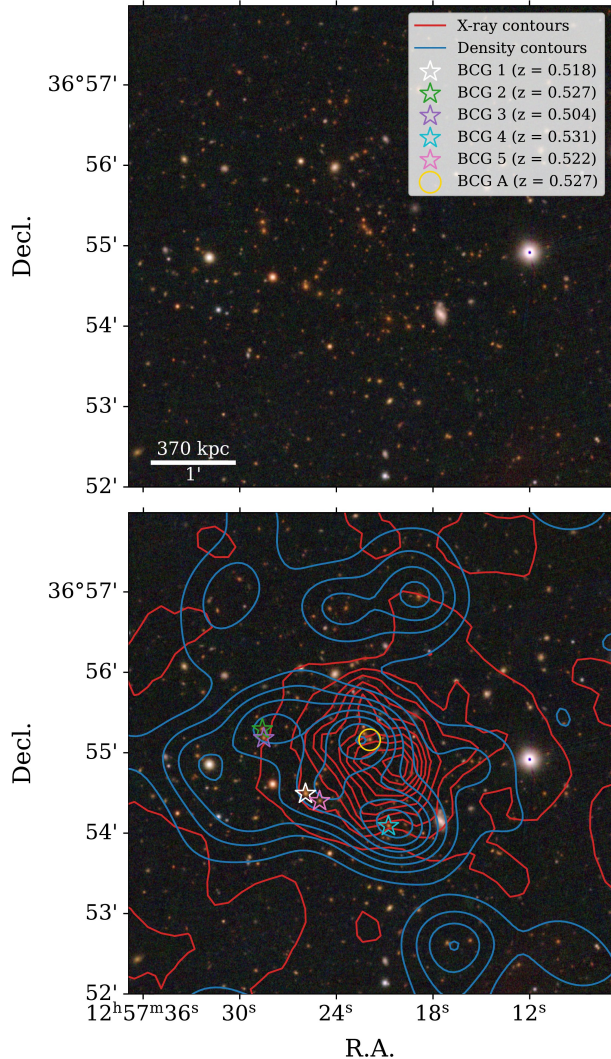


FIG. 32.— Optical image of RMJ1257. Top panel: $6'$ by $6'$ (2.22 by 2.22 Mpc) Pan-STARRS image. Bottom panel: red sequence density contours (blue), X-ray surface brightness contours (red), and BCG candidates identified by redMaPPer.

3.3.9. RM J125725.9+365429.4

RMJ1257 is another complicated cluster. The BCGs identified by redMaPPer form roughly along a line $\sim 400 \text{ kpc}$ east of the peak in the X-ray emission, Figure 32. We identified an additional bright cluster member, which we label BCG A, northeast of the X-ray peak, with an r -magnitude of 19.71, making it brighter than all but BCG 1 (Table 26). Luminosity density contours show two primary peaks located on BCGs A and 4, with the central peak extending towards BCGs 1 and 5. There is also an additional, smaller, peak located at BCGs 2/3 (Figure 32).

The redshift distribution, Figure 33, defines cluster members from $0.52 \leq z \leq 0.54$. In this range, a one-component fit is preferred and consistent with Gaussianity ($D = 0.12$, $p = 0.72$; $A^2 = 0.45$, $p = 0.26$). However, this excludes BCGs 1 and 3. If the range is extended down to $z = 0.50$ to capture those members, a

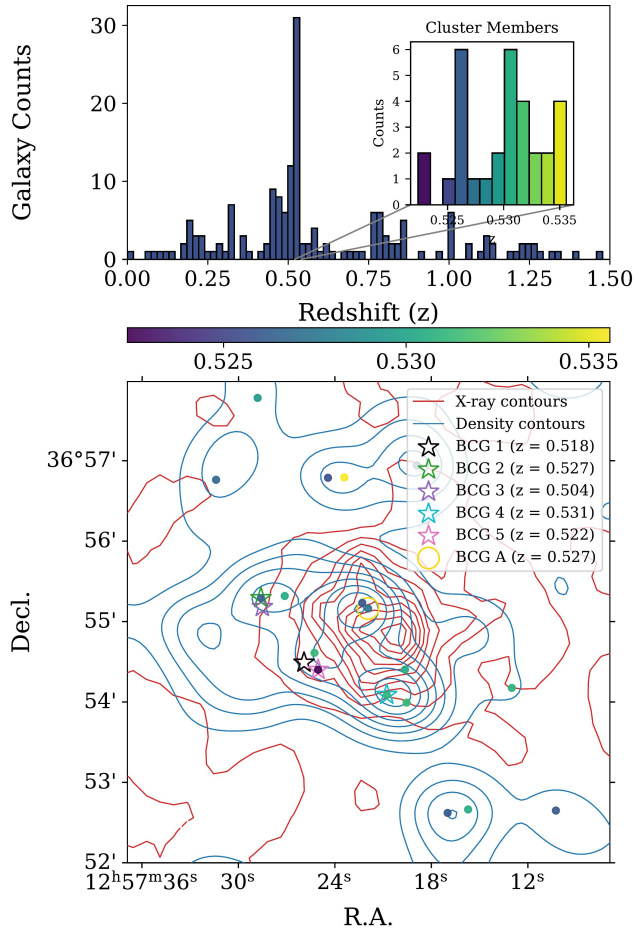


FIG. 33.— Redshift distribution of RMJ1257. Top panel: histogram of spectroscopic redshifts, combining archival data within $10'$ of the cluster with new observations from DEIMOS. The inset highlights galaxies in the redshift range $0.52 \leq z \leq 0.54$, which are classified as cluster members. Bottom panel: spatial distribution of those same members.

two-component GMM fit is preferred with 13 galaxies at $z = 0.51$ and 30 at 0.53 . The lower redshift group is spread widely through the entire $10'$ field of view, but does have a handful of members concentrated near BCG 3. With a velocity difference of $\sim 5000 \text{ km s}^{-1}$ between BCG 3 and the primary cluster, we consider this to be a foreground group. There is an additional foreground group at $z = 0.49$ with 16 members, also broadly covering the region, with some clustering near BCG 4.

Given the location of the X-ray peak and primary density peaks at BCG A and BCG 4, we divide the cluster into subclusters centered on those two BCGs (Figure 34). There is differentiation in redshift between the two subclusters, with a velocity difference of 820 km s^{-1} between subcluster means (Table 27). However, with only 7 and 9 members in each group, we cannot draw any strong conclusions. New DEIMOS spectroscopy was limited to a single mask, adding only 39 new redshifts. RMJ1257 has the lowest number of both spectroscopic and total cluster members in the sample.

RMJ1257 has the second lowest X-ray temperature in our sample at 4.04 keV , 1.2σ below the expected value of 5.71 keV , while its X-ray luminosity of $3.04 \times 10^{44} \text{ erg s}^{-1}$

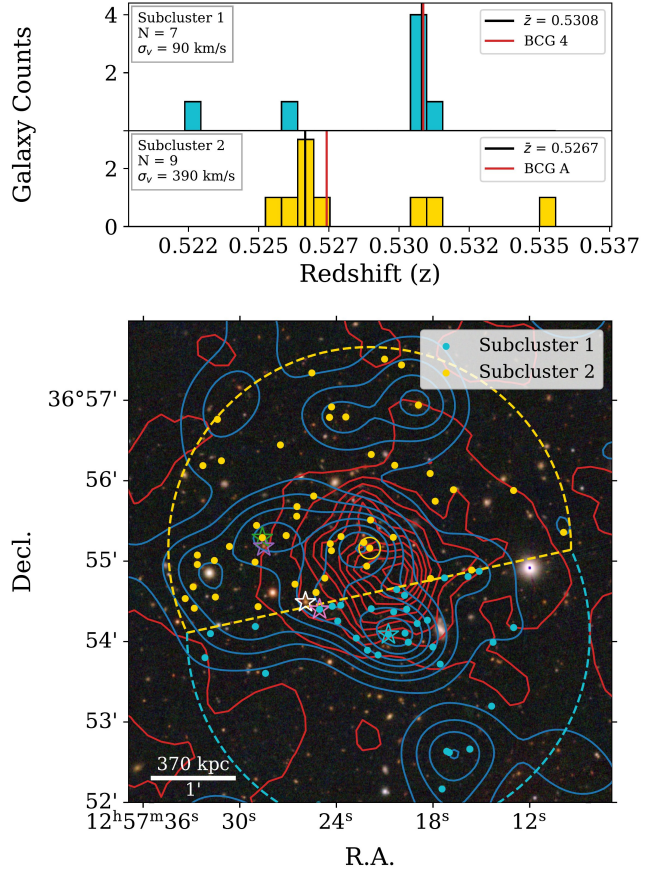


FIG. 34.— Subclustering analysis of RMJ1257. Bottom panel: spatial distribution of subcluster members, both spectroscopic and photometric, identified within regions defined by the bisector between BCG pairs and a radial distance of $2.5'$ from each BCG. Top panel: redshift distribution of the spectroscopic members of those regions.

slightly exceeds the expectation of $2.44 \times 10^{44} \text{ erg s}^{-1}$ (Table 8). RMJ1257 had the lowest XMM-Newton exposure time of any cluster in our sample with 14 ks, which was further diminished by extensive proton flaring, especially on the PN detector (only 1.08 ks of usable exposure, which we drop from our spectral fitting).

Given the displaced X-ray peak between BCGs 4 and A, we believe this to be a post-collision merger, with the BCGs separated by 410 kpc. The X-ray peak is 300 kpc from BCG 4 and 225 kpc from BCG A, offset from the presumed merger axis by $\sim 150 \text{ kpc}$. However, the lack of data gives us low confidence in this assessment. Additional spectroscopy (or weak lensing) would help to better define the subclusters involved while additional X-ray imaging is needed to compensate for the high flaring in this data. If the observed morphology is confirmed, RMJ1257 has the potential to be a promising dissociative merger.

3.3.10. RM J132724.2+534656.5

RMJ1327 is perhaps the most interesting system in our sample, with multiple well-separated clusters, highlighting the ability to identify subclusters from redMaPPer BCG separations. RedMaPPer assigns a probability of

TABLE 27
RMJ1257 SUBCLUSTER PROPERTIES

Subcluster	N	BCG	BCG z	Mean z	σ_v [km s $^{-1}$]
All	31	0.5301	720
1	7	4	0.531	0.5308	90
2	9	A	0.527	0.5267	390

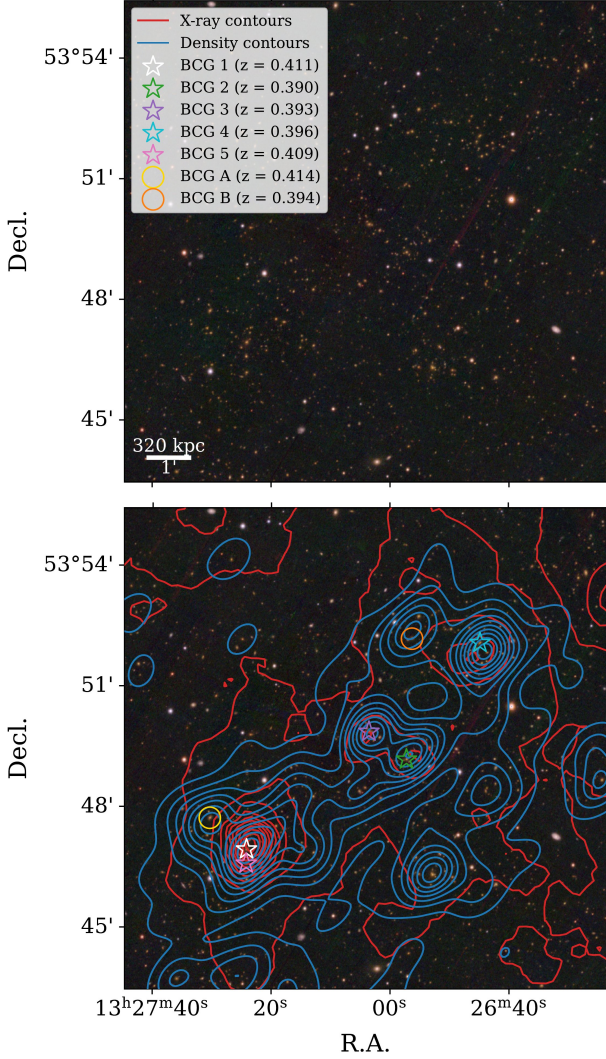


FIG. 35.— Optical image of RMJ1327. Top panel: 12' by 12' (3.84 by 3.84 Mpc) Pan-STARRS image. Bottom panel: red sequence density contours (blue), X-ray surface brightness contours (red), and BCG candidates identified by redMaPPer.

0.9436 to BCG 1 (Table 28) making it the dominant candidate, but still within our 0.98 threshold. We also identified two additional bright galaxies, listed as BCGs A and B, with magnitudes comparable to the BCGs identified by redMaPPer. The luminosity density and the XSB contours (Figure 35) show three primary subclusters: southeast, containing BCGs 1, 5, and A; center, containing BCGs 2 and 3; and northwest, with BCGs 4 and B. The undetected BCGs are associated with more minor structures than BCGs 1–5, justifying their exclu-

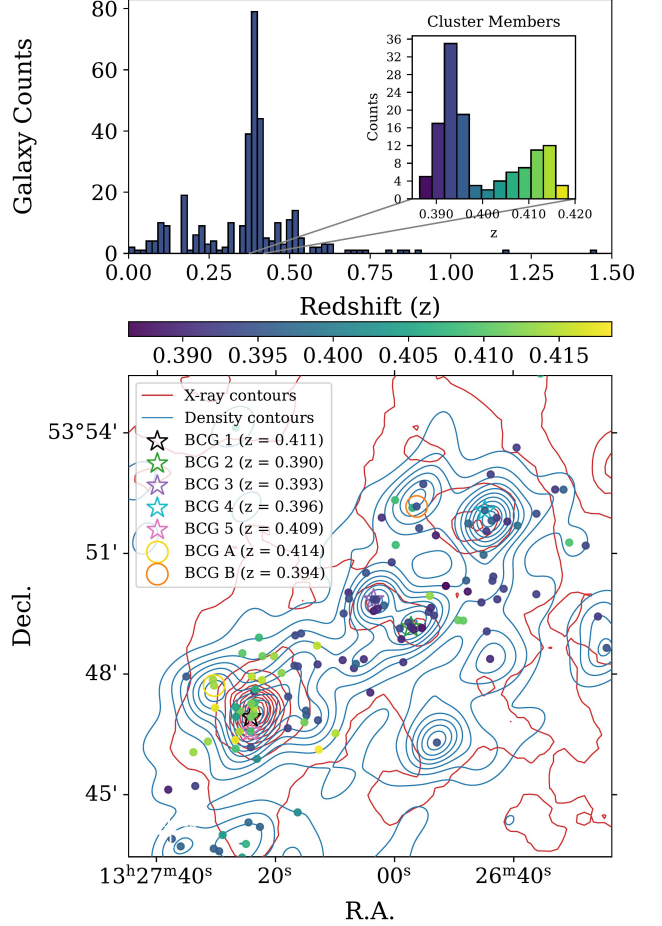


FIG. 36.— Redshift distribution of RMJ1327. Top panel: histogram of spectroscopic redshifts, combining archival data within 10' of the cluster with new observations from DEIMOS. The inset highlights galaxies in the redshift range $0.38 \leq z \leq 0.42$, which are classified as cluster members. Bottom panel: spatial distribution of those same members.

TABLE 28
RMJ1327 BCG INFORMATION

BCG	Probability	Redshift	r -mag ^d	RA [deg]	Dec [deg]
1	0.9436	0.411 ^a	18.90	201.85063	53.78235
2	0.0484	0.390 ^a	19.04	201.73846	53.81966
3	0.0029	0.393 ^a	18.26	201.76472	53.83118
4	0.0026	0.396 ^b	18.82	201.68665	53.86797
5	0.0025	0.409 ^a	19.12	201.85095	53.77650
A	...	0.414 ^a	18.57	201.87647	53.79540
B	...	0.394 ^c	19.28	201.73490	53.86985

^aDESI DR1 (DESI Collaboration et al. 2025)

^bSDSS DR18 (Almeida et al. 2023)

^cDEIMOS (This work)

^dDESI Legacy Survey DR10 (Dey et al. 2019)

sion from the top five candidates identified by redMaPPer. Additionally, the true brightest galaxy in the field ($r = 18.09$ from DESI Legacy Survey DR10 (Dey et al.

TABLE 29
RMJ1327 SUBCLUSTER PROPERTIES

Subcluster	N	BCG	BCG z	Mean z	σ_v [km s^{-1}]
All	124	0.3961	2140
1	30	1	0.411	0.4121	890
2	29	3	0.393	0.3918	510
3	26	4	0.396	0.3931	540

2019) and $z = 0.3945$ from DESI DR1 (DESI Collaboration et al. 2025)), located $\sim 3.5'$ south of BCG 2 and $\sim 4'$ west of BCG 1, was not identified. However, this galaxy was separately classified as a BCG using an optical selection algorithm utilizing a fit of the red sequence on SDSS DR7 data by Hao et al. (2010). While this galaxy has been previously identified as a BCG, it is relatively isolated and not associated with any extended X-ray emission, thus, we choose to omit it from our list of potential BCG candidates. Of note, the furthest separation between BCG candidates is $\sim 8'$ (~ 2.6 Mpc) between BCGs 1/5 and BCG 4, the largest in our sample, which could offer a way to identify similar extended systems.

The XSB contours are dominated by the southeastern subcluster. The central and northwestern subclusters have elevated X-ray emission, but are easily overwhelmed by the contour scale of the primary subcluster. Notably, there is no enhanced X-ray emission in the regions between the three subclusters. In addition to the three largest subclusters, there are several smaller structures that could themselves be involved in independent mergers. Each subcluster contains two BCG candidates, each associated with an overdensity in galaxies. The peak in the luminosity density containing a single galaxy west of BCG 1 is the previously identified BCG mentioned above.

The redshift distribution in the cluster redshift range of $0.38 \leq z \leq 0.42$ is best-fit with a two-component GMM corresponding to the two prominent peaks in Figure 36. Both are consistent with a Gaussian distribution ($D = 0.069$, $p = 0.83$; $A^2 = 0.25$, $p = 0.74$ at $\bar{z} = 0.393$ and $D = 0.10$, $p = 0.68$; $A^2 = 0.38$, $p = 0.40$ at $\bar{z} = 0.410$). The bottom panel of Figure 36 shows the southeastern subcluster at a distinctly higher redshift than the two other primary subclusters. To explore this further, we begin by dividing the field into regions separated by the bisectors between BCGs 1–3 and 3–4 and a $2.75'$ radius from each, shown in the bottom panel of Figure 37. The redshift distribution in the center panel shows the bimodality and the difference in redshifts between Subcluster 1 and Subclusters 2/3. Given such a clean separation, we elect to enforce a redshift range of $0.40 \leq z \leq 0.42$ for Subcluster 1, and $0.38 \leq z \leq 0.40$ for Subclusters 2 and 3. The resulting distributions are shown in the top panel of Figure 37 and given in Table 29. Subclusters 2 and 3 have similar distributions, with velocity dispersions of 510 km s^{-1} and 540 km s^{-1} , respectively, and a LOS velocity difference of 280 km s^{-1} between the subcluster means. Subcluster 1 is more broad, with $\sigma_v = 890 \text{ km s}^{-1}$. The ultimate LOS velocity difference between Subcluster 1 and Subclusters 2/3 is then 4200 km s^{-1} , too large for an active merger between Subclusters 1 and 2 at a projected separation of 1.5 Mpc.

Next, we take a closer look at each subcluster individ-

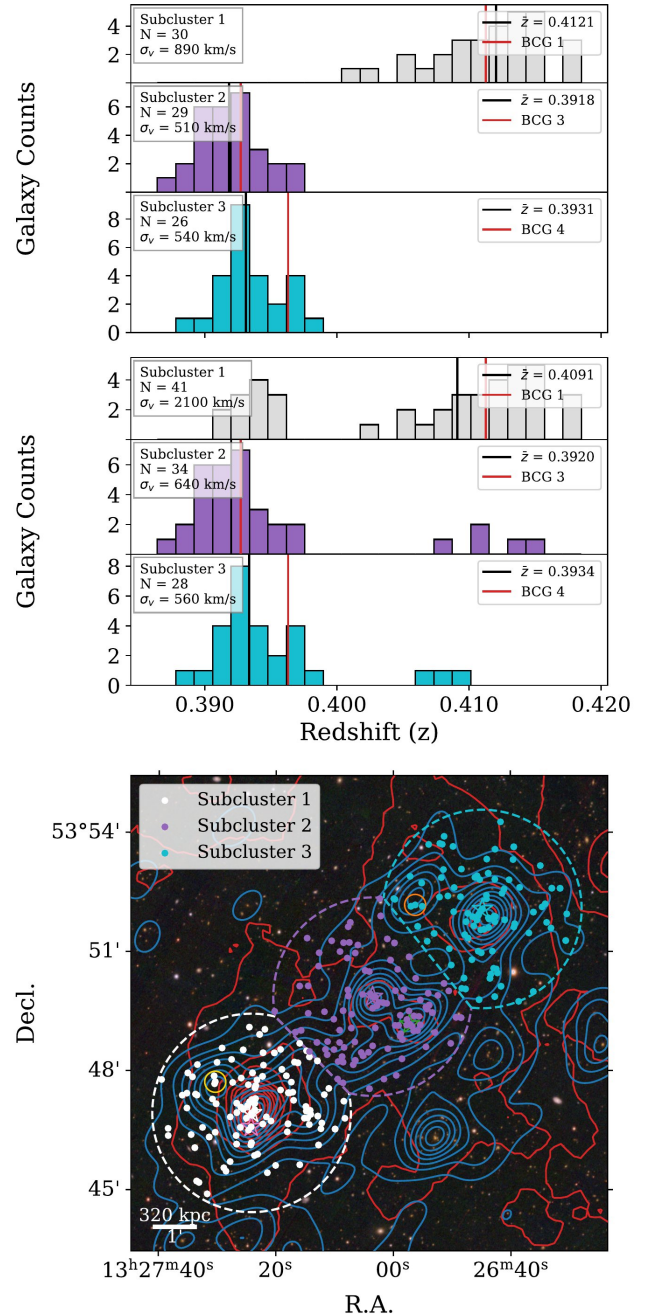


FIG. 37.— Subclustering analysis of the primary subclusters of RMJ1327. Bottom panel: full $12'$ field with the three primary subclusters defined by bisectors between BCGs 1, 3, and 4 and a $2.75'$ radius from each. The center set of histograms show the redshift distribution when considering the full range $0.38 \leq z \leq 0.42$, while the bottom histograms limit Subcluster 1 to the range $0.40 \leq z \leq 0.42$ and Subclusters 2 and 3 to the range $0.38 \leq z \leq 0.40$.

ually. We divide each subcluster into two regions defined by a bisector between BCGs and a radius of $1.75'$ from each (Figure 38).

- Subcluster 1, shown in the left panel, has two peaks in the luminosity density, but X-ray emission is almost entirely centered on BCG 1. This could

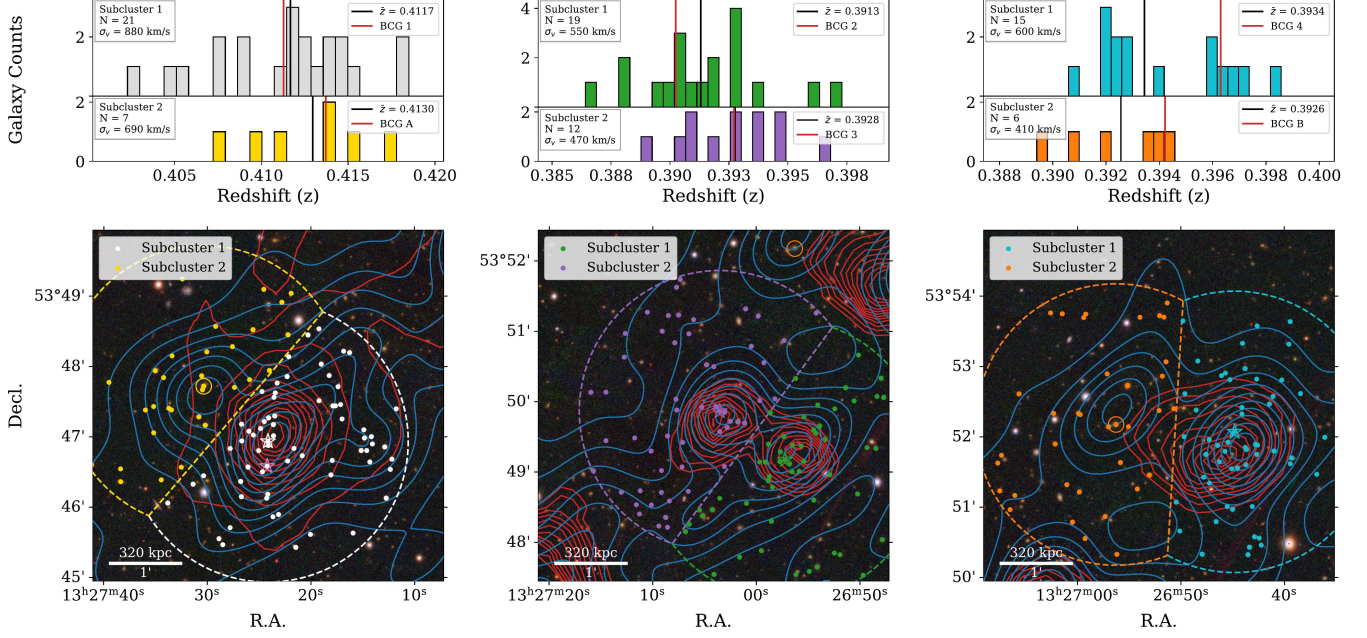


FIG. 38.— Subclustering analysis of the individual subclusters of RMJ1327. Each panel shows a $5'$ field about one of the primary subclusters shown in Figure 37, arranged from southeast to northwest, left to right. Regions are defined by the bisectors between relevant BCGs and a $1.75'$ radius from each BCG.

indicate gas-stripping from a recent merger, but there appears to be minimal disruption to the X-ray morphology. More likely, this is a minor merger or possibly even a relaxed cluster. The luminosity density in the northeast is dominated by BCG A and unweighted galaxy density contours are centered almost exclusively on BCG 1. This is also supported by X-ray temperatures and luminosities, which were extracted from a region centered on BCG 1, both being $\sim 0.5\sigma$ lower than predicted at 4.31 keV and 1.21×10^{44} erg s $^{-1}$ (Table 8). There was a fair amount of proton flaring, but all detectors had at least 10 ks of exposure.

- Subcluster 2, shown in the center panel, features two distinct luminosity density and XSB peaks, with both groups having similar redshifts. The X-ray morphology is somewhat disturbed, with a bridge in the XSB between the subclusters and each X-ray peak offset counterclockwise from their BCG, possibly indicating rotation. Of the three subclusters, this is the best candidate for a binary merger, possibly at a large impact parameter.
- Subcluster 3, shown in the far right panel, again has two luminosity density peaks, centered on BCGs 4 and B. The XSB is largely centered on BCG 4, but is extended towards BCG B with the peak offset from BCG 4 by ~ 100 kpc, possibly indicating a merger. However, the luminosity density peak near BCG B is largely dominated by the BCG and largely vanishes when considering unweighted galaxy density, calling into question the existence of a unique group.

While it does not appear that any of the three primary subclusters are actively merging with each other, each

of the three shows some evidence of being involved in binary mergers themselves. While not a clean binary system, RMJ1327 appears to be an excellent example of a dynamic system along a filament, warranting further observations.

3.3.11. *RM J163509.2+152951.5*

The top two most likely BCG candidates for RMJ1635 each have relatively large probabilities (0.5402 and 0.3727), with the third-ranked BCG at 0.0762 (Table 30). The luminosity density contours show two distinct peaks, one centered on BCG 3/5 and the other located between BCGs 1 and 4 (Figure 39). The X-ray surface brightness exhibits a disturbed morphology, with a primary peak coincident with BCG 3/5, and a secondary peak at BCG 4. The XSB is asymmetric, with pronounced edges south of BCG 3/5 as well as south of BCG 1, indicative of dynamic activity. These features are clearly visible in the smoothed XSB map (top panel of Figure 40) and are further emphasized in the gradient magnitude (center) and

TABLE 30
RMJ1635 BCG INFORMATION

BCG	Probability	Redshift	r -mag ^c	RA [deg]	Dec [deg]
1	0.5402	0.474 ^a	19.43	248.78848	15.49764
2	0.3727	0.472 ^a	19.04	248.76398	15.48361
3	0.0762	0.481 ^b	18.99	248.77975	15.48494
4	0.0069	0.478 ^b	19.85	248.79898	15.49102
5	0.0040	0.478 ^a	19.81	248.77858	15.48468

^aSDSS DR18 (Almeida et al. 2023)

^bDEIMOS (This work)

^cDESI Legacy Survey DR10 (Dey et al. 2019)

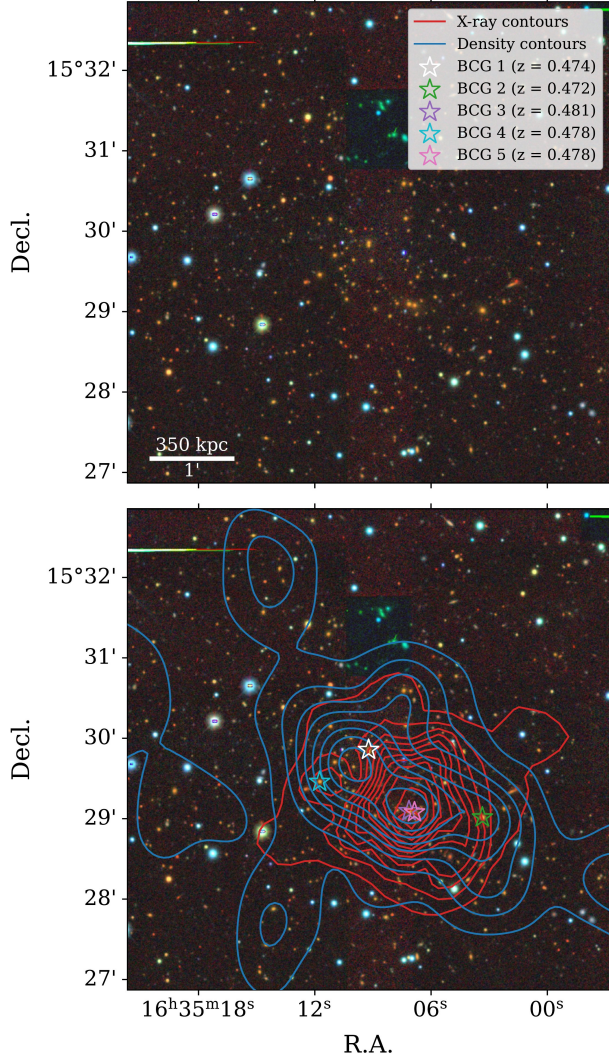


FIG. 39.— Optical image of RMJ1635. Top panel: 6' by 6' (2.10 by 2.10 Mpc) Legacy Survey image. Bottom panel: red sequence density contours (blue), X-ray surface brightness contours (red), and BCG candidates identified by redMaPPer.

unsharp-masked (bottom) images.

A one-dimensional surface brightness profile extracted across the southern edge of the cluster (marked ‘S’ in the top panel of Figure 40) shows a clear, abrupt change in surface brightness on both the eastern and western sides of the feature. From the gradient magnitude and unsharp-mask, it is evident that the northeastern feature (marked ‘N’) has an even more severe gradient than the southern edge. Extracting a one-dimensional profile across that feature shows the rapid change in XSB and also resolves the secondary XSB peak near BCG 4.

In the cluster redshift range of $0.465 \leq z \leq 0.485$, the redshift distribution (Figure 41) is well fit by a single Gaussian ($D = 0.067$, $p = 0.87$; $A^2 = 0.31$, $p = 0.57$), and no foreground or background structures contaminate the field. Spatially, the highest redshift galaxies in the cluster are preferentially located in the south near BCG 2 (bottom panel of Figure 41). Dividing the cluster into

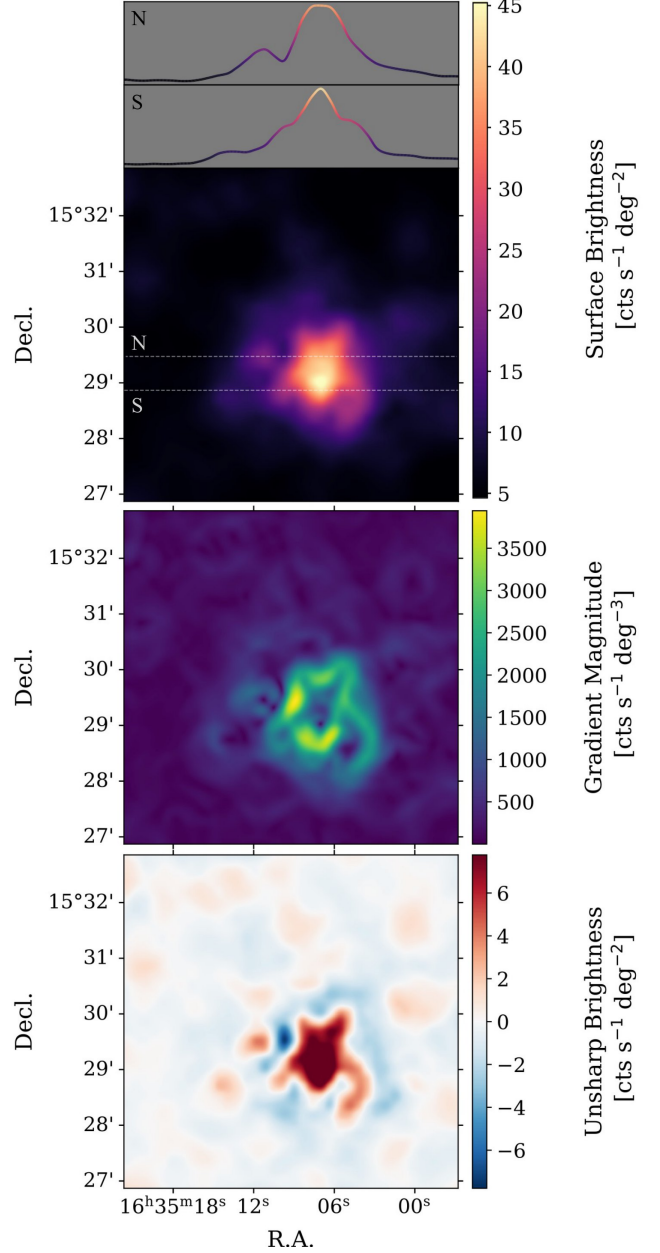


FIG. 40.— RMJ1635 X-ray features. The top panel shows the X-ray surface brightness smoothed with a 10'' kernel and reprojected on an 800×800 pixel grid with the extracted one-dimensional profiles. The dashed lines show where the profiles were extracted across the southern and northeastern edges. The center panel displays the gradient magnitude of the brightness. The bottom panel shows residual features after unsharp masking, where an image smoothed with a kernel of 50'' is subtracted from the image smoothed at 10''.

subclusters centered on BCGs 1 and 3 (Figure 42) shows a relatively tight distribution of redshifts around BCG 1, with a velocity dispersion of 640 km s^{-1} . Subcluster 2 is more broadly distributed, with $\sigma_v = 1110 \text{ km s}^{-1}$. Both subclusters have approximately the same mean redshift, with a velocity difference of $< 50 \text{ km s}^{-1}$ (Table 31).

The X-ray temperature of 5.74 keV is consistent with the predicted value, while the X-ray luminosity is elevated by $\sim 1\sigma$ at $4.09 \times 10^{44} \text{ erg s}^{-1}$ (Table 8). The bimodal galaxy distribution, disturbed X-ray morphology,

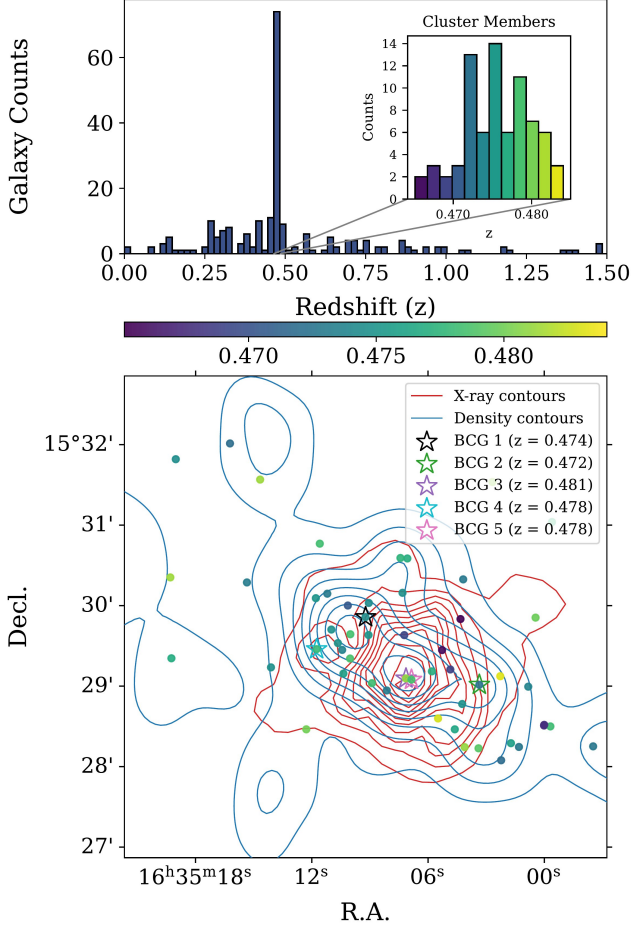


FIG. 41.— Redshift distribution of RMJ1635. Top panel: histogram of spectroscopic redshifts, combining archival data within $10'$ of the cluster with new observations from DEIMOS. The inset highlights cluster members in the redshift range $0.465 \leq z \leq 0.485$.

TABLE 31
RMJ1635 SUBCLUSTER PROPERTIES

Subcluster	N	BCG	BCG z	Mean z	σ_v [km s $^{-1}$]
All	76	0.4756	870
1	25	1	0.474	0.4755	640
2	25	3	0.481	0.4754	1110

and presence of sharp surface brightness variations collectively indicate a dynamically active system. The small LOS velocity difference between the two galaxy concentrations indicates this is likely a merger near the plane of the sky. While the XSB peak is not displaced from the primary cluster, this is a relatively clean system and an excellent candidate for follow-up with weak lensing studies.

3.3.12. RM J232104.1+291134.0

Our final cluster, RMJ2321, is another complicated system. The top three BCGs are listed with probabilities of 0.7827, 0.1679, and 0.0460 (Table 32). However, BCGs 1 and 2 have a large LOS velocity difference of ~ 3200 km s $^{-1}$, indicating either a significant LOS component to a potential merger or foreground/background

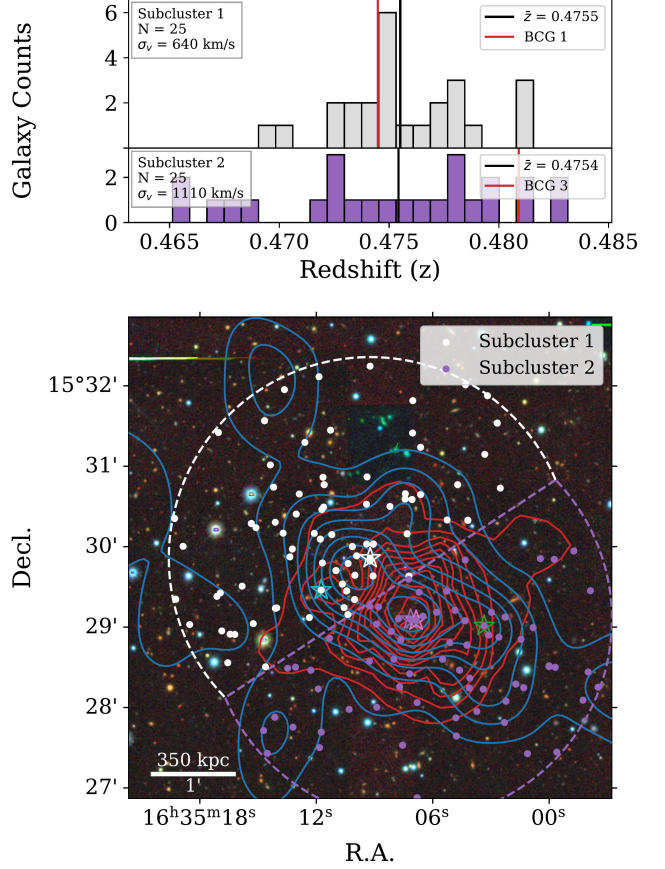


FIG. 42.— Subclustering analysis of RMJ1635. Bottom panel: spatial distribution of subcluster members, both spectroscopic and photometric, identified within regions defined by the bisector between BCG pairs and a radial distance of $2.5'$ from the BCG in each region. Top panel: redshift distribution of the spectroscopic members of those regions.

group. There are multiple peaks in the luminosity density contours: one located near BCG 1/4, another at BCG 5, and two in the north near BCG 2 (Figure 43). The X-ray surface brightness is peaked just northwest of BCG 1/4, with a secondary peak near BCG 3. The X-ray contours also extend out towards BCG 2.

A GMM fit of the full redshift distribution is best-fit with three total components but contains only a single

TABLE 32
RMJ2321 BCG INFORMATION

BCG	Probability	Redshift	r -mag ^c	RA [deg]	Dec [deg]
1	0.7827	0.485 ^a	18.64	350.26727	29.19291
2	0.1679	0.501 ^a	19.13	350.24640	29.21685
3	0.0460	0.494 ^a	19.27	350.24790	29.20312
4	0.0020	0.489 ^a	20.72	350.26820	29.19231
5	0.0015	0.497 ^b	19.70	350.24000	29.19139

^aSDSS DR18 (Almeida et al. 2023)

^bDEIMOS (This work)

^cDESI Legacy Survey DR10 (Dey et al. 2019)

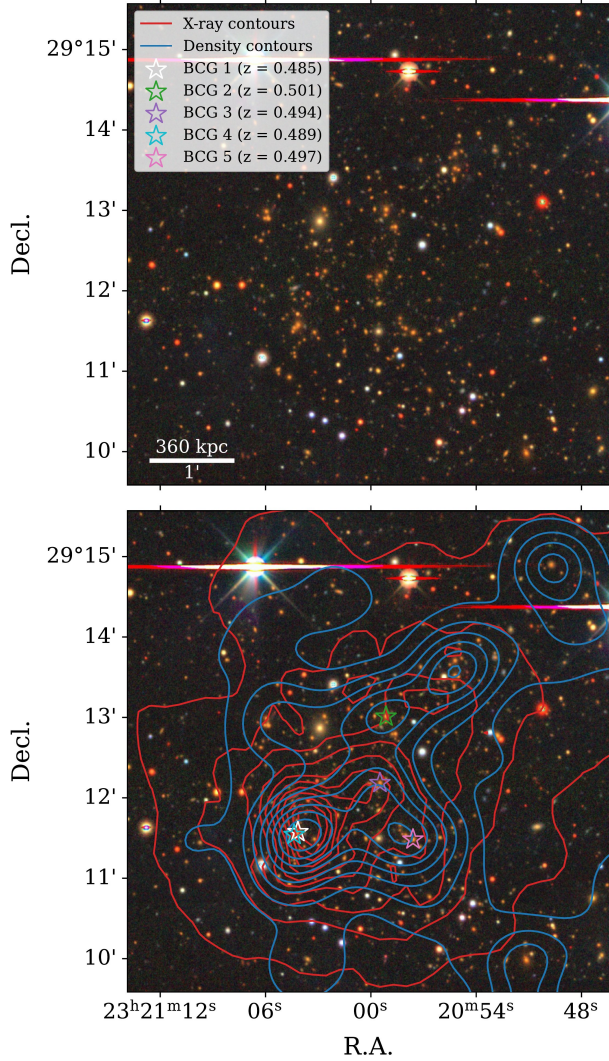


FIG. 43.— Optical image of RMJ2321. Top panel: 6' by 6' (2.16 by 2.16 Mpc) Legacy Survey image. Bottom panel: red sequence density contours (blue), X-ray surface brightness contours (red), and BCG candidates identified by redMaPPer.

narrow Gaussian and shows no foreground or background structures (Figure 44). In the cluster redshift range of $0.48 \leq z \leq 0.51$, the distribution is consistent with Gaussianity by the KS test ($D = 0.104$, $p = 0.15$), but not the AD test ($A^2 = 1.60$, $p = 0.0004$). There is a gradient in the spatial distribution of redshifts, following the trend from BCGs 1 and 2, with the southeast subcluster at a lower redshift. To investigate further, we divided the cluster into regions centered on BCGs 1, 2, and 3 (left panel of Figure 45). If there is a distinct subcluster associated with BCG 3, it also likely includes BCG 5. However, it is unclear which would be the primary BCG of the subcluster. BCG 3 is brighter ($r = 19.27$ versus 19.70) and associated with a peak in the XSB. However, BCG 5 is associated with a peak in the luminosity density. A merger axis between BCGs 1 and 3 places both XSB peaks between the BCGs. Subclusters 1 and 2 have noticeable differences in redshift, with a velocity

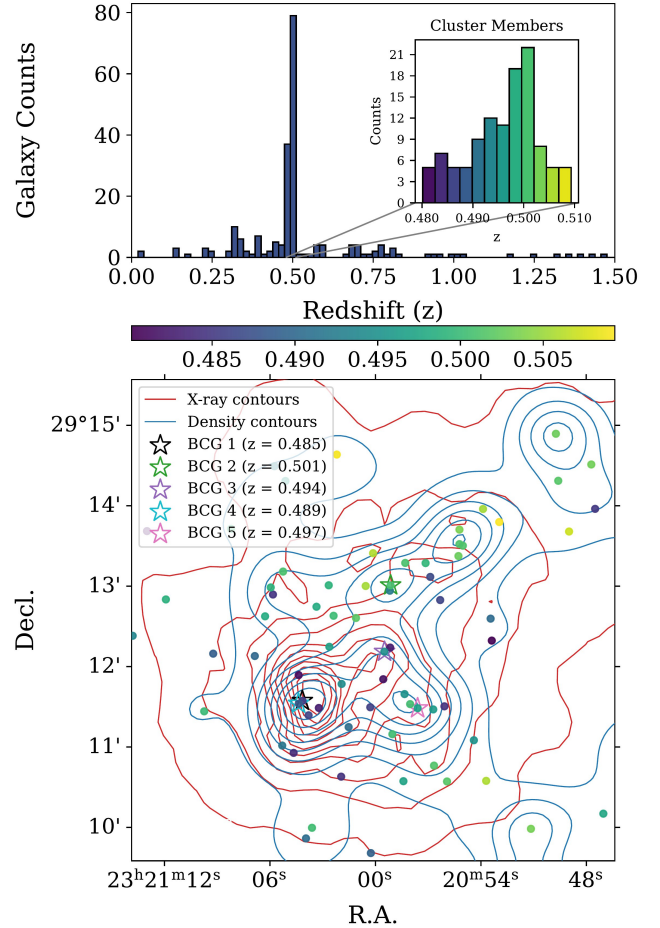


FIG. 44.— Redshift distribution of RMJ2321. Top panel: histogram of spectroscopic redshifts, combining archival data within 10' of the cluster with new observations from DEIMOS. The inset highlights galaxies in the redshift range $0.48 \leq z \leq 0.51$, which are classified as cluster members. Bottom panel: spatial distribution of those same members.

difference of 2000 km s^{-1} between subcluster means (Table 33). Subcluster 3 has members across both redshift ranges.

We then combine Subclusters 1 and 3 (center panel of Figure 45) which increases the dispersion on Subcluster 1 to 1500 km s^{-1} , but decreases the LOS velocity difference between means to 1600 km s^{-1} . We also consider a scenario combining Subclusters 2 and 3. This increases the dispersion on Subcluster 2 to 1500 km s^{-1} with a velocity difference between means of 1740 km s^{-1} .

While the cluster redshift range is best fit with a single component Gaussian ($\text{BIC} = -794$), a two-component GMM yields a nearly identical BIC of -793 , indicating no strong statistical preference between the models. To explore these two distributions further, we divide the cluster into two redshift bins, $0.480 \leq z \leq 0.495$ and $0.495 \leq z \leq 0.510$, and examine their spatial distributions in Figure 46. From this, Subclusters 1 and 2 appear distinct, whereas the region of Subcluster 3 remains ambiguous. It contains approximately equal numbers of galaxies from each redshift bin, with BCGs 3 and 5 divided between the bins. Adjusting the redshift boundary slightly, from 0.495 to 0.494 or 0.497, to capture both

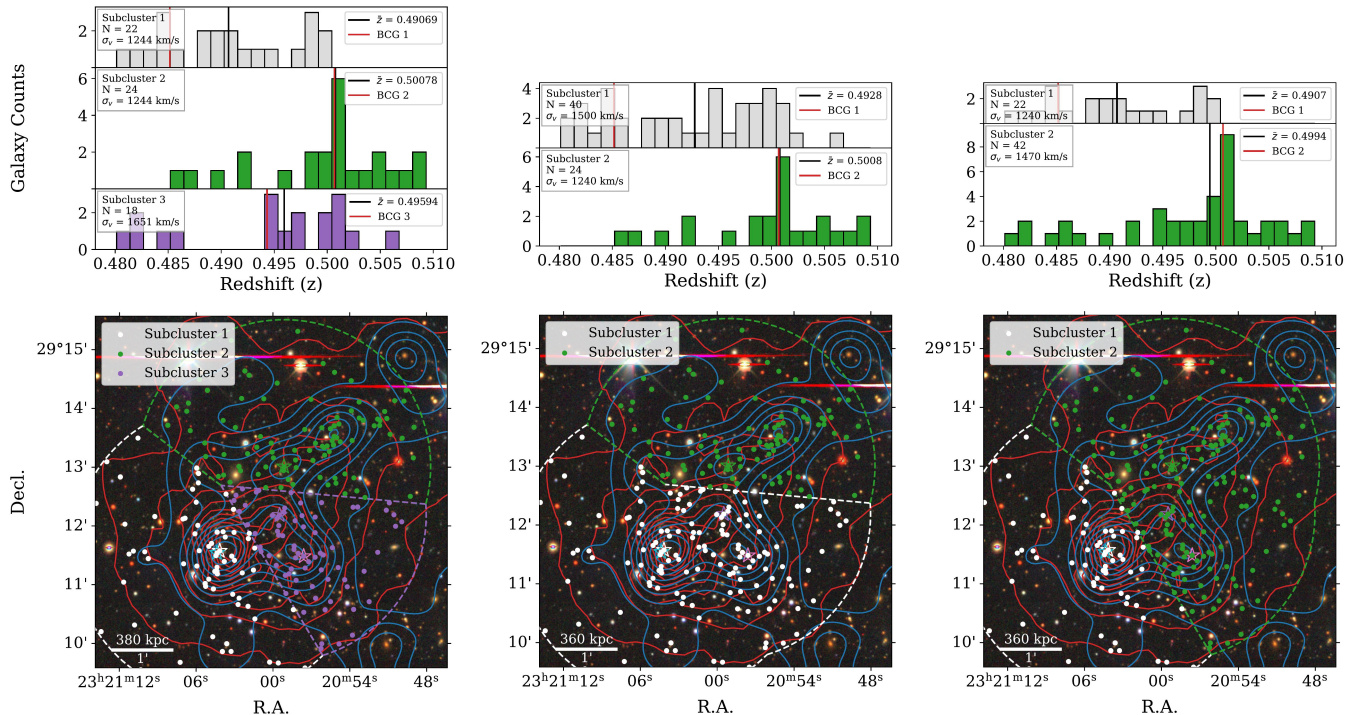


FIG. 45.— Subclustering analysis of RMJ2321. Bottom panel: spatial distribution of subcluster members, both spectroscopic and photometric, identified within regions defined by the bisector between BCG pairs and a radial distance of $2.5'$ from the BCG in each region. Top panel: redshift distribution of the spectroscopic members of those regions.

TABLE 33
RMJ2321 SUBCLUSTER PROPERTIES

Subcluster	N	BCG	BCG z	Mean z	σ_v [km s^{-1}]
All	113	0.4970	1440
1	22	1	0.485	0.4907	1240
2	24	2	0.501	0.5008	1240
3	18	3	0.494	0.4959	1650

BCGs in the same bin biases the observed density contours somewhat, but the general morphology of an extension in the low redshift contours towards BCG 3 and a concentration in high redshift members near BCG 5 remains.

RMJ2321 has the highest X-ray luminosity in the sample at $7.20 \times 10^{44} \text{ erg s}^{-1}$, and second-highest X-ray temperature, 8.62 keV (Table 8). However, it also has the highest richness in our sample, at $\lambda = 239$ (Table 6). This places both the X-ray temperature and luminosity only $\lesssim 0.5\sigma$ above the expected values. RMJ2321 (PSZ2 G100.22-29.64) was also studied as one of the LOFAR–Planck SZ clusters, where [Botteon et al. \(2022\)](#) report no diffuse emission.

The disturbed X-ray and luminosity density morphologies are strongly suggestive of merging activity, but the underlying substructure remains uncertain. One possible configuration is a merger between Subclusters 1 and 3 at the lower redshift, with Subcluster 2 in the background; however, the extent to which Subcluster 3 represents a distinct system, rather than a mixture of interlopers from Subclusters 1 and 2, is unclear. Any active merger between Subclusters 1 and 2 would require a large LOS velocity component, complicating modeling. Additional

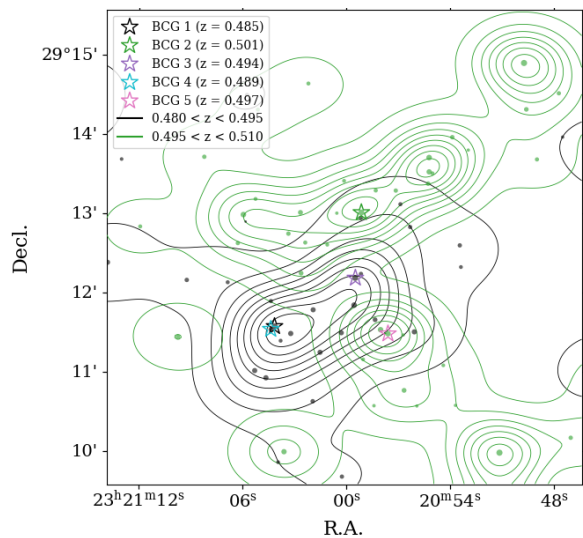


FIG. 46.— Distribution of galaxies in RMJ2321 separated by redshift. Contours show the luminosity-weighted density of spectroscopic members in each redshift bin. Individual galaxies are indicated by markers sized proportional to their luminosity.

spectroscopy focused on Subclusters 2 and 3 would be particularly useful in determining the substructure of the cluster.

4. SUMMARY AND CONCLUSION

We have presented X-ray and spectroscopic follow-up of 12 galaxy clusters selected from the redMaPPer catalog using optical indicators of binarity, forming the core sample of the X-SORTER program. Our selection aimed

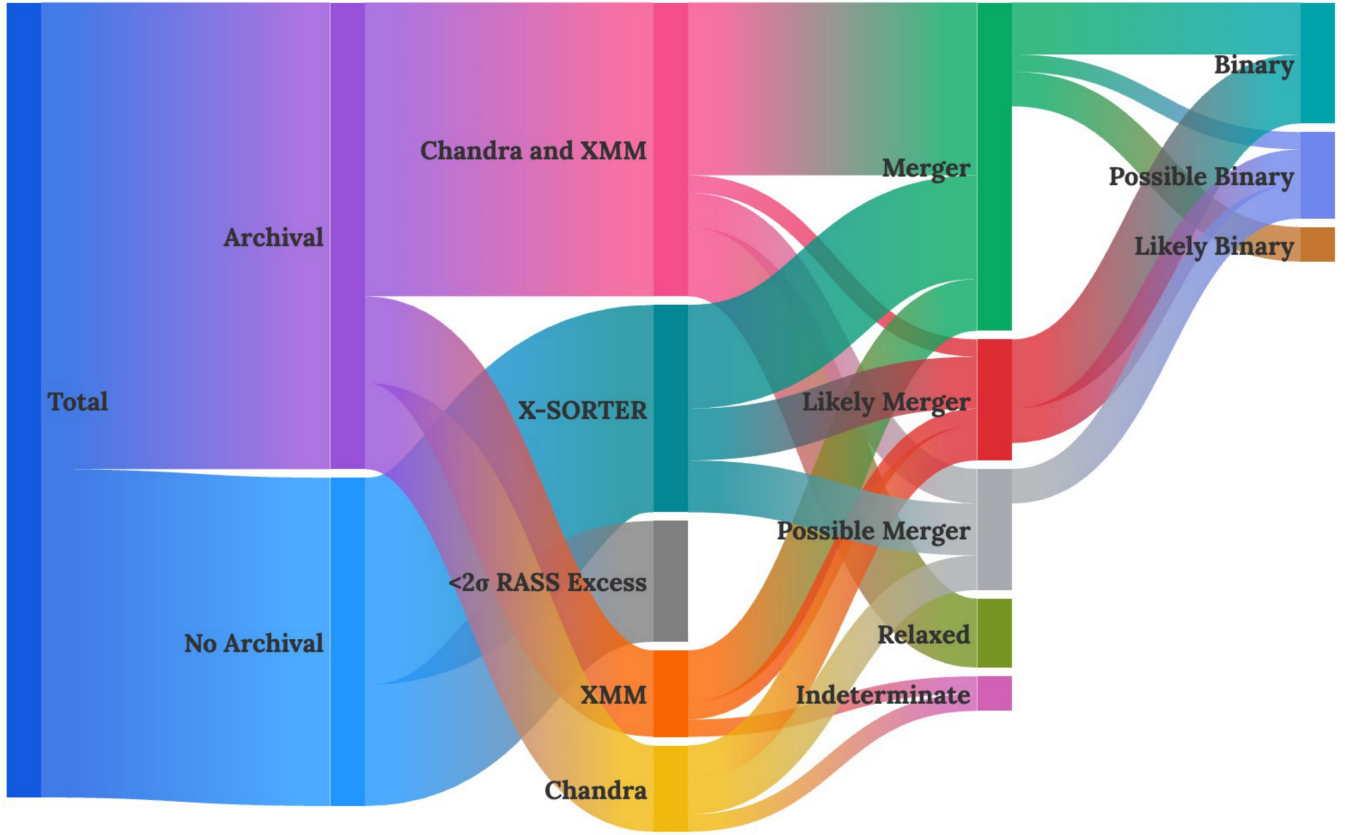


FIG. 47.— Flow diagram summarizing the classification of cluster candidates across the full program. Clusters with archival X-ray data are categorized according to classifications given in Tables 1 to 3 while new designations are assigned to the X-SORTER sample. Binarity classifications are limited to the X-SORTER systems presented in this work.

to identify massive, dissociative mergers by requiring low BCG probability (< 0.98), projected BCG separations exceeding $0.95'$, and richness $\lambda \geq 120$. These criteria were designed to preferentially select post-pericenter, binary mergers observable near the plane of the sky—ideal conditions for constraining dark matter self-interactions through the spatial offsets between galaxies, gas, and dark matter.

While only a handful of the 12 observed clusters in this sample can be modeled as clean binary mergers, the success rate in identifying disturbed and dynamically active systems remains high. The majority of clusters show clear evidence of merging activity, even if the underlying substructure is somewhat ambiguous. No clusters from the sample are definitively relaxed systems, while multiple appear to be premerger or multi-body systems, illustrating the diversity of dynamical states that can arise from a selection based on optical BCG properties.

To provide a consistent framework for comparison, we assign qualitative classifications based on the combined X-ray morphology, optical luminosity density, and redshift distribution. Systems designated as *Mergers* exhibit clearly disturbed X-ray morphologies accompanied by identifiable substructure. *Likely Mergers* show similar signatures, but with some ambiguity in the merger geometry or subcluster separations. *Possible Mergers* display asymmetric or disturbed X-ray emission that may be consistent with interaction, though a single dynamically complex halo cannot be ruled out. Assessments

of binarity are based primarily on the presence of multiple peaks in the luminosity density map. These classifications are intended as descriptive guides rather than definitive dynamical determinations and may evolve with additional observations. These classifications, along with classifications from the full program, including archival results, are summarized in Figure 47.

Below, we summarize the results for the 12 X-SORTER targets presented in this work; candidates are listed by ascending RA in each category:

Top Binary Merger Candidates—

- **RMJ0219** – Binary merger, likely post-pericenter and near the plane of the sky; X-ray contours show dual peaks with a bullet-like feature.
- **RMJ0926** – Binary merger. Highest T_X in the sample and L_X is $>1.5\sigma$ greater than expected; XSB is extended along the presumed merger axis with a single peak between merging groups.
- **RMJ1219** – Confirmed dissociative merger; multi-wavelength follow-up confirms post-pericenter scenario, but weak lensing by Stancioli et al. (2026) reveals additional possible substructure.
- **RMJ1635** – Merger, likely binary; two clear peaks in luminosity density and sharp features in the X-ray emission.

Likely Binary Merger Candidates—

- **RMJ0003** – Likely merger, possibly binary. X-ray emission is primarily located with the top BCG candidate and is elongated along a presumed merger axis, but also exhibits an offset X-ray peak.
- **RMJ0109** – Merger, possibly binary. X-ray peak is offset between two galaxy overdensities. Role of BCG A, which was not identified by redMaPPer, is unclear.
- **RMJ0829** – Likely merger, possibly binary. Disturbed X-ray morphology and two dominant luminosity density peaks, but possible additional substructure; high L_X and candidate radio halo by Botteon et al. (2022).
- **RMJ1257** – Merger, likely binary. XSB peak offset between two peaks in the luminosity density; low L_X , T_X , X-ray exposure time, and spectroscopic members.

Possible Binary Merger Candidates—

- **RMJ0801** – Possible merger, possibly binary; Elongated gas and galaxy contours with three coaxial galaxy density peaks; X-ray peak along the presumed merger axis and slightly offset towards the southern luminosity density peak. T_X exceeds 1.6σ above the value predicted from richness scaling relation.
- **RMJ1043** – Likely merger, possibly binary. Moderately disturbed system with three luminosity density peaks; possible dissociative merger between two of the three subclusters.

Complex Systems—

- **RMJ1327** – Possible merger, not binary. Low temperature system with three well-separated subclusters along a filamentary structure. Possible binary merger within central subcluster.
- **RMJ2321** – Likely merger, possibly binary. Complicated, disturbed system, with ambiguous substructure. Possibly binary with background contamination.

Taken together, these results show that redMaPPer-based selection is effective at identifying disturbed and dynamically complex clusters. None of the 12 systems is definitively relaxed, and several are strong candidates for binary, post-pericenter mergers conducive to simple modeling. This is even more apparent when considering the full program of 46 targets meeting our selection criteria, which includes 27 clusters with archival X-ray data (22 *Chandra*, 5 XMM-*Newton*). Among those with archival data, ten are previously known mergers and 11 are disturbed systems, and several high-value dissociative mergers (e.g., Abell 56, RMJ1508, and RMJ1219) were identified by this approach.

However, our X-SORTER sample also demonstrates that BCG-based selection alone does not uniquely isolate simple binary-merger geometries; while many of

the systems are dynamically active, few are clean two-body mergers. In addition, several systems (RMJ0109, RMJ0801, RMJ1219, RMJ1257, and RMJ1327) have merger scenarios involving BCGs that were not among redMaPPer’s top candidates, making these partly serendipitous discoveries. These results motivate combining BCG probability and separation with additional optical information. Incorporating BCG properties into broader optical selection frameworks, such as that of Wen et al. (2024), may improve the yield of clean binary systems.

Even with these limitations, BCG probabilities and separations provide a useful and inexpensive first step toward constructing the larger, controlled samples needed for statistical studies of cluster mergers. The sample presented here provides a foundation for targeted multi-wavelength follow-up. Weak lensing will be essential for constraining subcluster masses and confirming merger geometries, while radio observations can identify relics and halos diagnostic of the merger stage. Together with the archival systems, this program contributes to a growing, uniformly selected ensemble of merging clusters, a resource valuable not only for constraining dark matter self-interactions, but also for studies of ICM dynamics, structure formation, and galaxy evolution in disturbed environments.

ACKNOWLEDGMENTS

Support for this work was provided by the National Science Foundation under grant NSF 2308383.

This work is based in part on observations obtained with XMM-*Newton*, an ESA science mission with instruments and contributions directly funded by ESA Member States and NASA. We thank the XMM-*Newton* operations team for their support of this program.

Spectroscopic data were obtained at the W. M. Keck Observatory using the DEIMOS instrument, which is operated as a scientific partnership among the California Institute of Technology, the University of California and the National Aeronautics and Space Administration. The Observatory was made possible by the generous financial support of the W.M. Keck Foundation. We are grateful to the Keck Observatory staff and observing assistants for their expert support. The authors wish to recognize and acknowledge the very significant cultural role and reverence that the summit of Mauna Kea has always had within the indigenous Hawaiian community. We are most fortunate to have the opportunity to conduct observations from this mountain.

This research has made use of data obtained from the Chandra Data Archive and the *ROSAT* All-Sky Survey in the target selection process.

This research has made use of the NASA/IPAC Extragalactic Database (NED), which is funded by the National Aeronautics and Space Administration and operated by the California Institute of Technology.

This work has made use of data from the Dark Energy Spectroscopic Instrument (DESI) Data Release 1 and from the Sloan Digital Sky Survey (SDSS) Data Release 18. Funding for the DESI Project has been provided by the U.S. Department of Energy, the National Science Foundation, and participating institutions. Funding for the SDSS has been provided by the Alfred P. Sloan Foundation, the U.S. Department of Energy Office of Science,

and participating institutions.

This research has made use of the Pan-STARRS1 Surveys (PS1) and imaging data from the DESI Legacy Imaging Surveys (DECaLS, BASS, and MzLS).

FACILITIES

XMM (EPIC), Keck:II (DEIMOS)

SOFTWARE

SAS (Ochsenbein et al. 2004), ESAS (Snowden & Kuntz 2024), XSPEC (Arnaud 1996), PyeIt (Prochaska et al. 2020), Astropy (Astropy Collaboration et al. 2013, 2018, 2022), Astroquery (Ginsburg et al. 2019), SciPy (Virtanen et al. 2020), scikit-image (van der Walt et al. 2014), scikit-learn (Pedregosa et al. 2011), reproject (Robitaille et al. 2020)

APPENDIX

REDSHIFT CATALOG

Table 34 lists newly obtained spectroscopic redshifts for galaxies in the 12 X-SORTER cluster fields observed with Keck/DEIMOS. The observations, mask design, and reduction procedures are described in §2.3. Redshifts were measured via cross-correlation with galaxy templates following the method of Wittman et al. (2023), with typical statistical uncertainties of $\lesssim 10^{-4}$.

TABLE 34
NEW SPECTROSCOPIC REDSHIFTS FROM KECK/DEIMOS

Cluster	RA [deg]	Dec [deg]	Redshift	Error
RMJ000343.8+100123.8	0.854225	9.982806	0.376286	7.8e-05
RMJ000343.8+100123.8	0.874092	9.985403	0.376233	8.1e-05
RMJ000343.8+100123.8	0.874900	9.982392	0.375552	7.3e-05
RMJ000343.8+100123.8	0.884100	9.992076	0.266945	1.6e-05
RMJ000343.8+100123.8	0.886304	9.989572	0.375704	3.0e-05

Note. – This table is published in its entirety in machine-readable format at Hopp et al. (2026). A portion is shown here for guidance regarding its form and content.

REFERENCES

- Acebron, A., Zitrin, A., Coe, D., et al. 2020, *ApJ*, 898, 6, doi: [10.3847/1538-4357/ab929d](https://doi.org/10.3847/1538-4357/ab929d)
- Albuquerque, R. P., Machado, R. E. G., & Monteiro-Oliveira, R. 2024, *MNRAS*, 530, 2146, doi: [10.1093/mnras/stae1004](https://doi.org/10.1093/mnras/stae1004)
- Almeida, A., Anderson, S. F., Argudo-Fernández, M., et al. 2023, *ApJS*, 267, 44, doi: [10.3847/1538-4365/acda98](https://doi.org/10.3847/1538-4365/acda98)
- Arendt, A. R., Perrott, Y. C., Contreras-Santos, A., et al. 2024, *MNRAS*, 530, 20, doi: [10.1093/mnras/stae568](https://doi.org/10.1093/mnras/stae568)
- Arnaud, K. A. 1996, in *Astronomical Society of the Pacific Conference Series*, Vol. 101, *Astronomical Data Analysis Software and Systems V*, ed. G. H. Jacoby & J. Barnes, 17
- Arnaud, M., Pointecouteau, E., & Pratt, G. W. 2005, *A&A*, 441, 893, doi: [10.1051/0004-6361:20052856](https://doi.org/10.1051/0004-6361:20052856)
- Arnaud, M., Majerowicz, S., Lumb, D., et al. 2002, *A&A*, 390, 27, doi: [10.1051/0004-6361:200206669](https://doi.org/10.1051/0004-6361:200206669)
- Astropy Collaboration, Robitaille, T. P., Tollerud, E. J., et al. 2013, *A&A*, 558, A33, doi: [10.1051/0004-6361/201322068](https://doi.org/10.1051/0004-6361/201322068)
- Astropy Collaboration, Price-Whelan, A. M., Sipőcz, B. M., et al. 2018, *AJ*, 156, 123, doi: [10.3847/1538-3881/aabc4f](https://doi.org/10.3847/1538-3881/aabc4f)
- Astropy Collaboration, Price-Whelan, A. M., Lim, P. L., et al. 2022, *ApJ*, 935, 167, doi: [10.3847/1538-4357/ac7c74](https://doi.org/10.3847/1538-4357/ac7c74)
- Birzan, L., Rafferty, D. A., Cassano, R., et al. 2019, *MNRAS*, 487, 4775, doi: [10.1093/mnras/stz1456](https://doi.org/10.1093/mnras/stz1456)
- Boschin, W., Barrena, R., & Girardi, M. 2009, *A&A*, 495, 15, doi: [10.1051/0004-6361:200811043](https://doi.org/10.1051/0004-6361:200811043)
- Botteon, A., Shimwell, T. W., Bonafede, A., et al. 2019, *A&A*, 622, A19, doi: [10.1051/0004-6361/201833861](https://doi.org/10.1051/0004-6361/201833861)
- Botteon, A., Shimwell, T. W., Cassano, R., et al. 2022, *A&A*, 660, A78, doi: [10.1051/0004-6361/202143020](https://doi.org/10.1051/0004-6361/202143020)
- Bouhrik, F., Stanciolu, R., & Wittman, D. 2025, *ApJ*, 988, 166, doi: [10.3847/1538-4357/ade67c](https://doi.org/10.3847/1538-4357/ade67c)
- Bradač, M., Allen, S. W., Treu, T., et al. 2008, *ApJ*, 687, 959, doi: [10.1086/591246](https://doi.org/10.1086/591246)
- Burchett, J. N., Tripp, T. M., Wang, Q. D., et al. 2018, *MNRAS*, 475, 2067, doi: [10.1093/mnras/stx3170](https://doi.org/10.1093/mnras/stx3170)
- Cantwell, T. M., Scaife, A. M. M., Oozeer, N., Wen, Z. L., & Han, J. L. 2016, *MNRAS*, 458, 1803, doi: [10.1093/mnras/stw419](https://doi.org/10.1093/mnras/stw419)
- Carter, J. A., & Read, A. M. 2007, *A&A*, 464, 1155, doi: [10.1051/0004-6361:20065882](https://doi.org/10.1051/0004-6361:20065882)
- Cerny, C., Sharon, K., Andrade-Santos, F., et al. 2018, *ApJ*, 859, 159, doi: [10.3847/1538-4357/aabe7b](https://doi.org/10.3847/1538-4357/aabe7b)
- Cha, S., Cho, B. Y., Joo, H., et al. 2025, *ApJ*, 987, L15, doi: [10.3847/2041-8213/add2f0](https://doi.org/10.3847/2041-8213/add2f0)
- Chatterjee, S., Pillay, D., Datta, A., et al. 2025, *MNRAS*, 539, 981, doi: [10.1093/mnras/staf480](https://doi.org/10.1093/mnras/staf480)
- Cibirka, N., Acebron, A., Zitrin, A., et al. 2018, *ApJ*, 863, 145, doi: [10.3847/1538-4357/aad2d3](https://doi.org/10.3847/1538-4357/aad2d3)
- Clowe, D., Bradač, M., Gonzalez, A. H., et al. 2006, *ApJ*, 648, L109, doi: [10.1086/508162](https://doi.org/10.1086/508162)
- Dark Energy Survey Collaboration, Abbott, T., Abdalla, F. B., et al. 2016, *MNRAS*, 460, 1270, doi: [10.1093/mnras/stw641](https://doi.org/10.1093/mnras/stw641)
- Dawson, K. S., Schlegel, D. J., Ahn, C. P., et al. 2013, *AJ*, 145, 10, doi: [10.1088/0004-6256/145/1/10](https://doi.org/10.1088/0004-6256/145/1/10)
- Dawson, W. A., Wittman, D., Jee, M. J., et al. 2012, *ApJ*, 747, L42, doi: [10.1088/2041-8205/747/2/L42](https://doi.org/10.1088/2041-8205/747/2/L42)
- DESI Collaboration, Abdul-Karim, M., Adame, A. G., et al. 2025, arXiv e-prints, arXiv:2503.14745, doi: [10.48550/arXiv.2503.14745](https://doi.org/10.48550/arXiv.2503.14745)
- Dey, A., Schlegel, D. J., Lang, D., et al. 2019, *AJ*, 157, 168, doi: [10.3847/1538-3881/ab089d](https://doi.org/10.3847/1538-3881/ab089d)
- Duchesne, S. W., Johnston-Hollitt, M., Zhu, Z., Wayth, R. B., & Line, J. L. B. 2020, *PASA*, 37, e037, doi: [10.1017/pasa.2020.29](https://doi.org/10.1017/pasa.2020.29)
- Dutta, A., Peterson, J. R., Cianfaglione, M., & Sembroski, G. 2025, *PASP*, 137, 064102, doi: [10.1088/1538-3873/adcbd5](https://doi.org/10.1088/1538-3873/adcbd5)
- Faber, S. M., Phillips, A. C., Kibrick, R. I., et al. 2003, in *Society of Photo-Optical Instrumentation Engineers (SPIE) Conference Series*, Vol. 4841, *Instrument Design and Performance for Optical/Infrared Ground-based Telescopes*, ed. M. Iye & A. F. M. Moorwood, 1657–1669, doi: [10.1117/12.460346](https://doi.org/10.1117/12.460346)
- Finner, K., Jee, M. J., Cho, H., et al. 2025, *ApJS*, 277, 28, doi: [10.3847/1538-4365/adb0b6](https://doi.org/10.3847/1538-4365/adb0b6)
- Ge, C., Wang, Q. D., Tripp, T. M., et al. 2016, *MNRAS*, 459, 366, doi: [10.1093/mnras/stw599](https://doi.org/10.1093/mnras/stw599)
- George, L. T., Kale, R., & Wadadekar, Y. 2021, *MNRAS*, 507, 4487, doi: [10.1093/mnras/stab3309](https://doi.org/10.1093/mnras/stab3309)
- Ginsburg, A., Sipőcz, B. M., Brasseur, C. E., et al. 2019, *AJ*, 157, 98, doi: [10.3847/1538-3881/aafc33](https://doi.org/10.3847/1538-3881/aafc33)
- Golovich, N., Dawson, W. A., Wittman, D. M., et al. 2019a, *ApJ*, 882, 69, doi: [10.3847/1538-4357/ab2f90](https://doi.org/10.3847/1538-4357/ab2f90)
- . 2019b, *ApJS*, 240, 39, doi: [10.3847/1538-4365/aaf88b](https://doi.org/10.3847/1538-4365/aaf88b)
- Groeneveld, C., van Weeren, R. J., Botteon, A., et al. 2025, *A&A*, 693, A99, doi: [10.1051/0004-6361/202452687](https://doi.org/10.1051/0004-6361/202452687)
- Hao, J., McKay, T. A., Koester, B. P., et al. 2010, *ApJS*, 191, 254, doi: [10.1088/0067-0049/191/2/254](https://doi.org/10.1088/0067-0049/191/2/254)
- Harvey, D., Massey, R., Kitching, T., Taylor, A., & Tittley, E. 2015, *Science*, 347, 1462, doi: [10.1126/science.1261381](https://doi.org/10.1126/science.1261381)

- Hoeft, M., Dumba, C., Drabent, A., et al. 2021, *A&A*, 654, A68, doi: [10.1051/0004-6361/202039725](https://doi.org/10.1051/0004-6361/202039725)
- Hopp, C., Wittman, D., Stanciolli, R., et al. 2026, Spectroscopic Redshifts of 1,561 Galaxies in 12 Merging Galaxy Clusters from the X-SORTER Survey, Zenodo, doi: [10.5281/zenodo.18879235](https://doi.org/10.5281/zenodo.18879235)
- Ivezić, Ž., Kahn, S. M., Tyson, J. A., et al. 2019, *ApJ*, 873, 111, doi: [10.3847/1538-4357/ab042c](https://doi.org/10.3847/1538-4357/ab042c)
- Jee, M. J., Hughes, J. P., Menanteau, F., et al. 2014, *ApJ*, 785, 20, doi: [10.1088/0004-637X/785/1/20](https://doi.org/10.1088/0004-637X/785/1/20)
- Kaiser, N., Aussel, H., Burke, B. E., et al. 2002, in Society of Photo-Optical Instrumentation Engineers (SPIE) Conference Series, Vol. 4836, Survey and Other Telescope Technologies and Discoveries, ed. J. A. Tyson & S. Wolff, 154–164, doi: [10.1117/12.457365](https://doi.org/10.1117/12.457365)
- Kale, R., Venturi, T., Giacintucci, S., et al. 2015, *A&A*, 579, A92, doi: [10.1051/0004-6361/201525695](https://doi.org/10.1051/0004-6361/201525695)
- Kim, H., Ko, J., Smith, R., et al. 2022, *ApJ*, 928, 170, doi: [10.3847/1538-4357/ac510e](https://doi.org/10.3847/1538-4357/ac510e)
- Kim, S. Y., Peter, A. H. G., & Wittman, D. 2017, *MNRAS*, 469, 1414, doi: [10.1093/mnras/stx896](https://doi.org/10.1093/mnras/stx896)
- Kollmeier, J., Anderson, S. F., Blanc, G. A., et al. 2019, in Bulletin of the American Astronomical Society, Vol. 51, 274
- Liu, A., Yu, H., Diaferio, A., et al. 2018, *ApJ*, 863, 102, doi: [10.3847/1538-4357/aad090](https://doi.org/10.3847/1538-4357/aad090)
- Mann, A. W., & Ebeling, H. 2012, *MNRAS*, 420, 2120, doi: [10.1111/j.1365-2966.2011.20170.x](https://doi.org/10.1111/j.1365-2966.2011.20170.x)
- Markevitch, M., Gonzalez, A. H., Clowe, D., et al. 2004, *ApJ*, 606, 819, doi: [10.1086/383178](https://doi.org/10.1086/383178)
- McDonald, W., Obreschkow, D., & Garratt-Smithson, L. 2022, *MNRAS*, 516, 5289, doi: [10.1093/mnras/stac2276](https://doi.org/10.1093/mnras/stac2276)
- Ochsenbein, F., Allen, M. G., & Egret, D., eds. 2004, Astronomical Society of the Pacific Conference Series, Vol. 314, Astronomical Data Analysis Software and Systems (ADASS) XIII
- Paterno-Mahler, R., Randall, S. W., Bulbul, E., et al. 2014, *ApJ*, 791, 104, doi: [10.1088/0004-637X/791/2/104](https://doi.org/10.1088/0004-637X/791/2/104)
- Paul, S., Gupta, P., Salunkhe, S., et al. 2021, *MNRAS*, 506, 5389, doi: [10.1093/mnras/stab1965](https://doi.org/10.1093/mnras/stab1965)
- Pedregosa, F., Varoquaux, G., Gramfort, A., et al. 2011, *Journal of Machine Learning Research*, 12, 2825, doi: [10.48550/arXiv.1201.0490](https://doi.org/10.48550/arXiv.1201.0490)
- Pillay, D. S., Turner, D. J., Hilton, M., et al. 2021, *Galaxies*, 9, 97, doi: [10.3390/galaxies9040097](https://doi.org/10.3390/galaxies9040097)
- Prochaska, J., Hennawi, J., Westfall, K., et al. 2020, *The Journal of Open Source Software*, 5, 2308, doi: [10.21105/joss.02308](https://doi.org/10.21105/joss.02308)
- Randall, S. W., Markevitch, M., Clowe, D., Gonzalez, A. H., & Bradač, M. 2008, *ApJ*, 679, 1173, doi: [10.1086/587859](https://doi.org/10.1086/587859)
- Rines, K. J., Sohn, J., Geller, M. J., & Diaferio, A. 2022, *ApJ*, 930, 156, doi: [10.3847/1538-4357/ac67a8](https://doi.org/10.3847/1538-4357/ac67a8)
- Robertson, A., Harvey, D., Massey, R., et al. 2019, *MNRAS*, 488, 3646, doi: [10.1093/mnras/stz1815](https://doi.org/10.1093/mnras/stz1815)
- Robertson, A., Massey, R., & Eke, V. 2017, *MNRAS*, 465, 569, doi: [10.1093/mnras/stw2670](https://doi.org/10.1093/mnras/stw2670)
- Robitaille, T., Deil, C., & Ginsburg, A. 2020, reproject: Python-based astronomical image reprojection, *Astrophysics Source Code Library*, record ascl:2011.023. <http://ascl.net/2011.023>
- Rykoff, E. S., Rozo, E., Busha, M. T., et al. 2014, *ApJ*, 785, 104, doi: [10.1088/0004-637X/785/2/104](https://doi.org/10.1088/0004-637X/785/2/104)
- Rykoff, E. S., Rozo, E., Hollowood, D., et al. 2016, *ApJS*, 224, 1, doi: [10.3847/0067-0049/224/1/1](https://doi.org/10.3847/0067-0049/224/1/1)
- Sarkar, A., Randall, S., Su, Y., et al. 2023, *ApJ*, 944, 132, doi: [10.3847/1538-4357/acaef9](https://doi.org/10.3847/1538-4357/acaef9)
- Sehgal, N., Hughes, J. P., Wittman, D., et al. 2008, *ApJ*, 673, 163, doi: [10.1086/523840](https://doi.org/10.1086/523840)
- Snowden, S., & Kuntz, K. 2024, Cookbook for analysis procedures for XMM-Newton EPIC observations of extended objects and the diffuse background, Tech. report
- Soucail, G., Foëx, G., Pointecouteau, E., Arnaud, M., & Limousin, M. 2015, *A&A*, 581, A31, doi: [10.1051/0004-6361/201322689](https://doi.org/10.1051/0004-6361/201322689)
- Stanciolli, R., Wittman, D., Finner, K., & Bouhrik, F. 2024, *ApJ*, 966, 49, doi: [10.3847/1538-4357/ad3249](https://doi.org/10.3847/1538-4357/ad3249)
- Stanciolli, R., Wittman, D., Finner, K., Bouhrik, F., & Gao, Z. 2026
- Stephens, M. A. 1974, *Journal of the American statistical Association*, 69, 730
- Stuardi, C., Botteon, A., Sereno, M., et al. 2025, *A&A*, 695, L16, doi: [10.1051/0004-6361/202452581](https://doi.org/10.1051/0004-6361/202452581)
- Szabo, T., Pierpaoli, E., Dong, F., Pipino, A., & Gunn, J. 2011, *ApJ*, 736, 21, doi: [10.1088/0004-637X/736/1/21](https://doi.org/10.1088/0004-637X/736/1/21)
- Tempel, E., Tuvikene, T., Kipper, R., & Libeskind, N. I. 2017, *A&A*, 602, A100, doi: [10.1051/0004-6361/201730499](https://doi.org/10.1051/0004-6361/201730499)
- Tulin, S., & Yu, H.-B. 2018, *Phys. Rep.*, 730, 1, doi: [10.1016/j.physrep.2017.11.004](https://doi.org/10.1016/j.physrep.2017.11.004)
- Upsdell, E. W., Giles, P. A., Romer, A. K., et al. 2023, *MNRAS*, 522, 5267, doi: [10.1093/mnras/stad1220](https://doi.org/10.1093/mnras/stad1220)
- van der Walt, S., Schönberger, J. L., Nunez-Iglesias, J., et al. 2014, *PeerJ*, 2, e453, doi: [10.7717/peerj.453](https://doi.org/10.7717/peerj.453)
- van Weeren, R. J., Shimwell, T. W., Botteon, A., et al. 2021, *A&A*, 651, A115, doi: [10.1051/0004-6361/202039826](https://doi.org/10.1051/0004-6361/202039826)
- Virtanen, P., Gommers, R., Oliphant, T. E., et al. 2020, *Nature Medicine*, 17, 261, doi: [10.1038/s41592-019-0686-2](https://doi.org/10.1038/s41592-019-0686-2)
- Voges, W., Aschenbach, B., Boller, T., et al. 1999, *A&A*, 349, 389, doi: [10.48550/arXiv.astro-ph/9909315](https://doi.org/10.48550/arXiv.astro-ph/9909315)
- Wen, Z. L., Han, J. L., & Yuan, Z. S. 2024, *MNRAS*, 532, 1849, doi: [10.1093/mnras/stae1614](https://doi.org/10.1093/mnras/stae1614)
- Wilber, A., Brüggen, M., Bonafede, A., et al. 2019, *A&A*, 622, A25, doi: [10.1051/0004-6361/201833884](https://doi.org/10.1051/0004-6361/201833884)
- Wittman, D., Golovich, N., & Dawson, W. A. 2018, *ApJ*, 869, 104, doi: [10.3847/1538-4357/aace77](https://doi.org/10.3847/1538-4357/aace77)
- Wittman, D., Stanciolli, R., Bouhrik, F., van Weeren, R., & Botteon, A. 2025, arXiv e-prints, arXiv:2512.14945, doi: [10.48550/arXiv.2512.14945](https://doi.org/10.48550/arXiv.2512.14945)
- Wittman, D., Stanciolli, R., Finner, K., et al. 2023, *ApJ*, 954, 36, doi: [10.3847/1538-4357/acdb73](https://doi.org/10.3847/1538-4357/acdb73)
- York, D. G., Adelman, J., Anderson, Jr., J. E., et al. 2000, *AJ*, 120, 1579, doi: [10.1086/301513](https://doi.org/10.1086/301513)
- Yuan, Z. S., & Han, J. L. 2020, *MNRAS*, 497, 5485, doi: [10.1093/mnras/staa2363](https://doi.org/10.1093/mnras/staa2363)
- Yuan, Z. S., Han, J. L., & Wen, Z. L. 2022, *MNRAS*, 513, 3013, doi: [10.1093/mnras/stac1037](https://doi.org/10.1093/mnras/stac1037)
- Zhang, X., Simionescu, A., Gastaldello, F., et al. 2023, *A&A*, 672, A42, doi: [10.1051/0004-6361/202244761](https://doi.org/10.1051/0004-6361/202244761)
- Zitrin, A., Acebron, A., Coe, D., et al. 2020, *ApJ*, 903, 137, doi: [10.3847/1538-4357/abb8dd](https://doi.org/10.3847/1538-4357/abb8dd)

provides fast and easy peer review for new papers in the **astro-ph** section of the arXiv, making the reviewing process simpler for authors and referees alike. Learn more at <http://astro.theoj.org>.

This paper was built using the Open Journal of Astrophysics L^AT_EX template. The OJA is a journal which